MICRO STRUCTURAL ENVIRONMENTS AND REDOX STATES OF IRON IN RANDOM AND ORDERED POROUS SILCA MATRICES

by

Don Anton Shanthilal Amarasinghe

A dissertation submitted to the Graduate Faculty in Chemistry in partial fulfillment of the requirements for the degree of Doctor of Philosophy, The City University of New York

2009

This manuscript has been read and accepted for the Graduate faculty in Chemistry in satisfaction of the dissertation requirement for the Doctor of Philosophy.

Dr. Harry D Gafney

.....

Date

.....

Chair of Examining Committee.

Dr. Mahesh K Lakshman

.....

Date

.....

Executive Officer

Dr. Harry D Gafney

Dr. John R. Lombardi

Dr. Nan Loh Yang

Supervisory Committee

THE CITY UNIVERSITY OF NEW YORK

GRADUATE CENTER
CITY UNIVERSITY OF NEW YORK

ABSTRACT

MICRO STRUCTURAL ENVIRONMENTS AND REDOX STATES OF IRON IN RANDOM AND ORDERED POROUS SILCA MATRICES

by

D.A.S. Amarasinghe

Chairperson of the Supervisory Committee: Professor Harry D Gafney

Department of Chemistry and Biochemistry Queens College City University of New York.

In our previous studies we have shown that refractive index of porous Vycor glass can be changed by iron doping and at the lower end of the iron loading, the refractive index shows fairly linear increase with the loading. This allows us to create refractive index pattern in porous Vycor glass. The exact mechanisms regarding image formation in the Vycor glass and the factors that affect the image quality is still in discussion stage. In this study we analyzed the cross sectional distribution of iron and the lateral diffusion of iron during the heat treatment in order to understand the contrast variations. The study also focused on micro structural changes of iron from the surface to the interior of the porous Vycor glass. The other objective of the study is to understand micro structural variations of iron in regular pore structured materials such as MCM-41 and random pore networks such as xerogel and PVG.

Results show that the maximum effective lateral diffusion length of iron in PVG is <10 μm at 650^{0}C. Therefore we conclude

that particle growth occurs at 650^0C is due to <10 μm particle diffusion within the matrix. The XANES study results shows that elemental iron found in the PVG immediately after photolysis is concentrated in the interior of the glass. Although some elemental iron is found on the surface of the glass they are covered with a protective layer of Fe(III). This protective layer seems to be strong enough to prevent further oxidation of elemental iron particles during the annealing process at 650^0C but the elemental iron found in the interior of the glass oxidized during the annealing process until the protective layer of Fe(III) is formed. The results suggest that once the Fe(III) / Fe(0) ratio reach a critical value further oxidation is prevented. EXAFS data analysis along with EPR confirmed that the chemical nature of iron oxides formed on the surface and the interior of the PVG are identical and Fe(III) is in octahedral micro environment. The Mossbauer data suggest that the iron particles in the PVG substrate are randomly oriented where as Fe(III) has some orientation suggesting that particles are attached to silica substrate through the oxide envelope.

Unlike $Fe(CO)_5$ doped PVG, when $Fe(CO)_5$ doped MCM-41 is photolized, that leads to formation of octahedrally and tetrahedrally coordinated iron sites within the silica matrix. Mossbauer study shows that with the increasing temperature iron migration from octahedral sites to tetrahedral sites.

Irons in xerogel behave differently than iron in PVG or MCM-41.Iron migration into tetrahedral sites initiate at 650^0C and number of tetrahedral sites increase with the increase of temperature. Neither xerogel nor MCM-41 shows any evidence of elemental iron before or after heat treatments. The Fe(0) formation in PVG seems a unique phenomena.

ACKNOWLEDGEMENT

There are many people to whom my thanks are due for the vital roles they played in helping me on this work. First I would like to express my deep and sincere gratitude to my thesis advisor, Professor Harry D Gafney (PhD), Department of Chemistry, Graduate Center City University of New York, for his untiring reviews, constant feedback and unwavering guidance. His wide knowledge and logical way of thinking have been of great value for me. His understanding, encouragement and personal guidance have provided a good basis for the thesis.

I would like to thank my committee members Dr Lombardy and Dr Nan lo Yang for interesting discussions constructive criticism and excellent advices around my work.

I am especially grateful to Dr. D. Sunil and his family for many ways that they helped me during my years at CUNY. His guidance and suggestions made much of this work possible. Numerous discussions with Dr.Sunil lead to the design of X-ray absorption and Mossbauer experiments that provided the main motivation for this thesis.

I am also indebted to Dr. T.Cheung, Dr. Sarachik Myriam, Dr. Fred Cadieu Dr. Ed Look, Dr.Julie Colis.and Dr. Igor Kuskovsky at City University of New York for their support on my research work and also my thanks go to all my colleagues as well as to the faculty and staff of Chemistry department at Queens College. I would like to thank the X10C and X27A beam line staff at Brookhaven National Lab for their support and technical advices during data collection.

My especial thank goes to Samanthi and Thushara for their support and care that helped me overcome setbacks and stay focused on my study. I am also grateful to the Sri Lankan families who helped me to adjust to a new country.

None of this would have been possible without the love and patience of my family. I am enormously indebted to my wife Sandamali. Without her understanding and constant encouragement it would have not been possible for me to finish this work. I would like to express my heart-felt gratitude to my mother, sister brother in law and Supuna for their loving support.

TABLE OF CONTENT PAGE

List of figures PAGE

List of Tables PAGE

Chapter 1

1.0 INTRODUCTION

1.1. General Introduction

The state of aggregation of matter is a subject of wide diversity and complexity. The three states of matter gas, liquid and solid are the simplest categorizations of aggregation of matter. In the first approximation, the gas state is characterized by the absence of intermolecular interactions, which therefore display statistical disorder. The requirement of maximum entropy controls the state. The more condensed liquids and solids phases are controlled not only by entropy, but also by intermolecular interactions. The balance of interplay between attractive and repulsive forces yields a local order, defined on some characteristic length. Three state categorization is insufficient for a detailed study of matter. For example, gases can exist as gas or plasma (ionized gas), liquids as liquid or liquid crystals, solids can exist in crystalline or amorphous forms. An amorphous, or synonymously, a non-crystalline material can be defined as one which is topologically disordered and which does not exhibit either the long-range translational order (periodicity) characteristic of single crystals, or the long-range orientational order characteristic of quasicrystals. Within this definition, such materials could be either solid or liquid.

A material is a solid when there is no observable long-range translational diffusive motion during the duration of the experiment; in other words, dynamic disorder is absent. Glass is an amorphous solid. Glass includes all materials which are structurally similar to a liquid. However, under ambient temperature they react to the impact of force with elastic deformation and therefore have to be considered as solids. Classifying material as a glass requires prudence. Glasses can be obtained by freezing

super-cool liquids, thus creating a noncrystalline solid. However glasses can also be obtained by methods other than super-cooling. The prevailing description of a glass is an amorphous solid that exhibit a glass transition.

The **glass transition temperature**, T_g, is the temperature at which an amorphous solid, such as glass or a polymer, becomes brittle on cooling, or soft on heating. More specifically, it defines a pseudo, second –order, phase transition in which a super-cooled melt yields, on cooling, a glassy structure and properties similar to those of crystalline materials e.g. of an isotropic solid material. T_g is usually applicable to wholly or partially amorphous solids such as common glasses and plastics (organic polymers). Silica is the most common glass forming material. The study and manufacturing of new types of glasses and glasses doped with impurities are an essential part of the progress in optical systems. Porous silica matrices provide an ideal opportunity to develop impurity doping. In our previous studies we have shown the possibility of using iron oxide doped PVG and xerogel materials as wave guides.

Glass is an excellent and inexpensive material to integrate active and passive optical elements [36]. Unlike electrical conduction, optical conduction occurs in the bulk. Therefore it is important to study cross-sectional distribution of doped materials and their microstructure. A part of this study focuses on studying the micro structural variation of doped iron across the cross section of porous Vycor glass (PVG.) The other objective of the study is to understand microstructural variations of iron in regular pore structured materials such as MCM-41 and irregular pore structured materials such as PVG.

1.2. Silica Glass

Glassy materials have been known for centuries, though attempts to understand their nature are relatively recent [1].

This non-crystalline material can be made by rapidly cooling the melt of the constituent materials [2]. Unlike crystalline materials, which have a periodic structure that can be determined by diffraction techniques, there is no direct way of determining the arrangement of atoms in glasses [2]. The diffraction patterns of glasses consist of diffuse rings [2]. The Radial Distribution Function (RDF) of atoms in glasses can be deduced from the above diffuse rings [2]. Glasses have only short range atomic order compared to the long range order of crystalline materials. In silica glasses SiO_4 tetrahedra are still present with oxygen bridging two such tetrahedras, but neighboring tetrahedras are not in a fixed orientation with respect to each other [2].

Only certain materials form glasses. Glass formers, also called network formers [3], include SiO_2,B_2O_3,GeO_2,P_2O_5 and As_2O_3. Some other oxides e.g. Al_2O_3 are not network formers by themselves, but at the same time they do not weaken the bonding in the network and are called intermediates [2]. The strongly ionic oxides such as Na_2O, K_2O and CaO depolymerize the continuous random network of the former thereby weakening the bonding when incorporated in to the glass network. They are called glass modifiers [3]. It is not possible to predict whether an added impurity will behave as a network former (substitutional, tetrahedrally coordinated, covalently bonded) or as a modifier (interstitial, octahedrally coordinated, ionically bonded) or as an intermediate [2]. There is a basic scientific and technical need to establish the specifics of structural changes brought about by the incorporation of foreign materials in to glass.

1.3. Porous Vycor glass

Porous Vycor glass (Corning glass 7930) is prepared in three steps. A melt composed of SiO_2, B_2O_3 and Na_2O 17:4: 1 is quenched below, but near its consolute temperature. The consolute temperature is the maximum temperature of immiscibility for a two liquid solution. Below this temperature, liquids become only partially miscible.

Slow liquid-liquid diffusion makes a SiO_2 rich phase and a B_2O_3 rich phase. Then the boron rich phase is acid leached at about 100^0C, leaving an almost pure form of SiO_2 porous skeleton [4]. This material is said to have highly interconnected network of pores [4,5].

The most resent publication on the PVG structures shows that the average diameter of pores in PVG is about 4 nm and 96% of the total pore volume is due to pores with diameter 4±0.6 nm [6]. The porosity of PVG is about 28% with specific surface area of 250m^2/g. The glass is an electrical insulator but when pores of PVG were filed with a conductor it could become an electrical conductor [6].

1.4. Xerogel

The sol-gel process of preparing silica glass involves four basic steps; 1) hydrolysis, 2) condensation, 3) aging and 4) drying. Depending on the drying conditions these materials can be divided into two categories. The first called xerogel, is prepared by evaporation under ambient conditions; that gives rise to capillary pressure and causes shrinkage of the gel net work. If the wet gel is dried under supercritical conditions then there is no interface between liquid and vapor resulting in no capillary pressure. Gels prepared under these conditions are called aerogels. Compared to xerogels, aerogels have little shrinkage. The hydrolysis of silica alkoxide can be catalyzed by acids or bases. The mechanism for hydrolysis given below (**Figure 1**) is not complete, but is still useful to understand the effects of different factors on gelation [57].

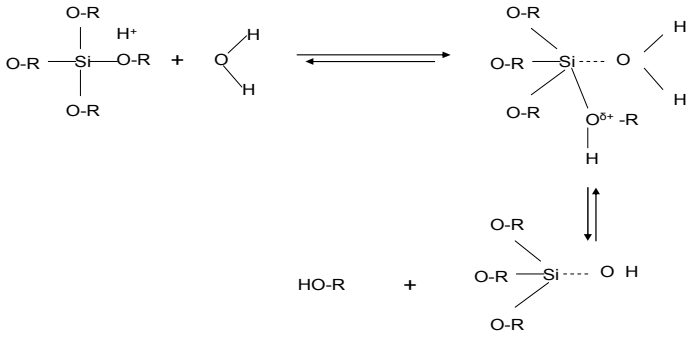

Acid catalyzed

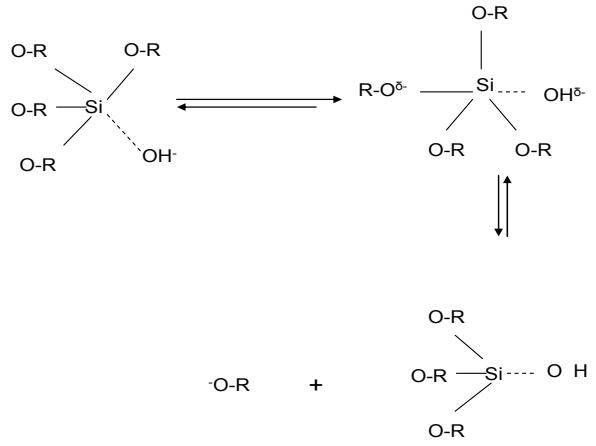

Base catalyzed

Figure 1. Mechanisms of hydrolysis of silica alkoxides.

The relative rates of condensation also depend on steric effect and the charge developed on the transition state. In acid hydrolysis, positively charged transition states are stabilized by electron donating groups. Therefore the condensation rates varies as follows for acid catalyzed reactions $(RO)_3SiOH > (RO)_2Si(OH)_2 > (RO)Si(OH)_3$ Because of the fast, first step, they form relatively open networks initially, followed by further hydrolysis and limited cross condensation (**Figure 2**).

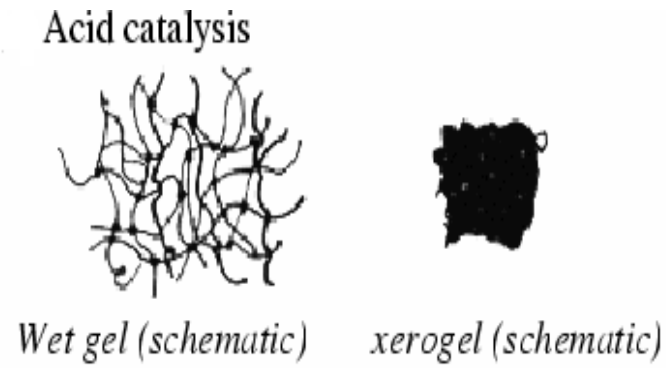

Figure 2. Acid catalyzed gel

In base catalyzed condensation, the negatively charged transition state become more stable as more hydroxyl groups replace the electron donating alkoxy groups. Thus, the state of the successive hydrolysis steps occurs rapidly with the fully hydrolyzed species undergoing the fastest condensation. As a consequence, in base catalyzed reactions, highly cross linked large sol particles are initially formed. Eventually they link to form gel with large gapes between particles (**Figure 3**).

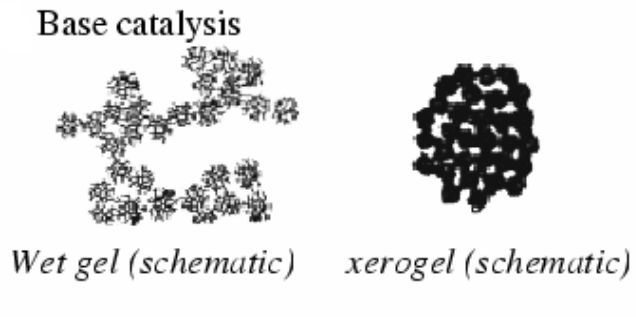

Figure 3. Based catalyzed gel

All of our experiments were carried out in the base-catalyzed environment.

1.5. MCM-41

When organic molecules other than solvent are added to the silica sol they became entrapped upon gelation. This can be used to introduce structure to gel. The lyotropic liquid crystalline phase formed by surfactants can also be used to add structure to a xerogel [57]. The self-assembly formations of cetyltrimethylammonium surfactants are used as templates for structuring silicates. Due to the electrostatic interactions between the cationic surfactant and negatively charged silica sol, the inorganic silica phase deposits around aggregates forming structures [57]. The detail mechanism of MCM-41 formation is not completely understood and is still a hot area of research.

One of the most exciting discoveries in the field of materials synthesis in resent years is the formation of mesoporous silicate and aluminosilicate molecular sieves [7]. According to IUPAC classification, porous materials with a pore diameter in the range of 2nm-50nm are defined as mesoporous materials [8]. Microporous materials have pore diameters of less than 2nm, and macroporous materials have pore diameter greater than 50nm. The mesoporous category thus lies in the middle [9]. In 1990, Kuroda and coworkers reported the preparation of mesoporous silica with uniform pore size distribution from layered poly-silicate kanemite[10,11]. Significant

breakthrough in mesoporous material research came with the discovery of the M-41S family of materials by Mobil scientists [8].

The family includes materials with pore structures such as; MCM-41 a two dimensional hexagonal [12], MCM-48 a Cubic and MCM-50 a lamellar [8] (**Figure 4**). MCM-41 is a nanoporous silica walled material that exhibits a regularly ordered 2D-hexagonal pore arrangement with narrow pore size distribution [8].

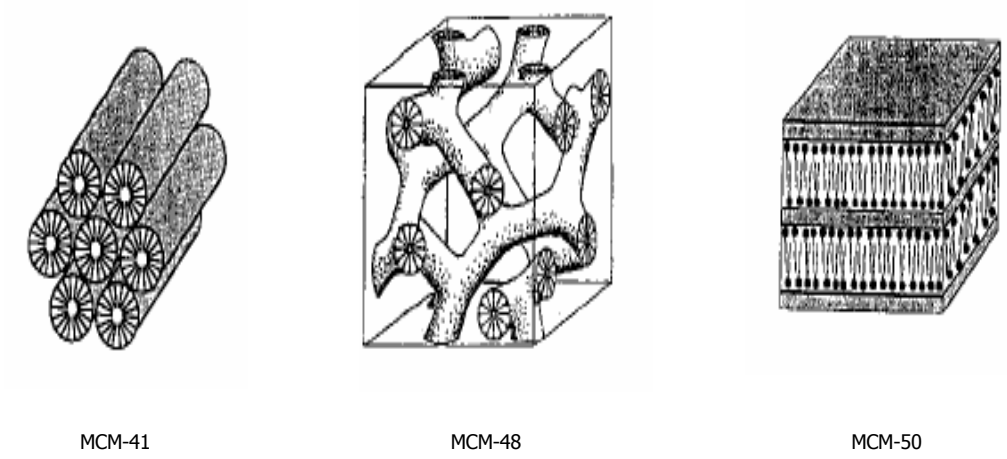

Figure 4. M-41S family

1.6.MCM-41 as a substrate

The high amount of silanol groups in MCM-41 enhances its ability to immobilize macromolecules such as metalloporphyrins [13].Several authors have reported use of MCM-41 as a drug delivery system. Zeng and co workers studied aspirin loaded MCM-41 as controlled drug released system [14]. Vallet-Regi and coworkers have reported the influence of pore sizes on the release rate of ibuprofen from the drug loaded MCM-41[15].

Enzymes such as globular enzymes, cytochrom c (bovine heart), papain (papaya latex) and trypsin (bovine pancreas) have been immobilized in a MCM-41 molecular sieve [16]. Kulkarni and co-workers studied the immobilization of iron-porphyrin complexes inside the pores of MCM-41 using various synthetic procedures [17].

MCM-41 loaded with copper and iron oxides act as catalysts for methanol decomposition to H_2 and CO have been studied by Tsoncheva and coworkers [18]. Catalytic cracking of large molecules have been reported on Al-MCM-41 [19].

1.7. Iron Oxides

Fifteen iron oxides and oxide hydroxides are known to date [20]. The most common ones are listed in **Table 1**. The most common structural unit of Fe(III) oxide is an octaheadron in which Fe atoms are coordinated to six oxygen atoms, or OH^- ions or both [20]. The Fe(III) in the octahedral positions can be partially replaced by other trivalent cations with similar size like Al^{3+}, Mn^{3+},Cr^{3+}.and V^{3+} without modifying the structure [20]. In hematite and goethite, the layers formed by O^{2-} and OH^- ions are hexagonally closed packed (hcp) and called the α-phases. In lepidocrocite and maghemite they are approximately cubic closed packed (ccp) and called the γ-phase. The oxide Fe_2O_3, exhibits amorphous or crystalline phases such as γ-Fe_2O_3 (maghemite), α-Fe_2O_3 (hematite). There are few meta-stable phases of iron oxides such as β (beta) and ε (epsilon). The beta phase has a cubic face centered structure, but at temperatures above 500°C, the beta phase converts to alpha phase. The epsilon phase has a rhombic structure. This phase shows properties intermediate between alpha and gamma. So far, this phase has not been prepared in pure form.

Table 1. Common iron oxides and oxide hydroxieds

Oxyhydroxides		Oxides	
Formula	**Mineral**	**Formula**	**Mineral**
α-FeOOH	*Goethite*	*Fe5HO8. 4H2O*	*Ferrihydrite*
β-FeOOH	*Akaganeite*	*α -Fe_2O_3*	*Hematite*
γ-FeOOH	*Lepidocrocite*	*γ -Fe_2O_3*	*Maghemite*
δ-FeOOH	*Feroxyhyte*	*Fe_3O_4*	*Magnetite*

Iron and iron oxides are some of the most attractive materials as they exhibit interesting optical and magnetic properties [21]. Iron based nanoparticles have become the focus of intense research because of their use in magnetic information storage devices, magnetic refrigerants, oxidation reduction catalyst, biological and environment sensors and bio medical applications [22].

The stability and semiconductor properties of α-Fe_2O_3 allow it to be used as a photocatalyst, while the magnetic properties of γ-Fe_2O_3 make it a common active component of high-density recording media [23]. The two forms of Fe_2O_3 differ in many aspects. Structurally the unit cell of γ-Fe_2O_3 is cubic, with both octahedrally and tetrahedrally coordinated Fe(III) sites, while α-Fe_2O_3 has hexagonal unit cell and entirely octaheadraly coordinated Fe(III) sites [24].The increasing exploration of nanotechnology in biological and medical applications has led to significant advances in the diagnosis, prevention, and treatment of diseases. Superparamagnetic iron oxide nanoparticles (SPIO) currently have a surge of interest as their potential has been demonstrated in biomedical applications such as MRI contrast agent [25], [26],[27] ,[28], drug carries and in therapy [29].

Bulk hematite is antiferromagnetic below the Morin temperature, 260K and weakly ferromagnetic above Morin temperature [30].

The net moment of antiferrormagnetic particles is very sensitive to particle size, lattice strain and defects [31]. Because of the potential for exhibiting magnetization reversal by quantum tunneling, the magnetic properties of antiferromagnetic nanoparticles have been receiving renewed attention in the last few years [31]. The net magnetic moment of antiferromagnetic particles, resulting from the non-exact compensation of the two magnetic sublattices, is very sensitive to particle size, lattice strain and defects [31].

1.8. Iron impregnated PVG in integrated Optics

Even though inorganic-organic nano-composites have been studied with growing interest over last few years, [32] less attention has been paid towards the research and development of inorganic- inorganic nanocomposites.

The field of integrated optics covers an exploration of waveguide techniques for the construction of newly improved optical devices [33]. In recent years there has been remarkable progress in the development of integrated optical devices [33]. This increasing interest in optical integrated circuits stimulated the studies on optical waveguide materials. Polymers are the most commonly used wave guiding materials [34] as they can be easily used to make thin films. There are some disadvantages of using polymers as wave guiding materials. Optical losses are higher in polymer based devices compared to silica based devices. In addition, they have poor surface quality and higher thermal expansion coefficients [34]. However, little attention has been paid to the development of glass based integrated optical devices [33].

Porous Vycor glass (PVG), Corning code 7930, is nearly a pure form of silica with a small amount of boric oxide. PVG is a good solid support for this kind of application because of its high strength, chemical inertness, thermal stability and porosity. A distinct advantage of this support over others is physical strength and transparency to visible light. SEM and AFM analysis of the calcinated PVG glasses reveal that the surface is composed of silica

nodules with intervening crevices [35]. These intervening crevices compose the interconnecting pore structure that is randomly distributed throughout the matrix. The external and interior surfaces of the glass have free and associated hydrogen bonded, Si-OH, silanol, groups and absorbed water [35]. Porous glasses impregnated with electro or magneto-optical materials for example, can be used to make many optical components [36,37,38].

Iron is common in naturally occurring silicate glasses and is known to significantly affect macroscopic properties such as color, polymerization, viscosity, density and heat capacities of silica glasses [39]. Borrelli and Morse showed that the refractive index of glass could be changed by photo-chemically binding transition metal compounds into Corning code 7930 porous Vycor glass and thermally consolidating the glass to nonporous, nonscattering optical medium [40]. According to our previous studies reported elsewhere, deposition of $Fe(CO)_5$ and photolysis produce refractive index changes upto 10^{-3} to 10^{-2} depending on the loading [35]. At the lower end of the iron loading, the refractive index shows fairly linear increase with loading [35]. Iron deposition and their subsequent changes are important because of the ability to pattern them with relative ease to make different forms of waveguides and opto-electronics [41]. We have reported that these composites can be consolidated without significant loss of resolution. There is very little information currently available that can be used to optimize efficiency of this photo deposited optical devises. Systematic scientific study of these systems is required to harness the full potential of making low cost photonic devices.

In this study, we focus on analyzing the distribution and the structure of photo products and their changes with temperature at the surface and the core of the glass. There are number of publications available on investigation of structural and chemical information of the iron in glasses.

As per our understanding, there was no study that investigated the structural and chemical environment of iron on the surface of glass and within the interior of the glass.

1.9. Iron doped MCM-41

Materials of nanometer scale are important in developing advanced quantum confined electronics and optoelectronics. Colloidal solutions [42] and polymer matrixes [43] are widely used for nonmaterial synthesis. But these hosts are neither efficient in generating uniform size clusters nor chemically inert towards guest materials [44]. On the other hand the regular pore structure of zeolite molecular sieves offers an ideal reaction chambers for nanostructure material synthesis [44]. However, the smaller pore size of these materials limits their applicability. The discovery of mesoporous molecular sieve such as the M41S family broadened the applications [44].

In 1992 Kresge and co workers first reported [45] the synthesis of M41S family of silicate mesoporous materials, MCM-41 is the most widely studied member of M41S family [46]. MCM-41 has highly attractive features such as stable honeycomb pore structure relatively large pore area, usually. 1000m^2/g (for details about surface area determination see reference [47]-[46]) and relative chemical inertness.

1.10. Iron doped MCM-41 in catalysis

Even though pure silica MCM-41 shows limited catalytic activity, active catalytic sites can be generated by introducing metals [48]. These particles often exhibit unusual catalytic properties [49], and Iron oxide nanomaterials in silica matrices are currently of great interest for exactly the same reasons [50]. Characterizing of iron oxides in glass matrices is difficult, partly because of the large range of oxides and oxide hydroxides iron can form with varying oxidation states. Fifteen iron oxides, oxide hydroxides are known to date [51]. The most common structural unit of Fe(III) oxide is an octahedron in which Fe atoms are coordinated to six, oxygen atoms or OH ions or both [20].

T. Kawabata and coworkers [52] have reported the Fe-MCM-41 ability to catalyzed Bayer- Villiger (B-V) reactions. The B-V oxidation of ketones is widely used for the synthesis of lactones [52]. Using heterogeneous catalysis for B-V reactions has some advantages such as simplicity in synthetic operations, prevention of the production of salt wastes during neutralization of catalysts, reusability of catalysts [52,53,54]. As iron containing materials show low toxicity [55] make it more attractive as a catalyst. Fe-MCM-41 is known for it use as a catalytic template for the production of carbon nanotubes [56].

Chapter 2

2. 0. EXPERIMENTAL

2.1. Materials

Corning code 7930 porous Vycor glass was obtained from Corning Glass in the form of plates with thickness of 2mm. Tetramethylorthosilicate (TMOS, $(CH_3O)_4Si$;95%), Tetraeathoxysilane (TEOS, $(CH_3CH_2O)_4Si$;95%), iron(III) oxide (Fe_2O_3;99.98%) were purchased from Sigma Aldrich and used without further purification. Reagent grade 15M ammonium hydroxide (NH_4OH;99.9%), α-Fe thin film was obtained from Fisher Scientific. Spectroscopic grade Methanol (CH_3OH), Iron pentacarbonyl ($Fe(CO)_5$), hexadecyl trimethyl-ammonium bromide ($CH_3(CH_2)_{15}N(CH_3)_3$,CTAB ;99+%), was purchased from Alfa Aesar.

2. 2. Pre-treatments

PVG was first dipped 3M HCl for 1Hr, and then rinse with hot and running distilled water for over 48 hours to remove water soluble contaminants. The partially cleaned PVG was then rinsed with spectroscopic grade methanol. The PVG pieces were dried in a National appliance company vacuum oven model 5831 about 70^0C for over one week at 50torr. PVG was then allowed to cool to room temperature in a vacuum desecrator.

2.3. Synthesis

2.3.1 MCM-41 Synthesis

For the synthesis of MCM-41 TEOS 98% was used as a silica source, CTAB, 99+% as a super-molecular templating agent, and NaOH as the catalysis were used. These reagents were used in following ratio: TEOS-1.02ml CTAB (92g/100ml) 10ml , NaOH (2M) 1.32ml . CTAB and TEOS were mixed together to form a uniform solution and then under vigorous stirring NaOH was slowly added to the solution. The pH was then adjusted to 11.5

with H_2SO_4. The solution was stirred, open to atmosphere, at room temperature for 48 hours. The solid product was recovered by filtration, washed with ethanol and deionized water, and dried in a vacuum oven at 100^0C. The product was then heat treated in air using a 1^0C/min heating ramp and dwell time of 6hours at 540^0C to remove organics.

2.3. Xerogel Synthesis

Xerogel were prepared as per the procedure described in reference 40 using TMOS, methanol and water. The TMOS and water didn't mix well at room temperature, [57] however adding MeOH increases miscibility. Methanol, TMOS and water were vigorously stirred until a uniform solution was formed. Then concentrated ammonia was added drop wise to the stirring solution. The gel time is longest at the iso-electric point therefore added based (or acid) reduced gel time [57].The catalyzed reaction mixture was stirred for another 5-7min and covered with polyethylene film and allowed to dry for 3-5weeks. The pre dried gel is then further vacuum dried at 60^0C for 12-15 hours in a National Appliance Company vacuum oven model 5831 at 50 torr.

2.3.3 Vapor deposition

The uniform adsorption of $Fe(CO)_5$ onto PVG glass was achieved by using the set up shown in **Figure 5**. The setup used to impregnate the MCM-41 and the xerogel is shown in **Figure 6**.The samples were heat treated in air according to the program shown in **Figure 13**, using a programmable Thermoline 461000 oven.

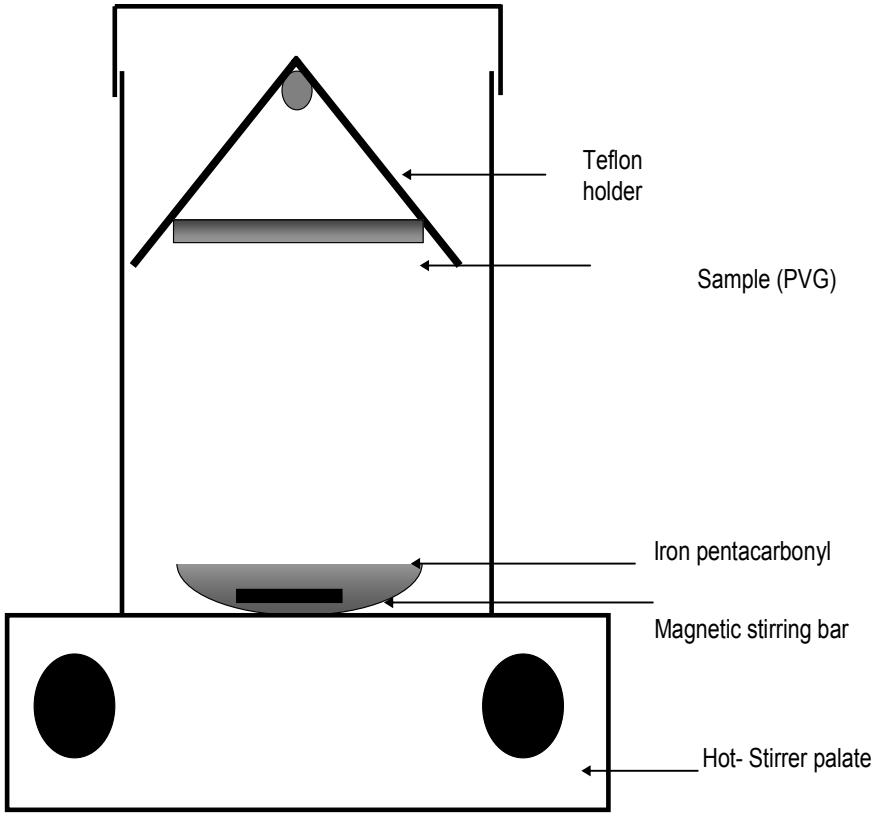

Figure 5. The setup used for vapor deposition of Fe(CO)5 on PVG .

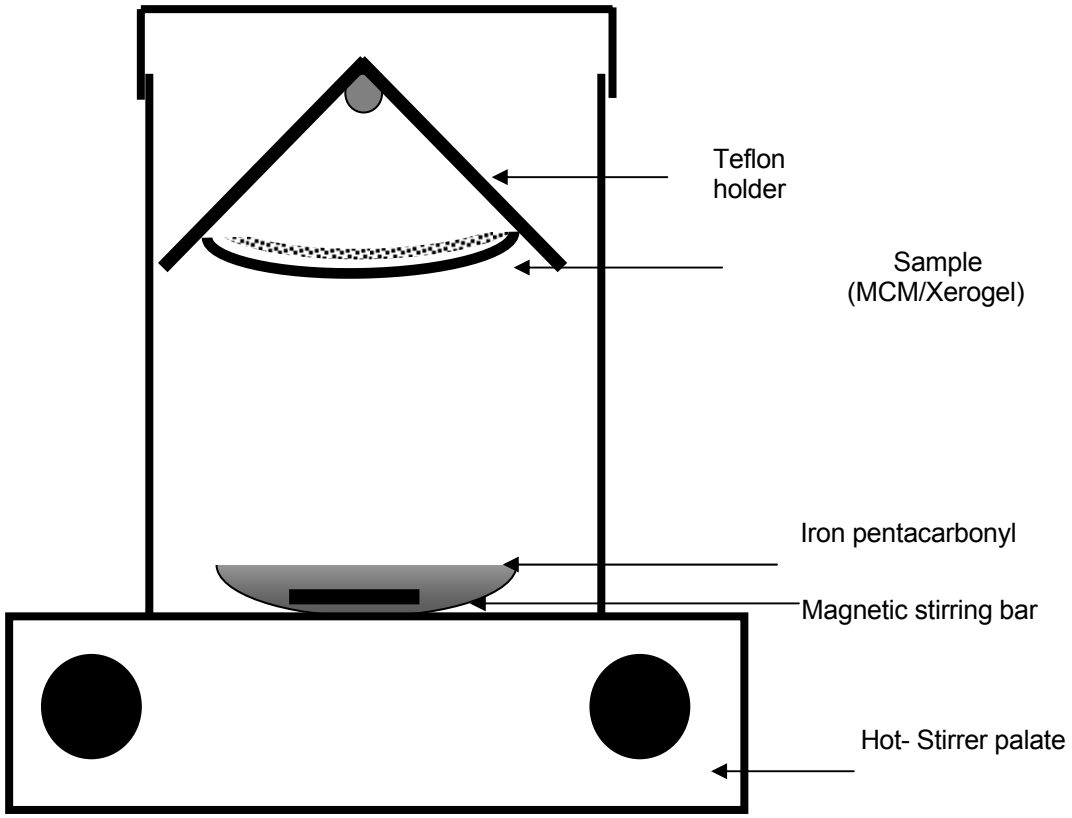

Figure 6. The setup used for vapor deposition of $Fe(CO)_5$ on Xerogel and MCM-41 .

2.4. Instrumentation

2.4.1 X-Ray Diffractometry

XRD spectra were recorded on Philips, PW1050/25 goniometer using Cu-K_α radiation(λ=1.54A). X-ray diffraction (XRD) is a versatile, non-destructive technique that reveals detailed information about the crystallographic structure of materials. A crystal lattice is a regular distribution of atom or atom clusters in space. These are arranged so that they form a series of parallel planes separated from one another by a distance *d*, which varies according to the nature of the material. For any crystal, planes exist in a number of different orientations - each with its own specific *d*-spacing. By varying θ (**Figure 7**), Bragg's Law conditions are satisfied by different *d*-spacings in crystalline materials. Plotting the angular positions and intensities of the resultant diffracted peaks of radiation produces a pattern, which is characteristic of the arrangement of atoms within the sample. When mixtures of different phases are present, the resultant diffractogram is formed by addition of the individual patterns. Based on the principle of X-ray diffraction, the structure of the material investigated can be obtained.

(a)

$$2d \sin \theta = n\lambda$$

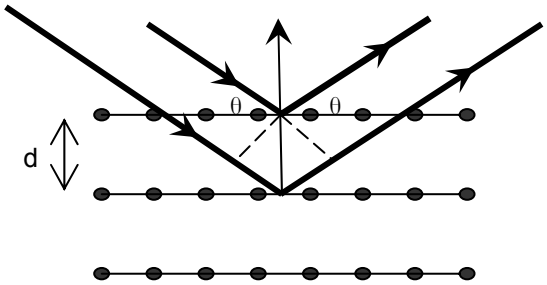

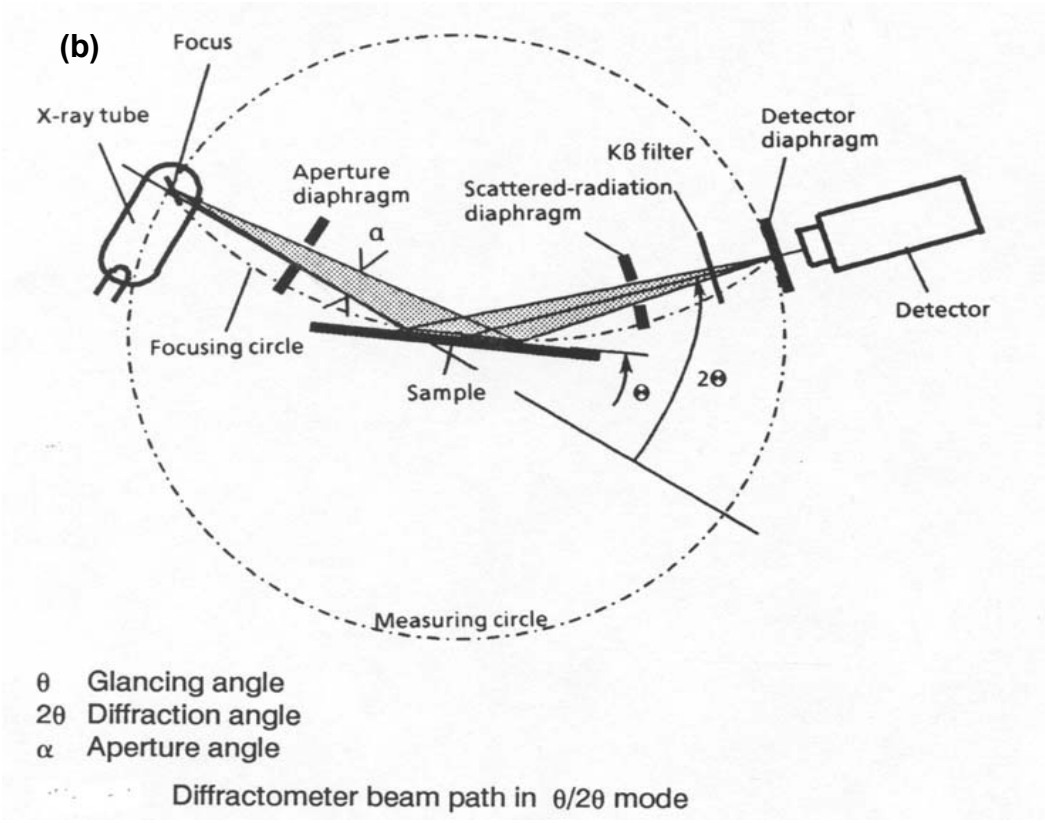

Figure 7. a)Bragg's law b)The schematic diagram of the X-ray diffractometer.

2.4.2 UV-Visible Spectra

UV-Visible absorption spectra were recorded on Cary 5000 spectrometer in double beam mode with full slit height. All spectra were recorded in 1nm data intervals. The spectrometer has source changeover at 350nm and detector change over at 800nm.

2.4.3 Mossbauer Spectra

i) Mossbauer Effect

The nuclear energy levels are influenced by their surrounding environment both electrically and magnetically. These either lift the degeneracy of energy levels or shift their energy thereby providing information about the atoms local environment. However there are two main obstacles: first hyperfine interaction between the nucleus and its environment are extremely small, and second recoil of the nucleus as the *γ*-ray is emitted or absorbed prevents resonance (**Figure 8**).

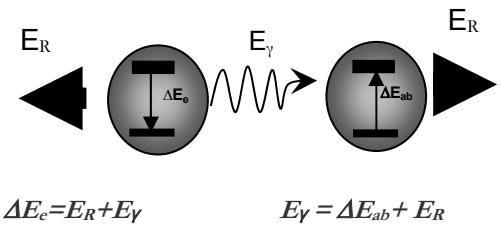

Figure 8. Recoil of nuclei

As the atoms will be moving due to random thermal motion, the gamma-ray energy has a spread of values E_D caused by the Doppler effect. This produces a gamma-ray energy profile as shown in **Figure 9**. To produce a resonant signal the two energies need to overlap and this is shown in the black-shaded area. This area is extremely small, so that 10^{-6} or less of the gamma-rays are in this region. As a result, gamma-ray absorption is impractical as a spectroscopic technique.

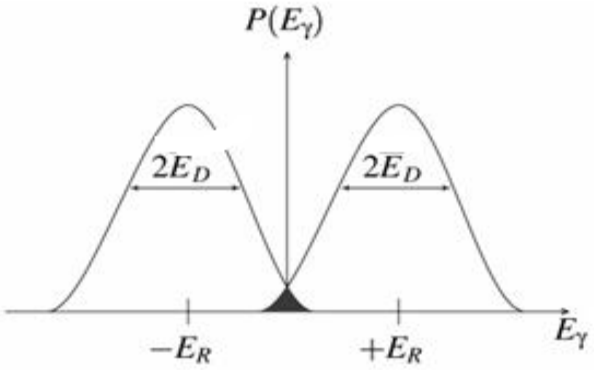

Figure 9. gamma-ray energy profile

Mössbauer discovered that when the atoms are within a solid matrix the effective mass of the nucleus is very much greater. The recoiling mass is now effectively the mass of the whole system, making E_R and E_D very small. If the gamma-ray energy is small enough, the recoil of the nucleus is too low to be transmitted as a phonon (vibration in the crystal lattice) and making the recoil energy practically zero; a recoil-free event. In this situation, if the emitting and absorbing nuclei are in a solid matrix the emitted and absorbed gamma-ray is the same energy (resonance). The resonance only occurs when the transition energy of the emitting and absorbing nucleus match exactly.

The Mössbauer effect is only detected in isotopes with very low lying excited states because of the relatively high number of recoil-free events. Hence the strength of the signal is strongly dependent upon the gamma-ray energy. Similarly the resolution is dependent upon the lifetime of the excited state. These two factors limit the number of isotopes that can be used successfully for Mössbauer spectroscopy. Following elements; Fe , Ru, Sn, Sb, Te, I, W, Ir, Au, Eu, Gd, Dy, Er, Yb and Np fulfilled the above requirements and form Mossbauer active isotopes.

ii) Experimental setup

Figure 11 is a schematic of the experimental arrangement for Mossbauer spectroscopy. In our experiments, a 10mCi, Co-57 in Rh matrix was used as a source. The ^{57}Co nucleus decays by K electron capture to an excited state of ^{57}Fe according to the scheme shown below with approximately 270 days half life.

$$^{57}Co + \beta \rightarrow {}^{57}Fe .$$

The source was mounted on a K-4 linear motor which moves back and forth with a velocity, that is a periodic saw tooth function of time. The dwell time per channel was set to 400 μsec. A sample containing ^{57}Fe atoms in an environment that permits recoilless absorption of 14.4 keV photons was placed between the source and the proportional counter. Calibrations were performed with 25-μm thick α-Fe standard.

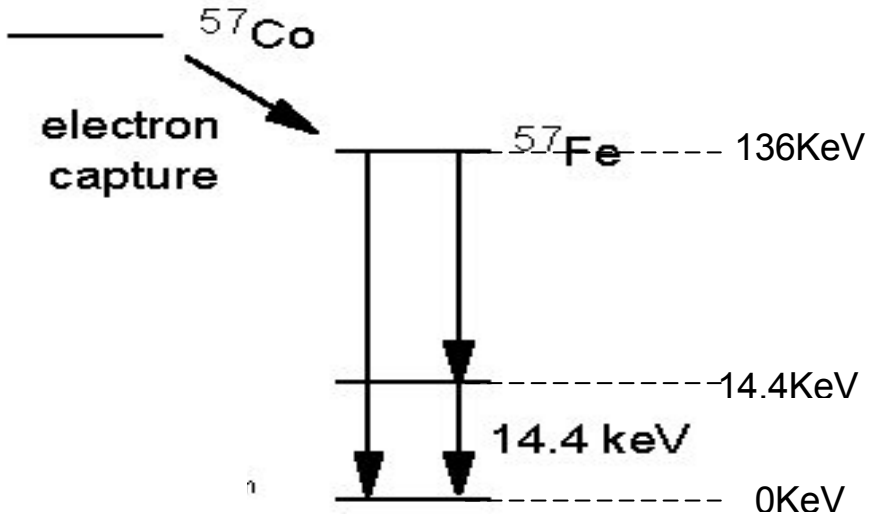

Figure 10. Decay scheme of ^{57}Co

.

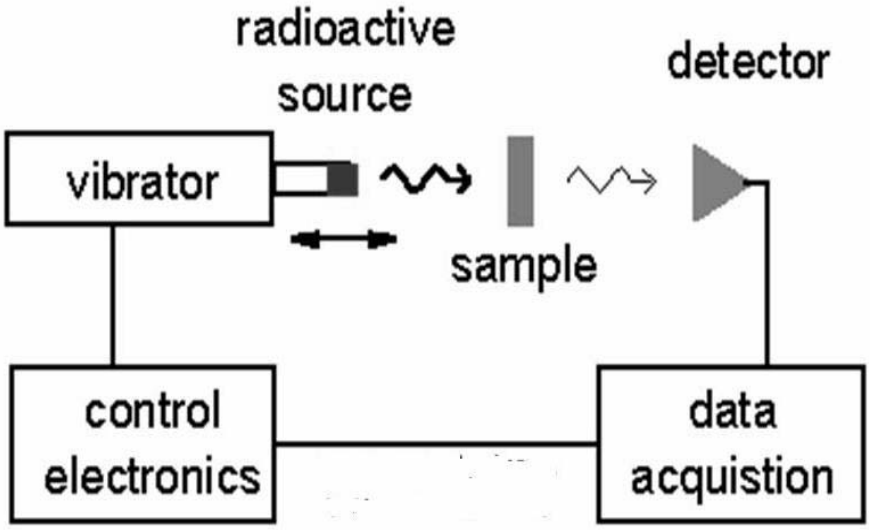

Figure 11. Schematic Mossbauer experimental setup.

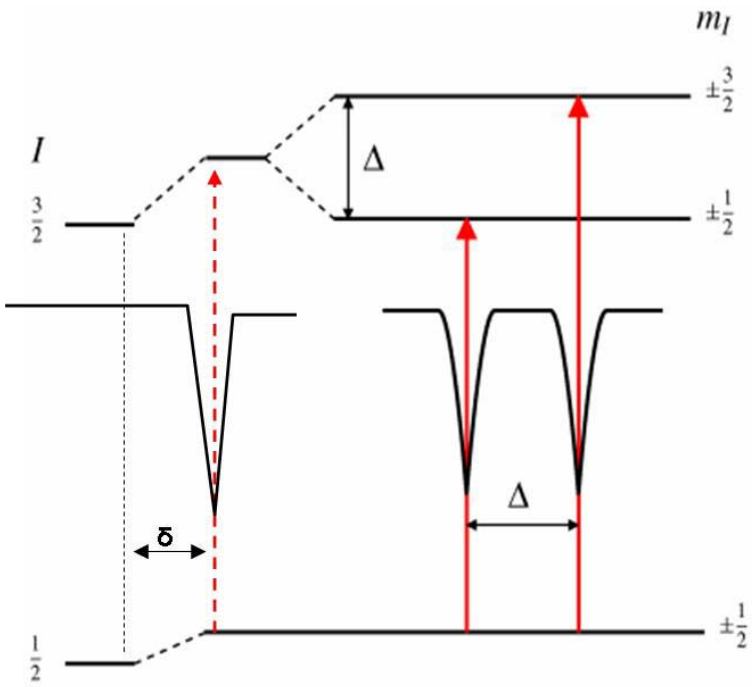

Figure 12. Mossbauer absorption transitions of ^{57}Fe.

i) Isomer Shift (δ)

Difference in the s-electron environment between the source and absorber produces a shift in the resonance energy of the transition (**Figure 12**). The whole energy spectrum shifts positively or negatively depending upon the s-electron density. The isomer shift provides information about valency states, ligand bonding states, electron shielding and the electron-drawing power of ligands.

ii) **Quadrupole Splitting (Δ)**

Non spherical charge distribution (nuclear angular momentum quantum number I>1/2) produces a nuclear quadrupole moment. Asymmetric electric fields split the nuclear energy levels (**Figure 12**).

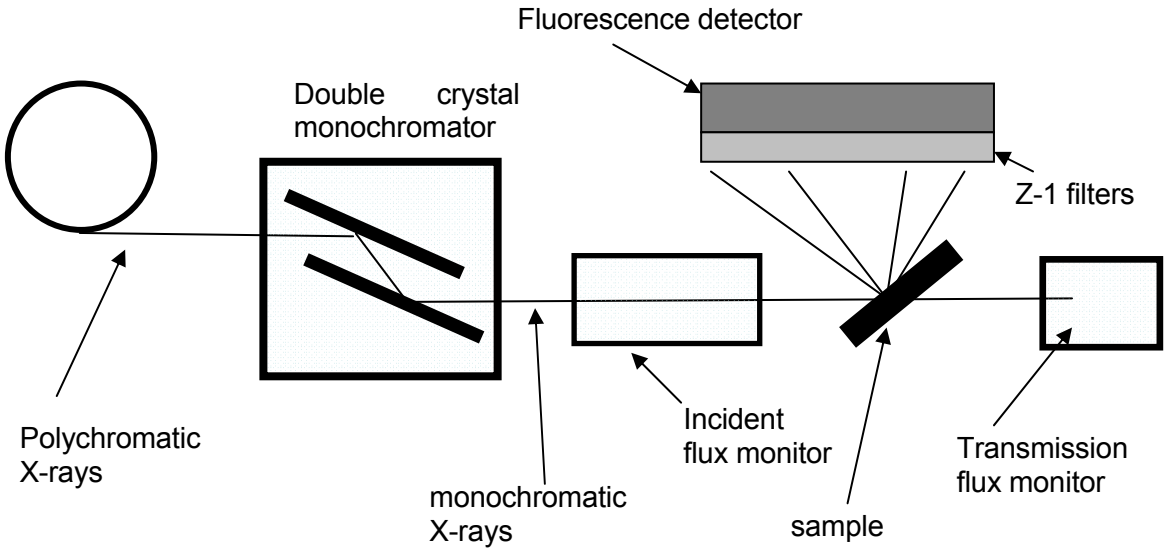

Figure 13. Schematic XAFS experiment setup

2.4.4 X-Ray Absorption Fine-Structure

X-ray Absorption Fine Structure (XAFS)) is the modulation of X-ray absorption coefficient at energies near and above an X-ray absorption edge. XAFS is also referred to as X-ray Absorption spectroscopy (XAS) and is divided into two regimes.

1. X-ray Absorption Near-Edge Spectroscopy (XANES)
2. Extended X-ray Absorption Fine-Structure (EXAFS)

For this study both XANES and EXAFS spectral regions were collected and analyzed.

The basic principle of XAFS experimental setup is as follows (**Figure 13**). The synchrotron produces polychromatic x-rays. A desired energy band with narrow band width (<1eV) is then selected by diffraction from silicon double crystal monochromator. Only those x-ray photons that satisfy conditions given in **equation 4** will be reflected from the first crystal at the selected angle θ; the others are absorbed. Equation 4 is derived in the following manner,

$$E = h\nu \quad \textbf{(1)}$$

Where *E* is the Photon energy *h* is the plank constant and *v* is the frequency.

$$C = \upsilon\lambda \quad \textbf{(2)}$$

Where c is the speed of light, ν is the x-ray frequency and λ is the wave length.

$$n\lambda = 2d\sin\theta \quad \textbf{(3)}$$

is the Bragg condition.

Substitution yields,

$$E = \frac{nhC}{2d \sin\theta} \qquad \textbf{(4)}$$

The parallel second crystal was used to restore the beam to its original position.

X-ray absorption spectra were run on the Exxon's X10C beam line at Brookhaven National Laboratory, New York. The beam line consist of double crystal monochromator, bent cylindrical focusing mirror, photon shutter and an experimental hutch. Data acquisition and beam-line controls were done on a VAM based MicroVAX computer system. The first crystal was water cooled through a copper thermal strap which was attached to a compliant force crystal holder. The heat is extracted from the crystal sides to minimized thermal gradients at the crystal surface. The primary crystal motions for energy scans are independent and orthogonal translations. The first crystal position determines the beam height while second is positioned to intercept the X-ray beam from the first.

Spectra were acquired in the energy-scanning mode, using a Stern- Heard-Lytle type fluorescence detector filled with argon. The beam intensity was monitored, upstream of the sample chamber (**Figure 13**). The signal was then normalized to incident beam intensity. Sample pellets were mounted on Kapton tape and exposed directly to the incoming beam at a 45^0 angle. X-ray absorption spectra were collected starting from 200eV below Fe K-edge to 4eV below Fe K-edge with 5eV steps, in the pre edge region, from 7108 to 7120 eV in 0.2eV steps, in the 7120.2eV to 7140eV region in 0.5eV steps and in the 7140eV to 7999eV region in 5eV steps. For every sample, three runs were obtained under the above settings. Energies were calibrated

with iron foil (Fe(0)) absorption edge at 7112.0eV at periodic time intervals. Count time was set as 12 seconds per point.

PVG Samples

A Pretreated 2cm x 2cm PVG piece was impregnated with $Fe(CO)_5$ and then cut into two equal pieces. The EXAFS spectra of the two halves were recorded in the fluorescence mode. The top 30μm layer of the half without heat treatment was removed using a diamond file. The removed top surface was denoted as PVG-01. The sample with the removed surface was denoted as PVG-02. The other half of the sample was heat treated according to program-01. The removed top surface of the heat treated samples was denoted as PVG-03 and the sample whose surface was removed was denoted as PVG-04.

MCM-41 Samples

Iron doped MCM-41 was mounted on to the sample holder with Kapton tape. The spectra were recorded in the fluorescence mode. Approximately the same amount of MCM-41 was used and the material was distributed uniformly on the Kapton tape.

Xerogel Samples

Iron impregnated samples were ground to a powder and mounted on to the sample holder with Kapton tape. Approximately the same amount of Xerogel was used with uniform distribution on the tape. The spectra were recorded in the fluorescence mode.

2.4.5 Programmable Oven

PVG Samples

The sample was broken in to two equal pieces and one was heat treated in the Thermoline programmable oven with 20 ^{0}C/min ramp up to 650^{0}C, 4Hours dwell time at 650^{0}C and then the samples were cool back to room temperature at a slow rate in the furnace (**Figure 14**).

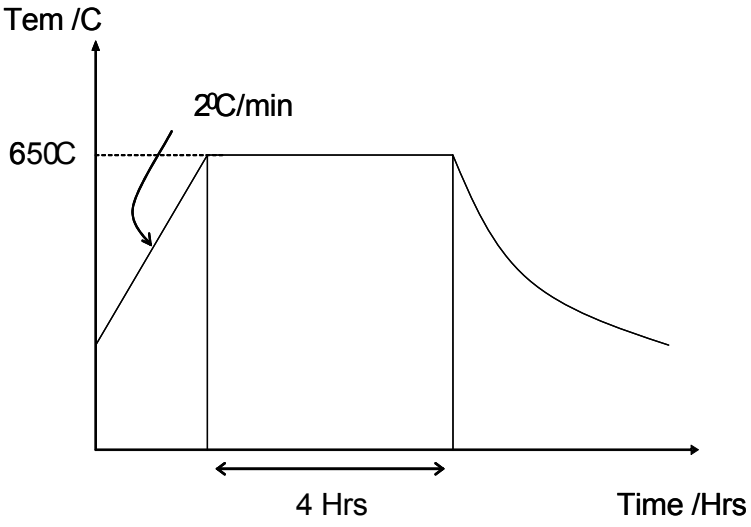

Figure 14. Heating program

MCM-41 Samples

The sample was used as it is. The Thermoline programmable oven was used with the same program described above (**Figure 14**).

Xerogel Samples

The sample was used as it is. The Thermoline programmable oven was used with the same program described above (**Figure 14**).

2.4.6 Electron paramagnetic resonance (EPR)

Electron paramagnetic resonance (EPR) or Electron Spin Resonance (ESR) spectroscopy is a technique for studying chemical species that have one or more unpaired electrons, such as organic and inorganic free radicals or inorganic complexes possessing a transition metal ion. The basic physical concepts of EPR are analogous to those of nuclear magnetic resonance (NMR). But in EPR, it is electron spins that are excited instead of spins of atomic nuclei.

An external magnetic field removes the degeneracy of the energy levels (**Figure 15**), since it interacts differently with electrons that have different

quantum numbers. The splitting of spectral lines in the presence of a static magnetic field is called the Zeeman Effect. It is analogous to Stark effect where the splitting is due to an electric field. The different projections of the spin gains different energies.

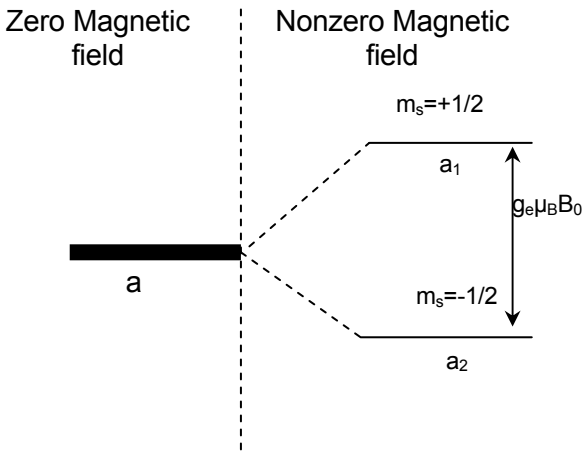

Figure 15: Zeeman effect

The electron has a spin quantum number s=1/2 with magnetic components m_s = ±1/2. In an external static magnetic field the energy splitting ΔE is given by,

$$\Delta E = g_e \mu_B B_0 \tag{5}$$

Where B_0 is the external field strength, μ_B is the Bohr magneton and g_e is the electron's g-factor (or Landé g-factor).

$$\mu_B = \left| \frac{eh}{4\pi m_e} \right| = 9.2740 \ X10^{-24} \ J/T \tag{6}$$

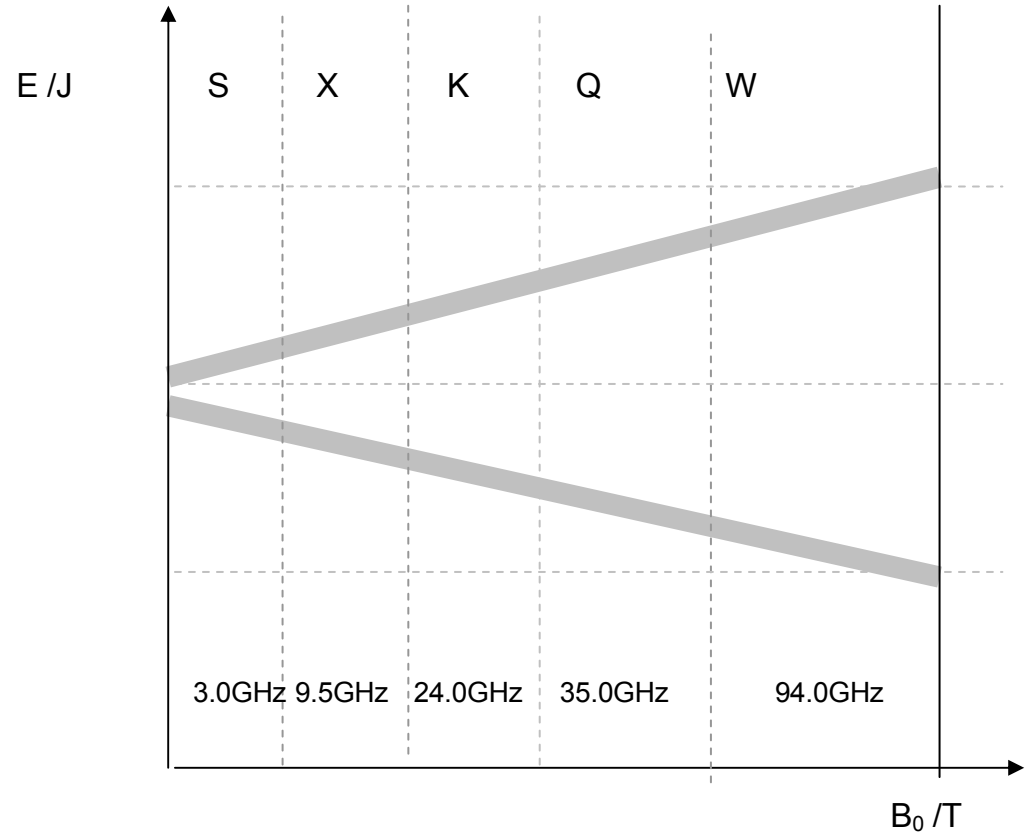

Figure 16 : Energy level splitting in a magnetic field

The splitting of energy levels is directly proportional to the external field strength. An unpaired electron can move between the two energy levels by either absorbing or emitting electromagnetic radiation (of energy hv).

At the resonance,

$$g_e = \frac{h\nu}{\mu_B B_0} \quad \textbf{(7)}$$

This equation permits a large combination of frequency and magnetic field values to be used in experiments. See below for other field-frequency combinations (**Table 2**).

Table 2. Field Frequency combinations of EPR

Band	**Frequency /GHz**	**B_0 / Gauss**
L	1.1	392
S	3.0	1070
X	9.5	3389
K	24.0	8560
Q	35.0	12485
W	94.0	33600

All the samples were run in X-band with 9.5 GHz microwave frequency.

PVG Samples

The top 30 μm layer was removed using a diamond file and was used for EPR measurement. To study the inside of PVG another 100μm layer was removed and used.

Xerogel samples

Xerogel samples were grounded and used.

MCM-41 Sample

MCM-41 samples were used as it is.

Chapter 3

3.0. RESULTS

3.1 PVG Samples

3.1.1 UV-Visible Absorption

UV-Visible absorption spectra of all PVG samples were recorded on Cary 5000 spectrometer. Spectra were recorded at a 1nm/sec scanning rate with step size of 1nm. There is no significant absorption by PVG samples below 310nm (**Figure 17** (a)). Iron impregnation shifts the absorption onset more towards lower energies (**Figure 17 (b)**), and the heat treatment shift absorption onset further towards lower energies (**Figure 17** (a) and **Figure 17** (b))

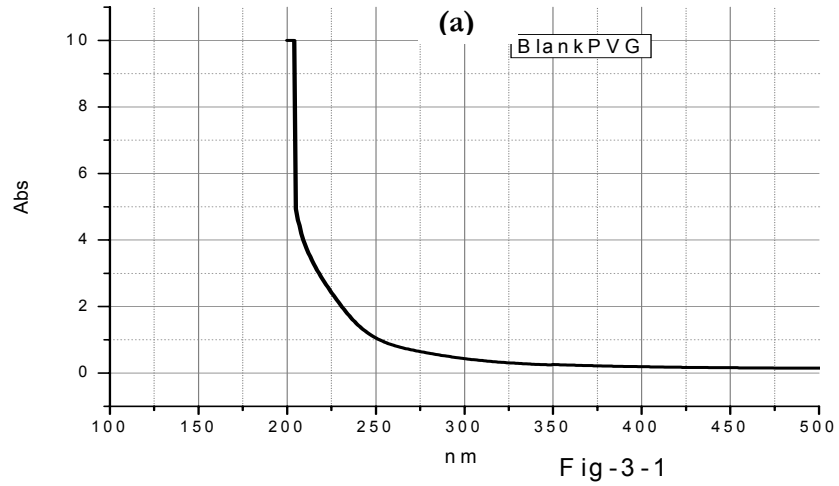

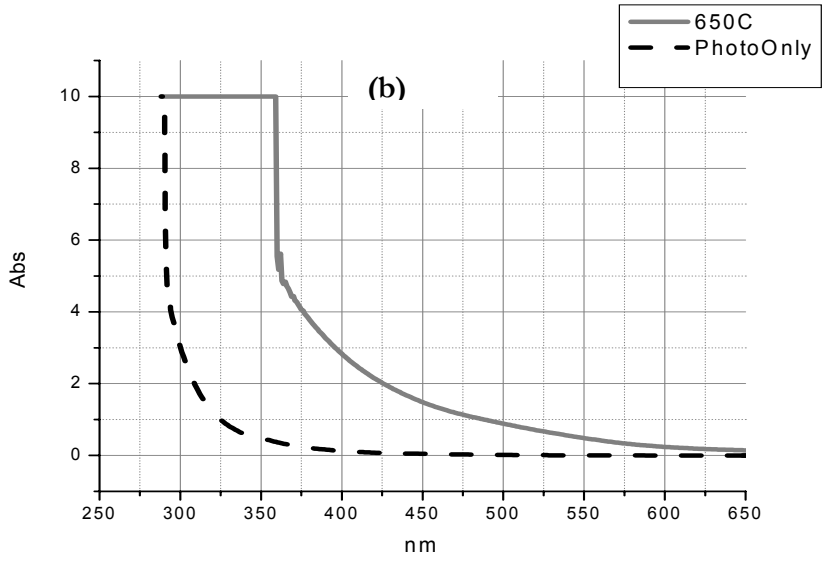

Figure 17. (a) UV-Vis Absorption spectrum of Blank PVG. (b) UV-Vis Absorption spectrum of iron impregnated PVG samples, black- before heat treatment, grey- after heat treatment (at 650^0C).

3.1.2 Fe K_α X-Ray micro Fluorescence (μ-XRF)

Sample Preparation

2mm thick PVG samples were pretreated as described in section **2.2.** Gaseous iron pentacarbonyl was adsorbed onto PVG. The iron impregnated PVG was photolyzed using a 1000W xenon lamp. Part of the sample was masked as shown in the picture below using a 2-mm thick black Teflon.

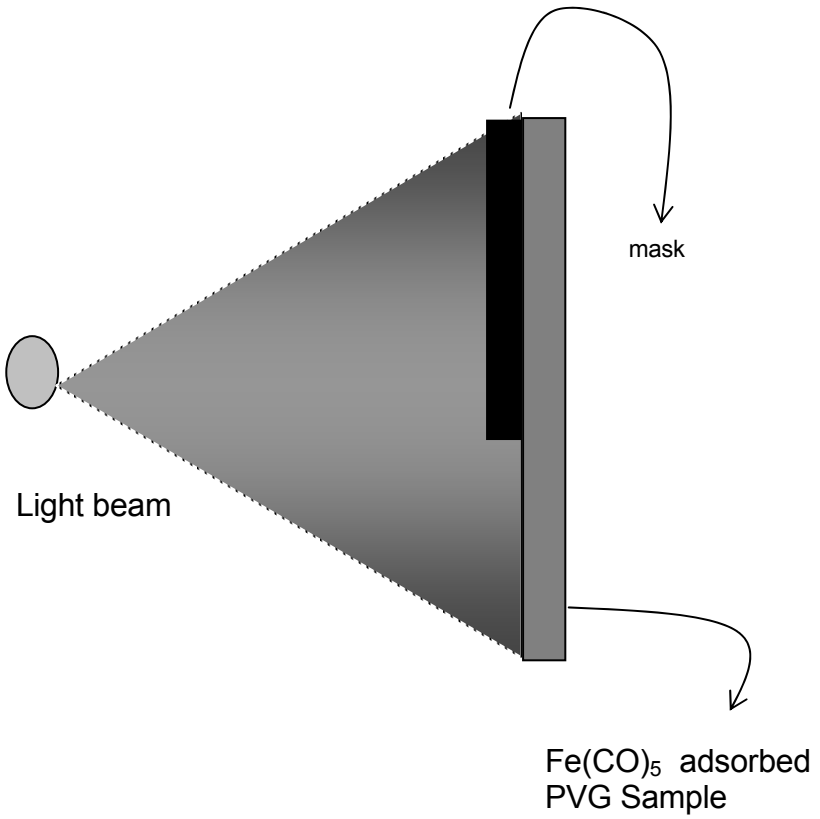

Figure 18. Iron impregnated PVG photolysing setup

X-ray microprobe Analysis

The X-ray microprobe facility at the X27A beam line at National Synchrotron Light Source at Brookhaven National Laboratory was used to study iron distribution in PVG glasses. The micro-focusing system at X27A consists of two 20-cm dynamically-bent rhodium-coated, silicon, mirrors arranged in the Kirkpatrick-Baez (KB) geometry [58] and housed within a helium-purged enclosure. The KB mirrors, 10.2 meters from the source, focus a 1mm x 1mm beam down to about 10 μm [vertical] x 15 μm [horizontal] (**Figure19**) with an average flux of $5x10^9$ ph/sec. The demagnifications in the vertical and horizontal directions are 26:1 and 55:1 respectively, and the working distance is 9 cm. The monochromator consists of two water-cooled channel-cut Si(111) and Si(311) crystals, with a four-jaw motorized slit system located immediately upstream of this arrangement. Canberra 13-element Germanium Array x-ray detector with digital signal processing technology (DSP) was used in the experiments. The experiment setup is shown in **Figure 21**. For our experiments, the step size in the Y-direction was set to 10μm and in X-the direction to 100μm (**Figure 20**).

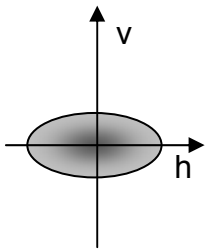

Figure19. X-ray micro probe beam sport.

.

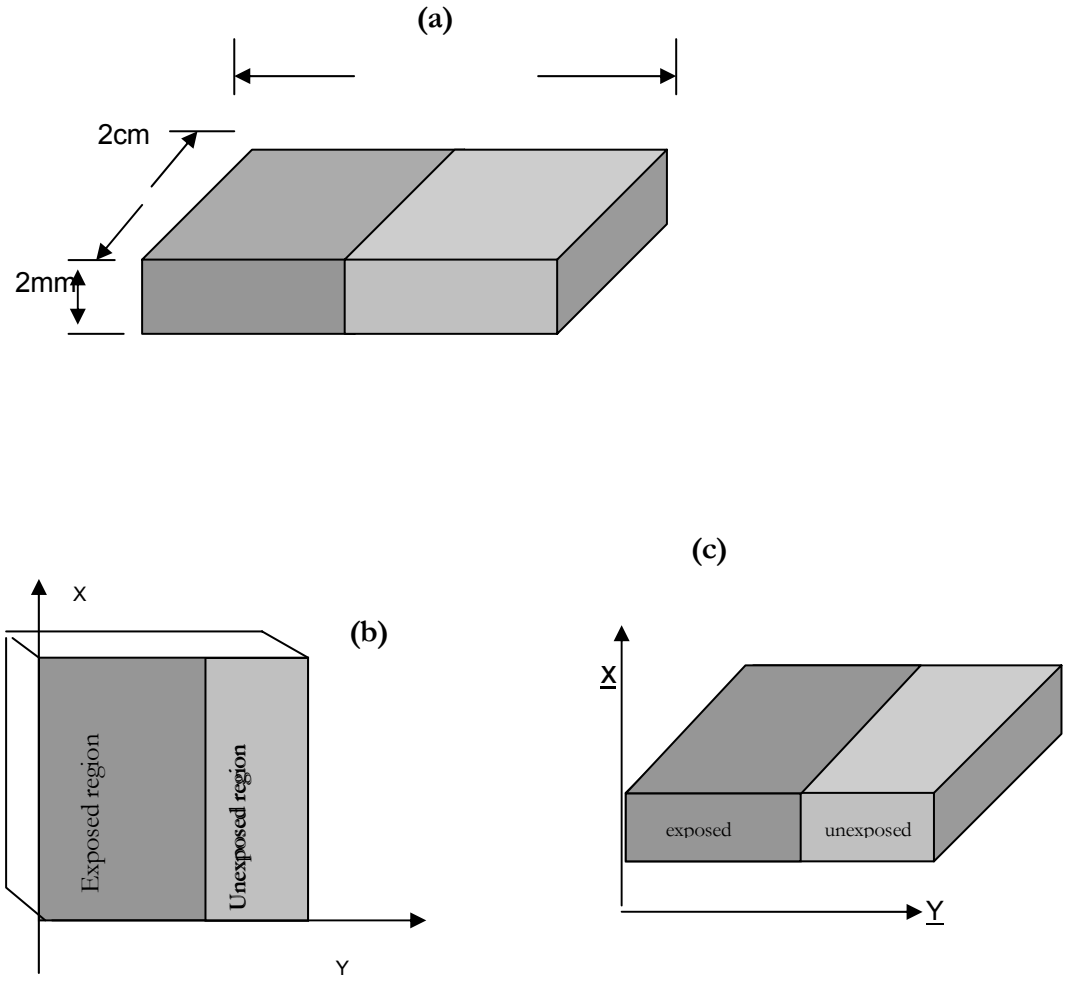

Figure 20. a) dimentions of PVG pieces used (b) Definition of X and Y direction for surface scan. (c) Definition of X and Y direction for thickness scan

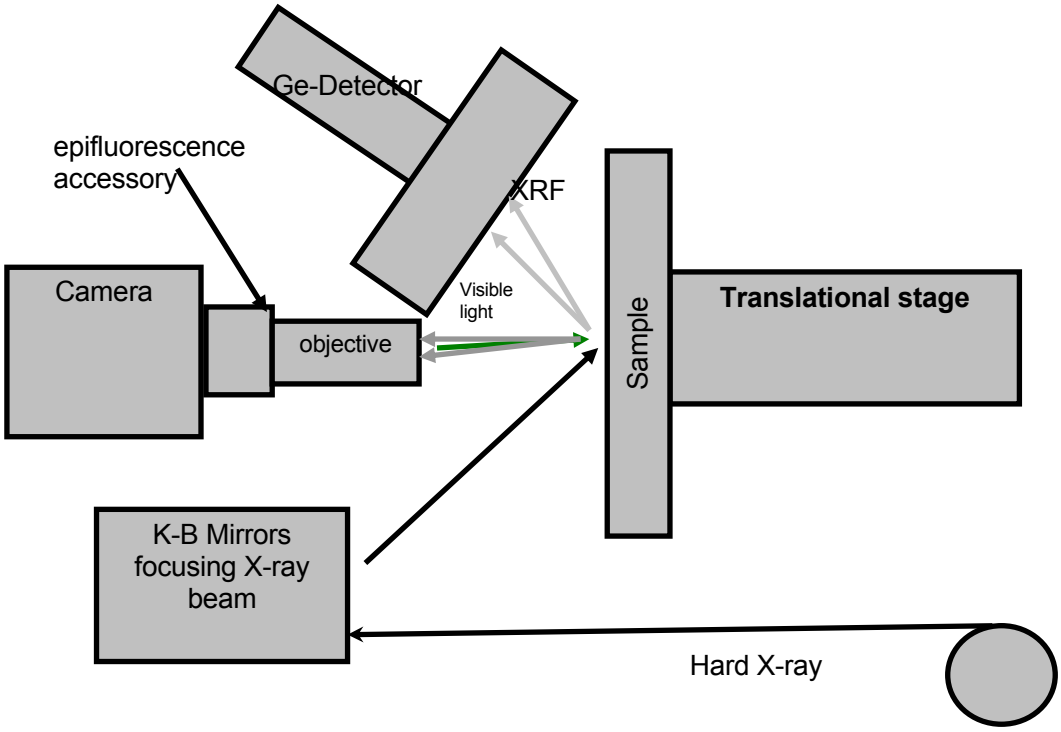

Figure 21. Experimental setup for microprobe μ-XRF study

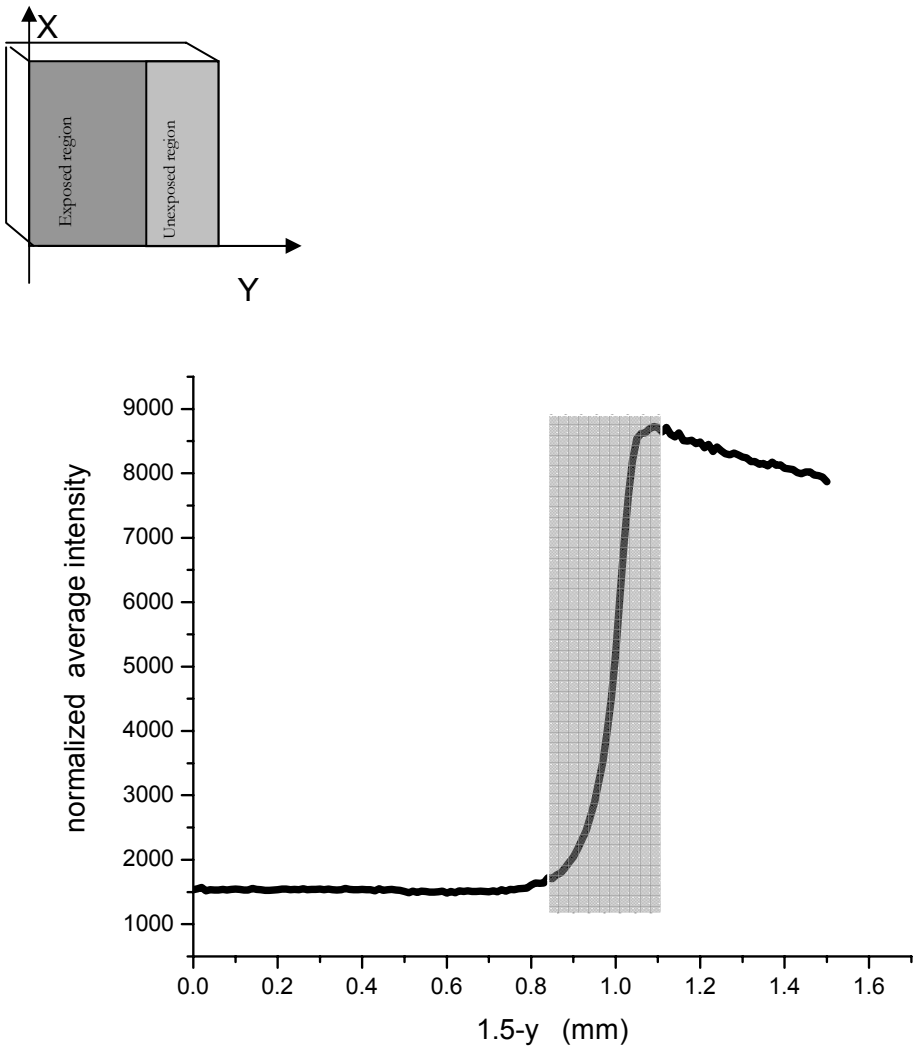

Figure 22. μ-XRF surface scan before heat treatment

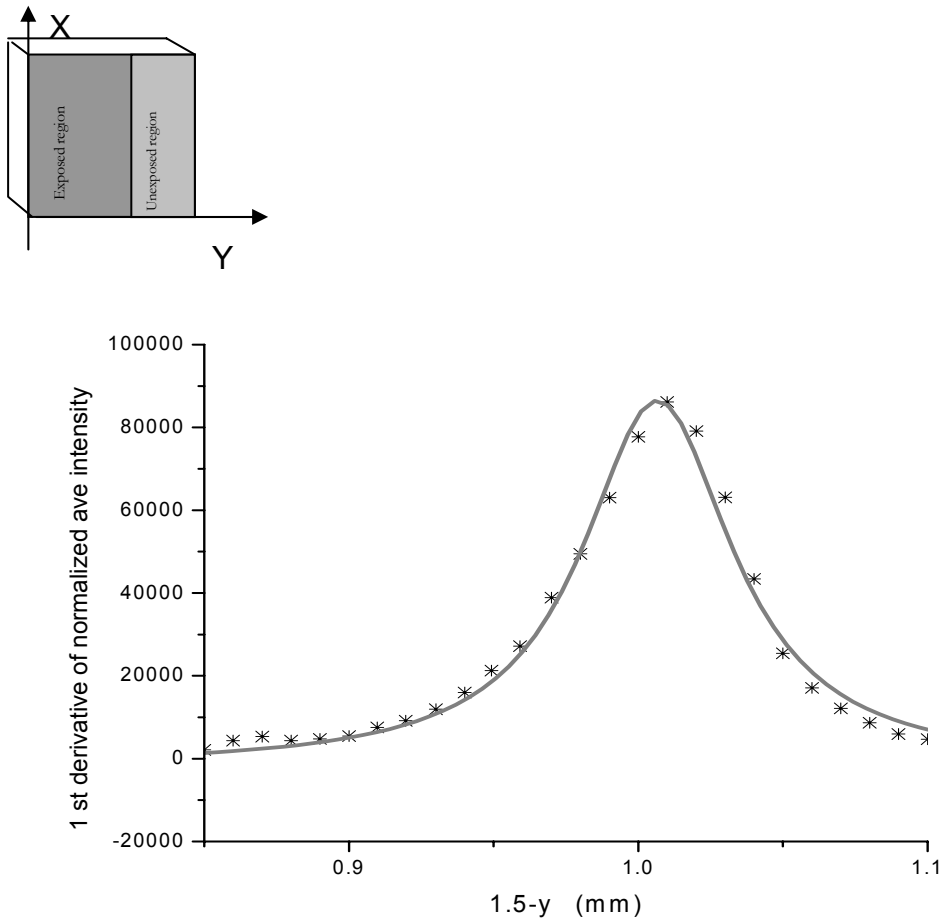

Figure 23. First derivative of μ-XRF surface scan prior to heat treatment

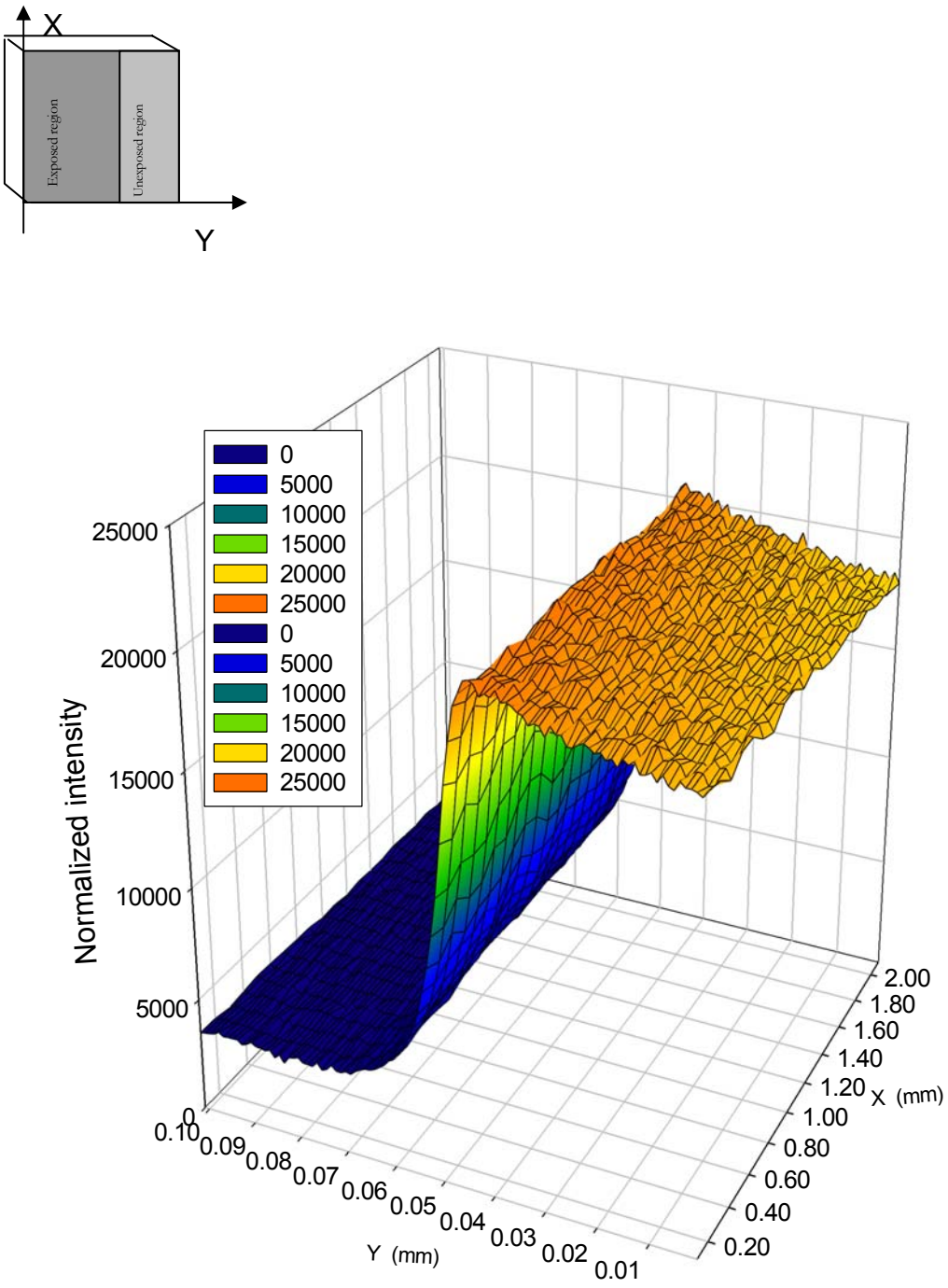

Figure 24. 2-D μ-XRF surface scan before heat treatment.

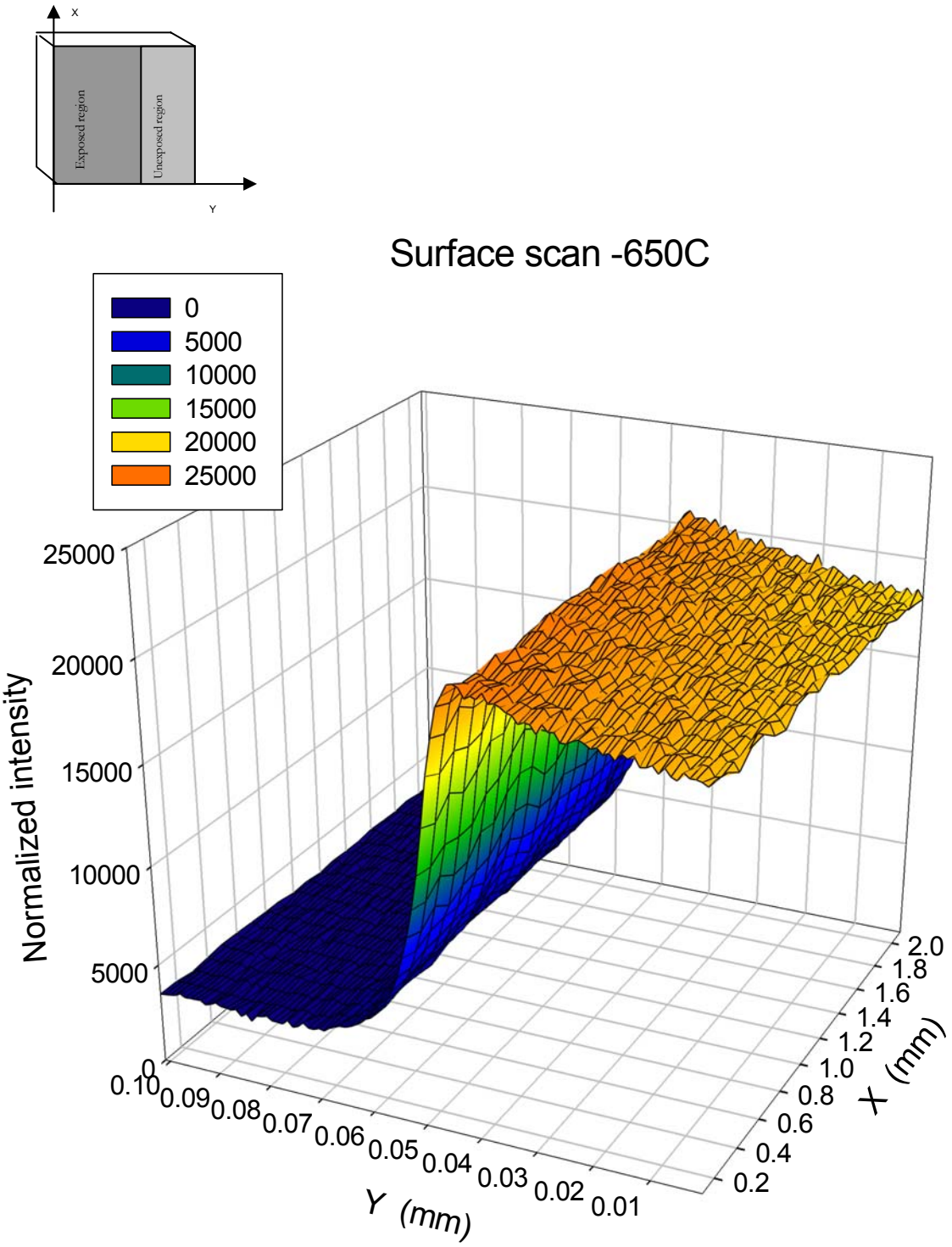

Figure 25 . 2-D μ-XRF surface scan after heat treatment.

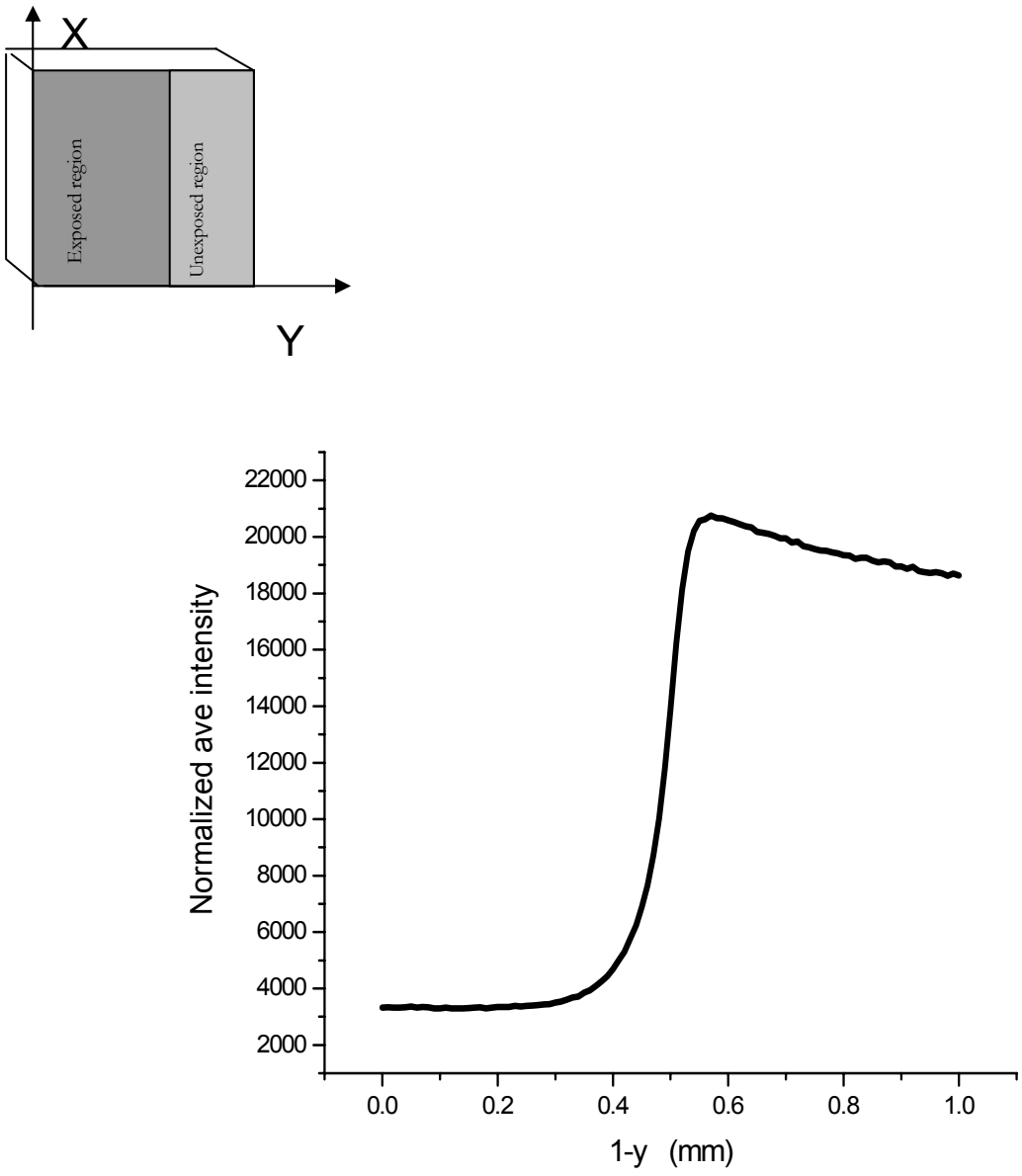

Figure 26. μ-XRF surface scan after heat treatment.

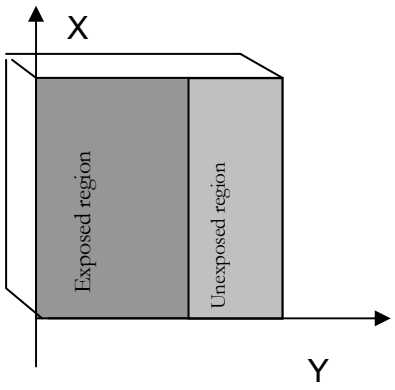

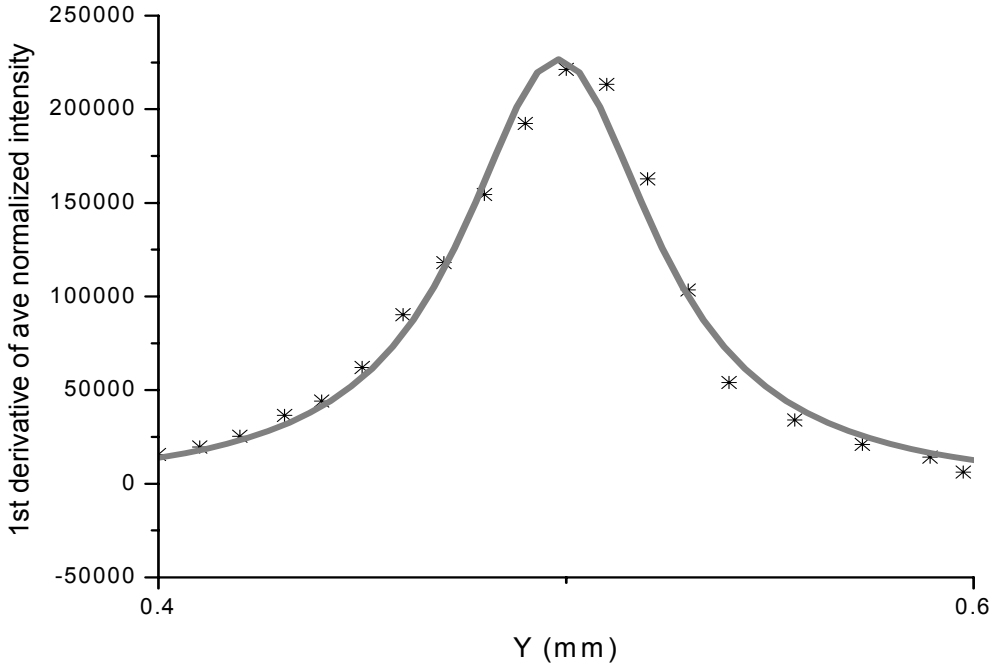

Figure 27. First derivative of μ-XRF surface scan after heat treatment.

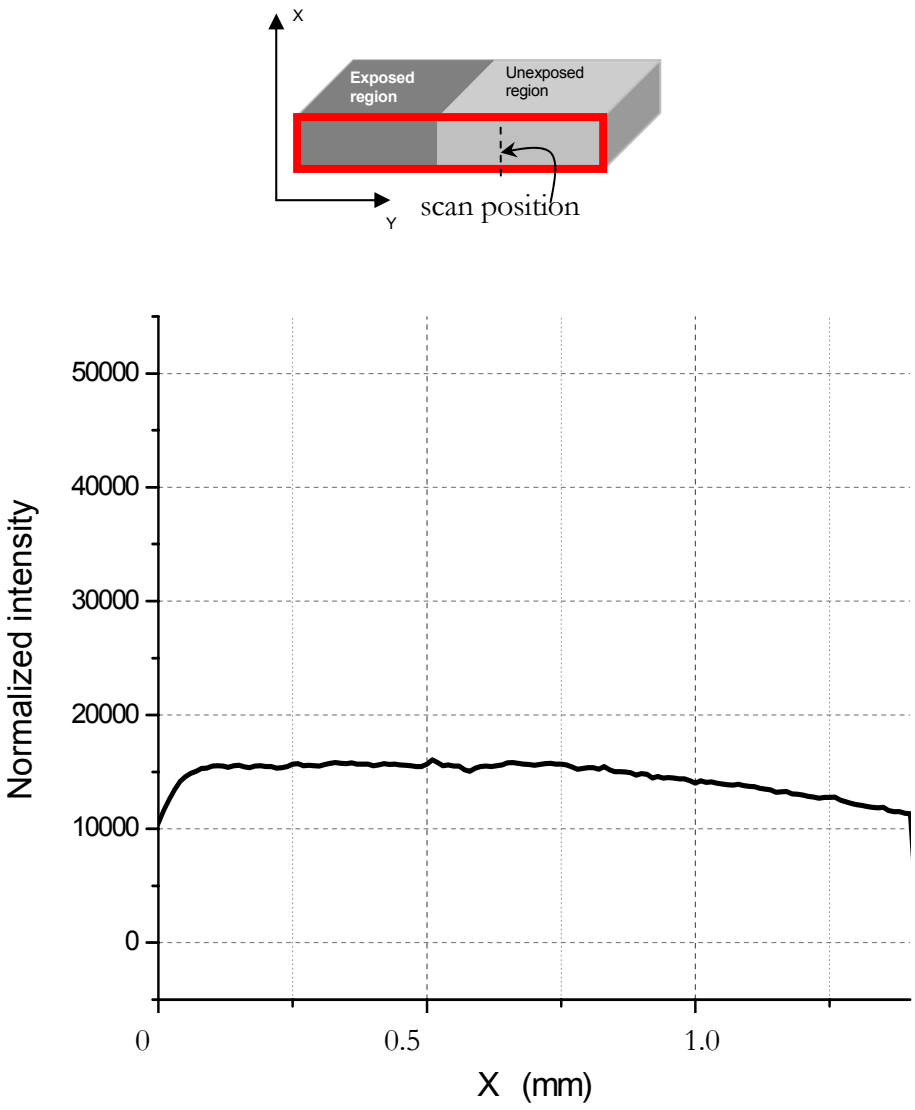

Figure 28. μ-XRF line scan of unexposed region of PVG. The X value represents the distance from the bottom edge of the sample.

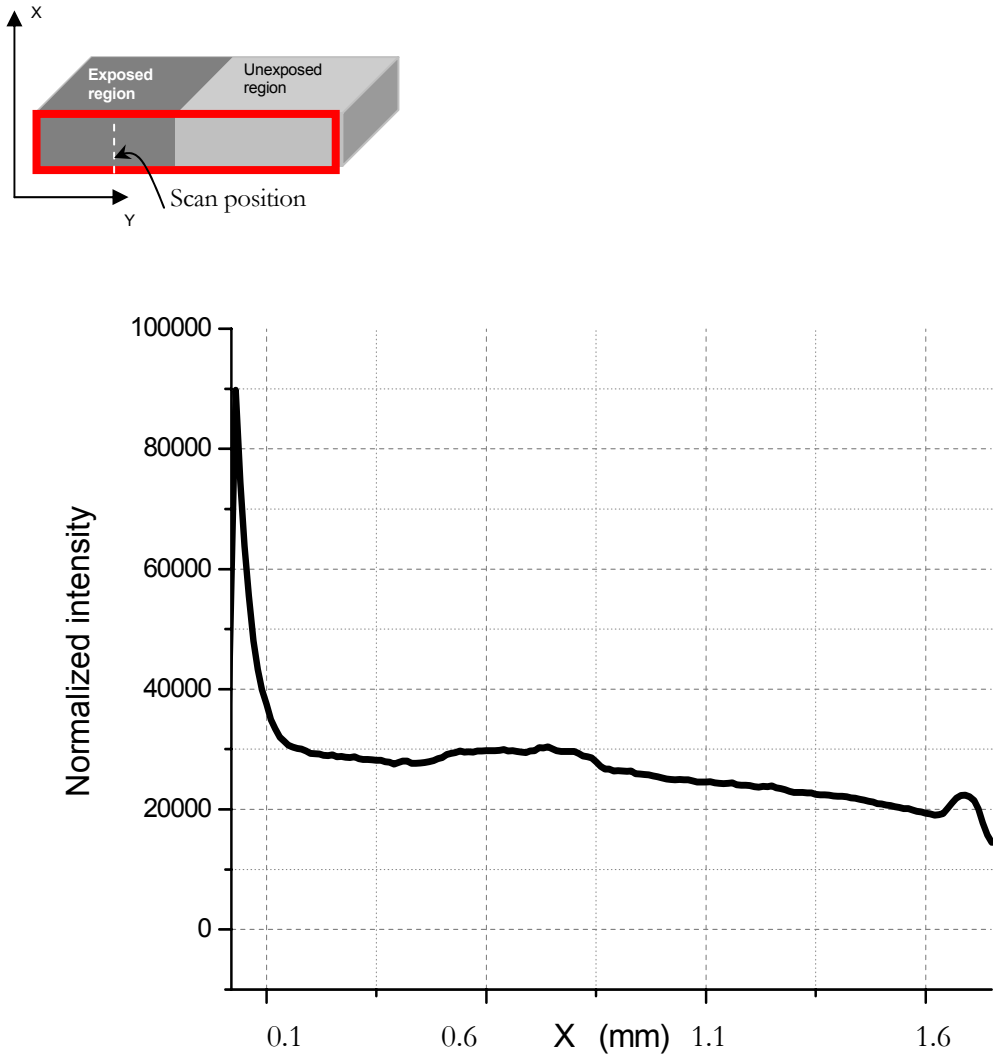

Figure 29. μ- XRF line scan of exposed region. The X value represents the distance from the bottom edge of the sample.

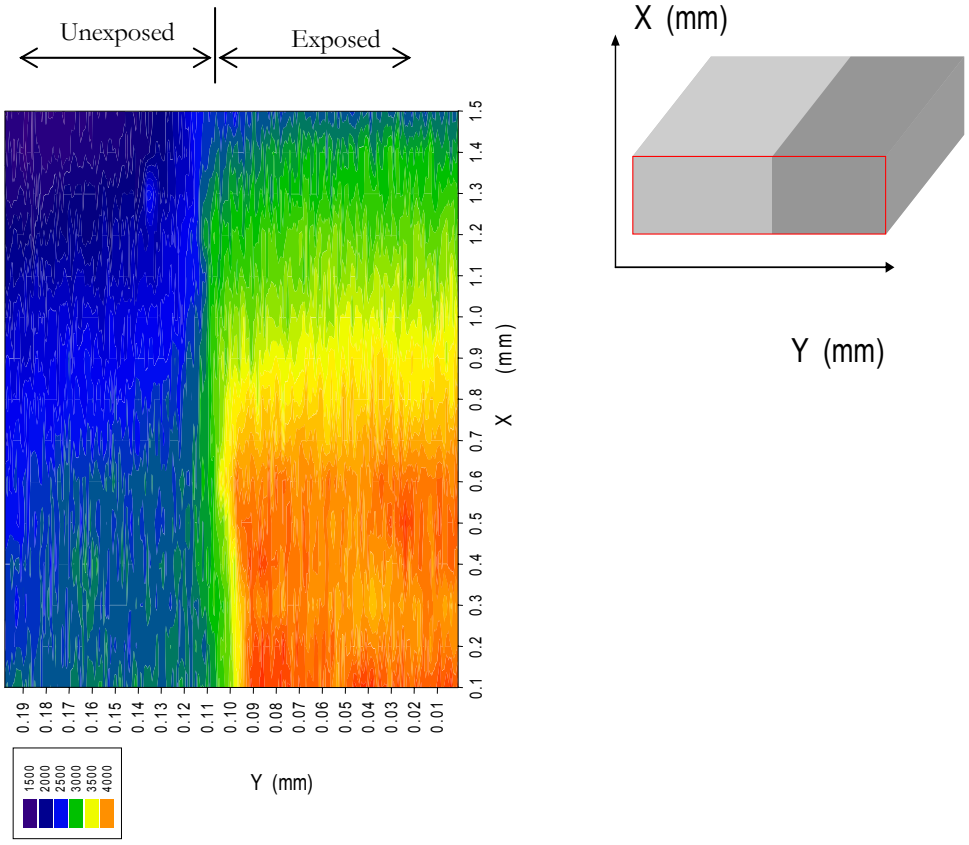

Figure 30. 2-D thickness scan of μ-XRF of Fe K_α of the 2-cmmX2-mm (thickness) side of the PVG-prior to heat treatment.

3.1.3 X-Ray Absorption Spectroscopy

PVG Samples

Samples were broken in to two equal pieces. One piece was heat treated in Thermoline programmable oven with 2^0C/min ramp up to 650^0C, four hour dwell time at 650^0C and then cooled back to room temperature at a slow rate in the furnace (**Figure 14**). The other piece was not heat treated. The X-ray Absorption Fine Structure (XAFS) spectra of the two halves were recorded in the fluorescence mode.

Table 3. PVG Samples and Treatments

Sample	**Treatment**	**Surface**
PVG-01	Photolyzed no heat treatment	Top 30μm
PVG-02	Photolyzed no heat treatment	Top 30μm removed
PVG-03	Photolyzed and heat treated	Top 30μm
PVG-04	Photolyzed and heat treated	Top 30μm removed

The XAFS spectra of PVG-02 and PVG -04 were recorded in the same setup as PVG-01 and PVG-03. XAFS spectrum of hematite was also recorded using the same setup and under the same conditions as a reference.

a) Pre-edge extraction

The XANES spectra were normalized by fitting a Victoreen function and subtracting this as background [72](**Figure 31** (a)). The spectra were then normalized for atomic absorption, based on the average absorption coefficient [72] of the spectral region from 7300 to 7500eV. The pre-edge feature was extracted by modeling the edge-jump contribution with two different model functions; an arctangent function and two –Lorentzian functions [39]. The first Lorentzian modeled the 1s-4d electronic transition while the other modeled Fe K-edge core –hole lifetime effect the edge jump. Although the extracted pre-edge shapes in both fittings the arctan and the two-Lorentzians are similar, the integrated areas were different. The two-Lorentzians better modeled the background compared to the arctangent function. Using two-Lorentzian functions to model Fe K-edge pre edge background in silicate glasses has been reported before [39]. Since the model function has no importance after extracting pre edge from the back ground, the two-Lorentzians method was used to extract the pre-edge of PVG samples and hematite standards (**Figure 31**-**Figure 35**). The extracted normalized pre edge spectrum of Hematite was deconvoluted with four pseudo-Voigt functions with two centroides near 7113.8eV and 7115.3eV and the other two above 7116eV. The components above 7116eV converge to quasi-Gaussian shapes while the others converges to 50:50 Voigt shapes (**Figure 36** and**Figure 37**). The FWHM of the two lower energy pseudo-Voigt components was about 1.5eV. The FWHM value is consistent with the values used by L.Galosiy and coworkers [68] and Wilke and coworkers [72]. The higher energy components of the deconvoluted spectra were relatively broader.

b) Pre edge intensity

Pre edge features are due to 1s$\rightarrow$3d core transitions and electric dipole and electric quadrupole transitions contribute to their intensities.

Electric quadrupole transitions are up to 100 times weaker compared to dipole transitions [69]. Though 1s-3d transitions are electric dipole forbidden, in centrosymmetric environments, these transitions gain intensity by mixing up with 4p orbitals [69]. The 3d-4p mixing enhances the intensity of low symmetry coordinations [69]. As a results quadrupole transitions are important for centrosymmetric sites which give rise to weak pre edge features. In noncentrosymmetric cases, dipole allowed transitions dominates the intensity. Thus transitions for tetrahedrally coordinated Fe are more intense than that of octahedrally coordinated Fe(III). The pre edge intensity also depends on total absorber concentration. The normalization process regularizes data with respect to variations in absorber concentrations.

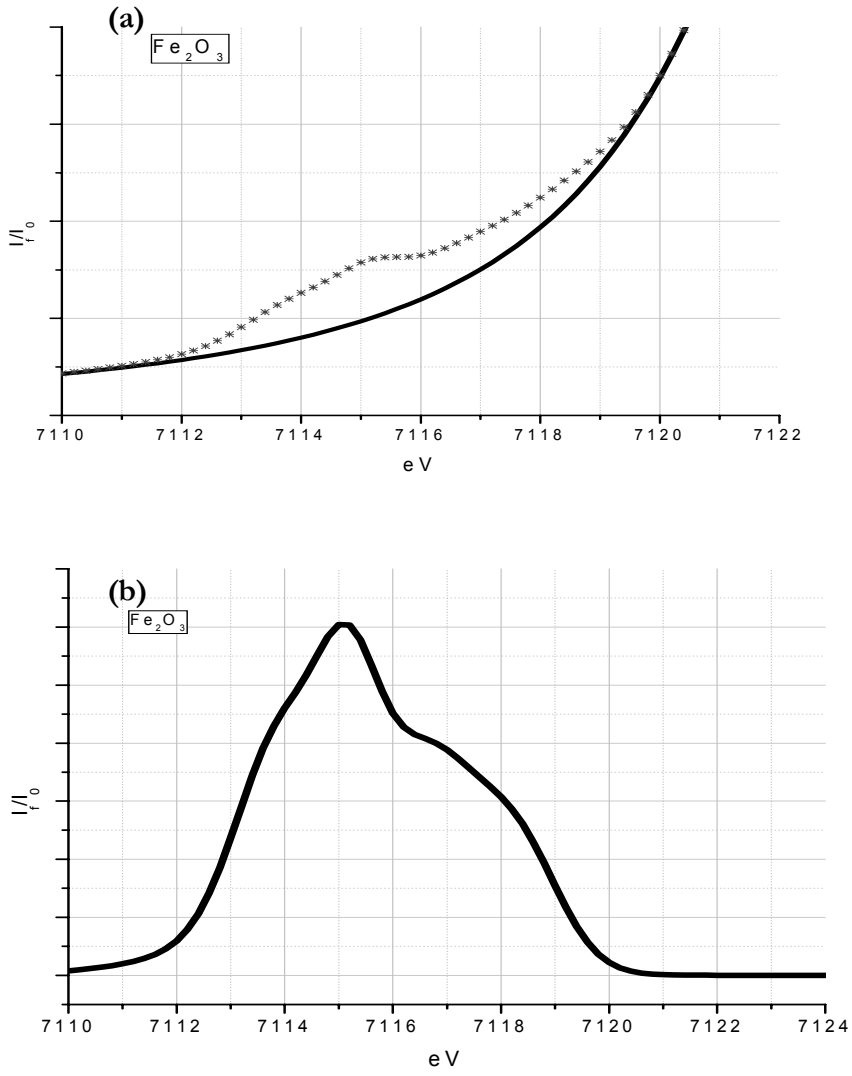

Figure 31. Pre edge of Hematite. a) Solid line-background modeled with two Lorentzians. Doted line -normalized data. b)extracted pre-edge of hematite.

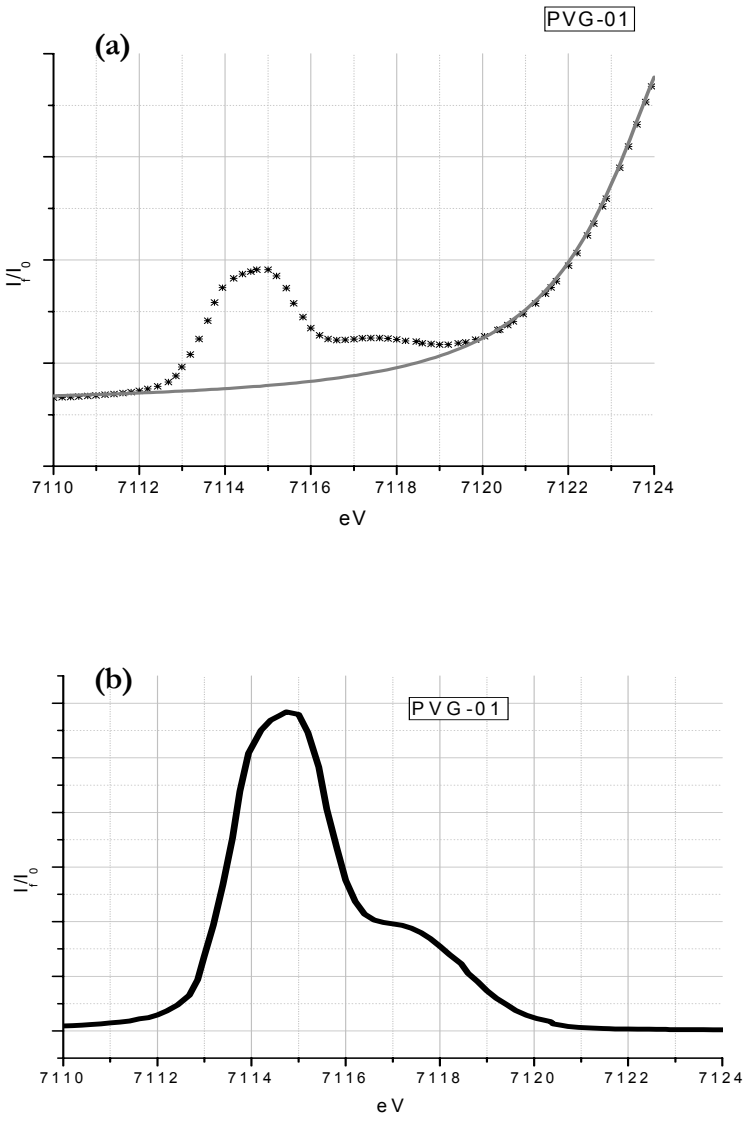

Figure 32 . Pre edge of PVG-01. a) Solid line-background modeled with two Lorentzians. Doted line -normalized data. b)extracted pre-edge of PVG-01.

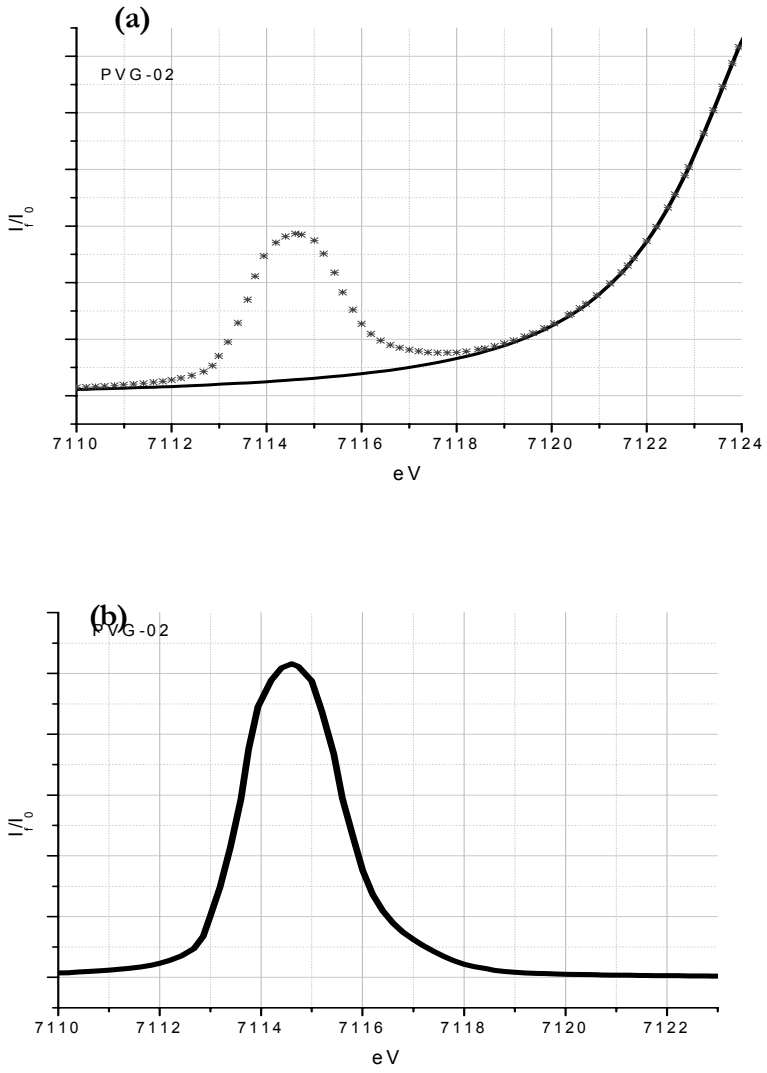

Figure 33. Pre edge of PVG -02. a) Solid line-background modeled with two Lorentzians. Doted line -normalized data. b)extracted pre-edge of PVG-01.

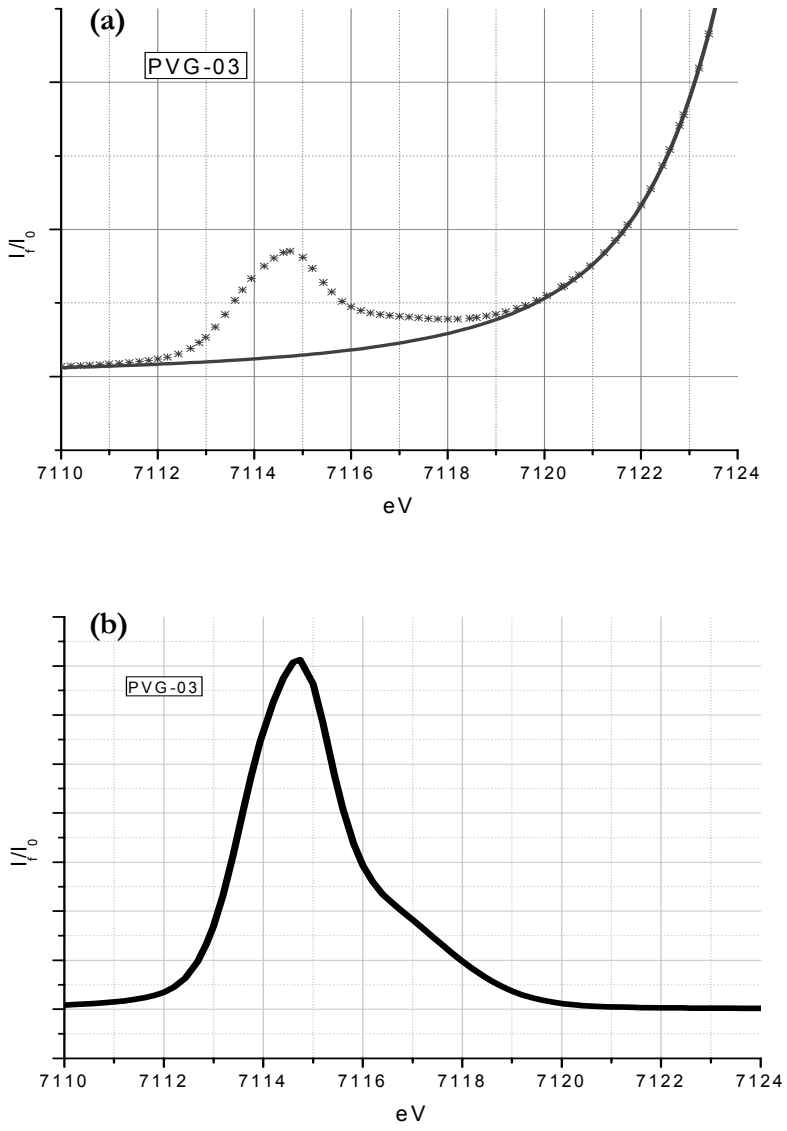

Figure 34. Pre edge of PVG-03. a) Solid line-background modeled with two Lorentzians. Doted line -normalized data. b)extracted pre-edge of PVG-03.

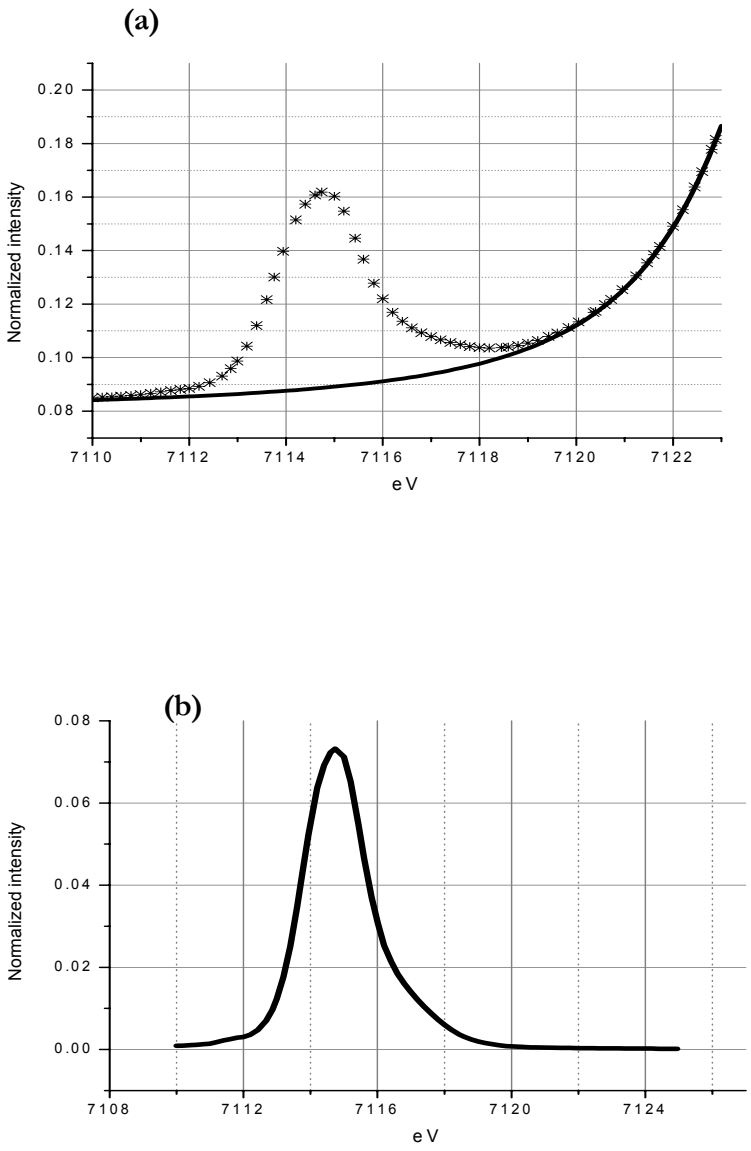

Figure 35. Pre edge of PVG-04. a) Solid line-background modeled with two Lorentzians. Doted line -normalized data. b)extracted pre-edge of PVG-04.

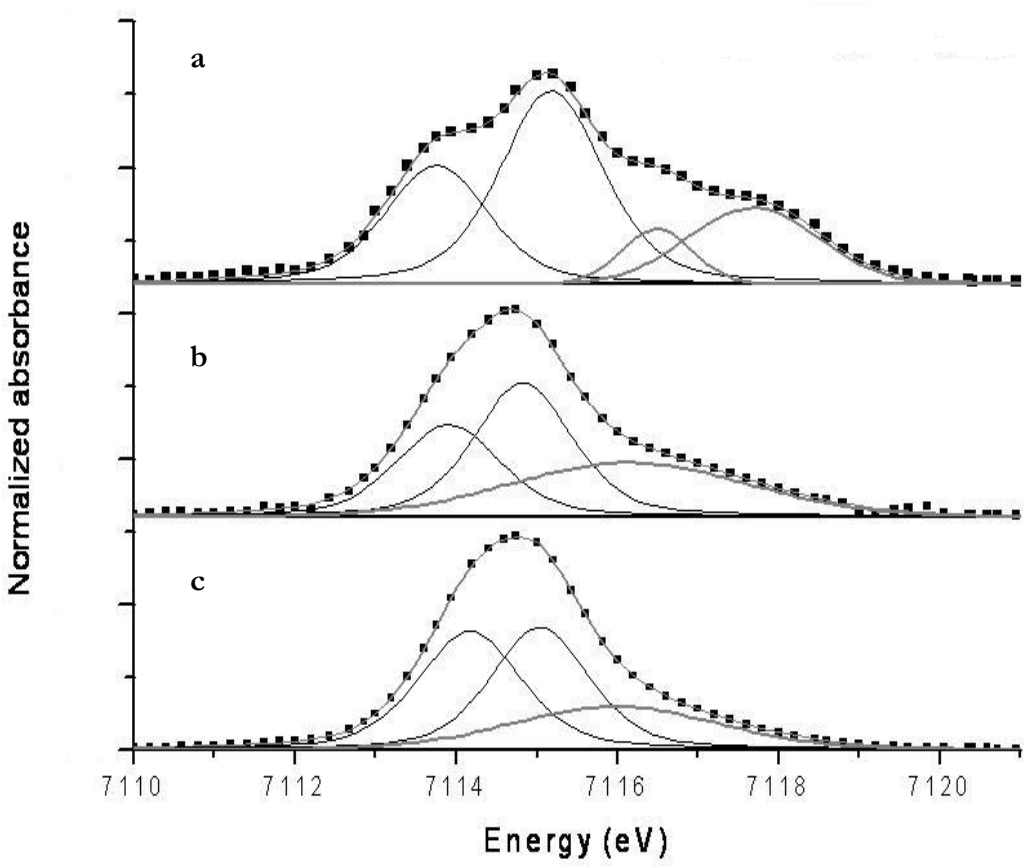

Figure 36. Deconvoluted pre-edges. a) Fe_2O_3 b) PVG-01 c)PVG02 Components are shown in grey

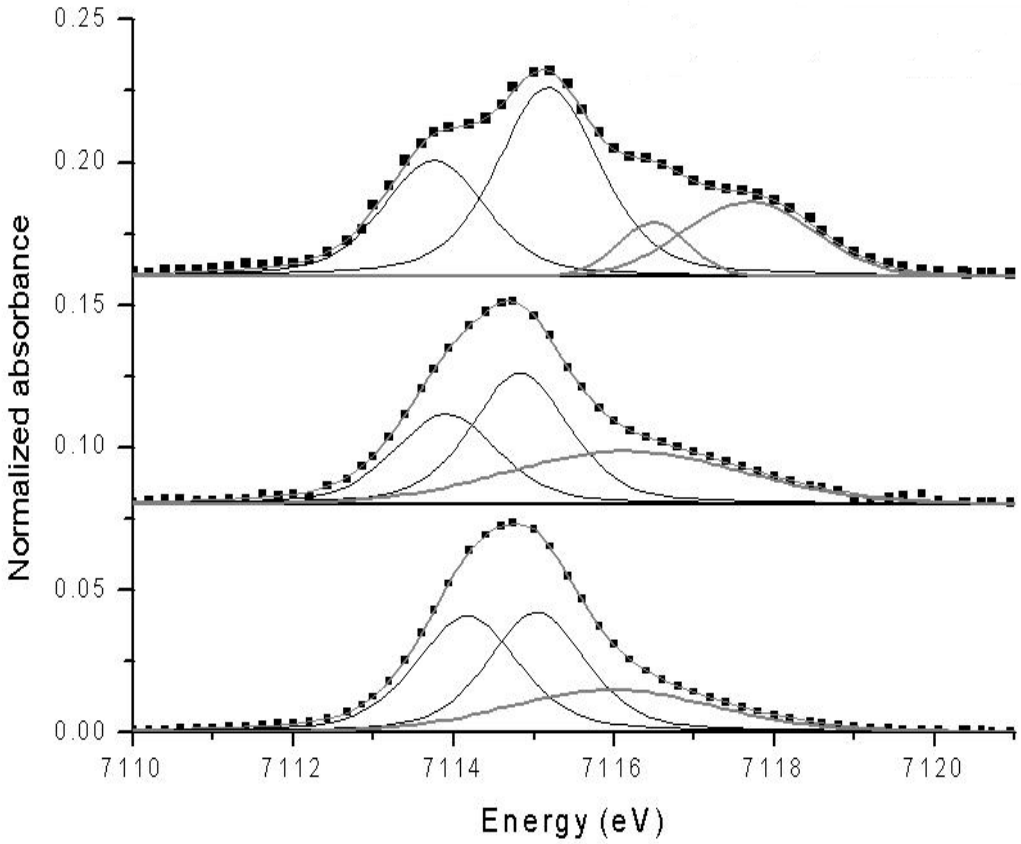

Figure 37. Deconvoluted pre-edges. a) Fe_2O_3 b) PVG-03 c)PVG-04 Components are shown in grey

c) Edge step normalization

The energy origin- E_0 is central to much of the XAFS analysis such as normalization. For this project E_0 was determined by first peak of the first derivative of μ(E) using IFEFFIT algorithm (**Figure 38**). Normalization of EXAFS data were performed as described below. A line was fit to the data in the pre-edge range and a polynomial was regressed to the data in the post edge region. The normalization constant, $\mu_0(E_0)$ was evaluated by extrapolating the pre- and post-edge lines to E_0 and subtracting the E_0 crossing of the pre-edge line from the E_0 crossing of the post edge-line. The pre-edge line was extrapolated to all energies in the measurement range of the data and subtracted from μ (E) using Athena software. The pre –edge subtracted data were then divided by edge-step parameter, $\mu_0(E_0)$.

$$\chi(E) = \frac{\mu(E) - \mu_0(E_0)}{\mu_0(E_0)} \quad \textbf{(8)}$$

This normalization process regularizes the data with respect to variations in sample preparation, sample thickness and absorber concentration. Also it allows a direct comparision of the data, $\chi(E)$ to the values of $\chi(E)$ calculated from IFEFFIT algorithm.

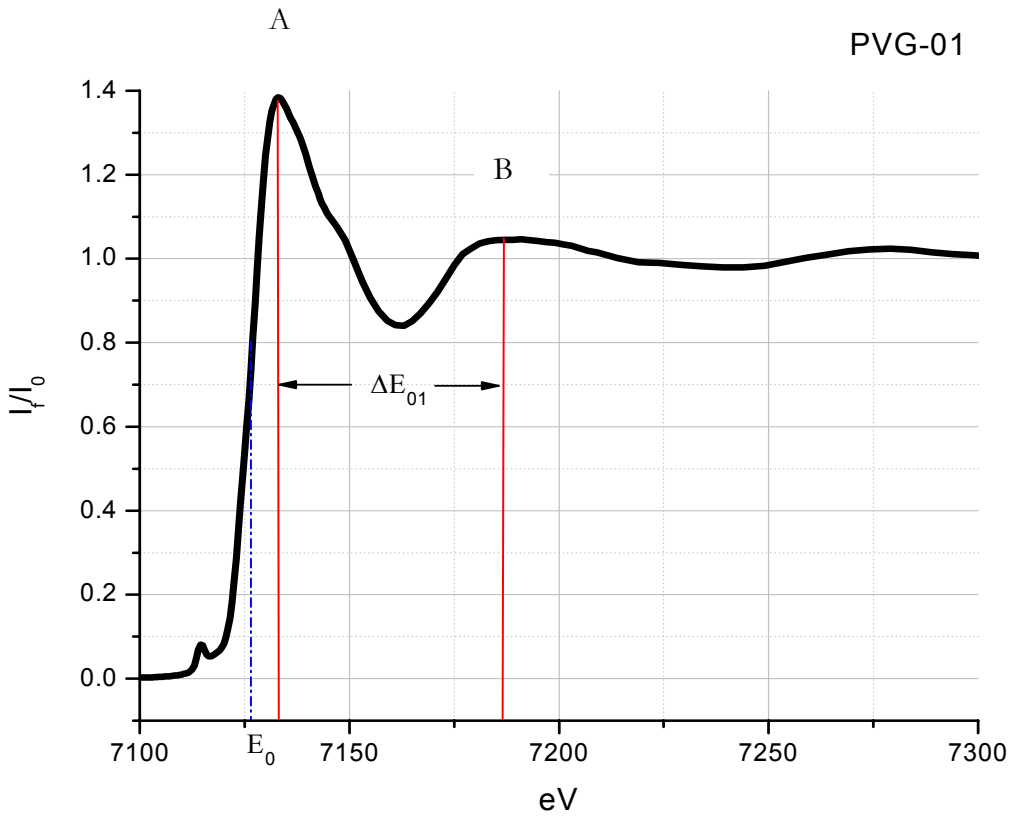

Figure 38. Flattened XANES spectrum of PVG-01. A-first strong resonance, B-shape resonance E_0 –energy origin or threshold energy.

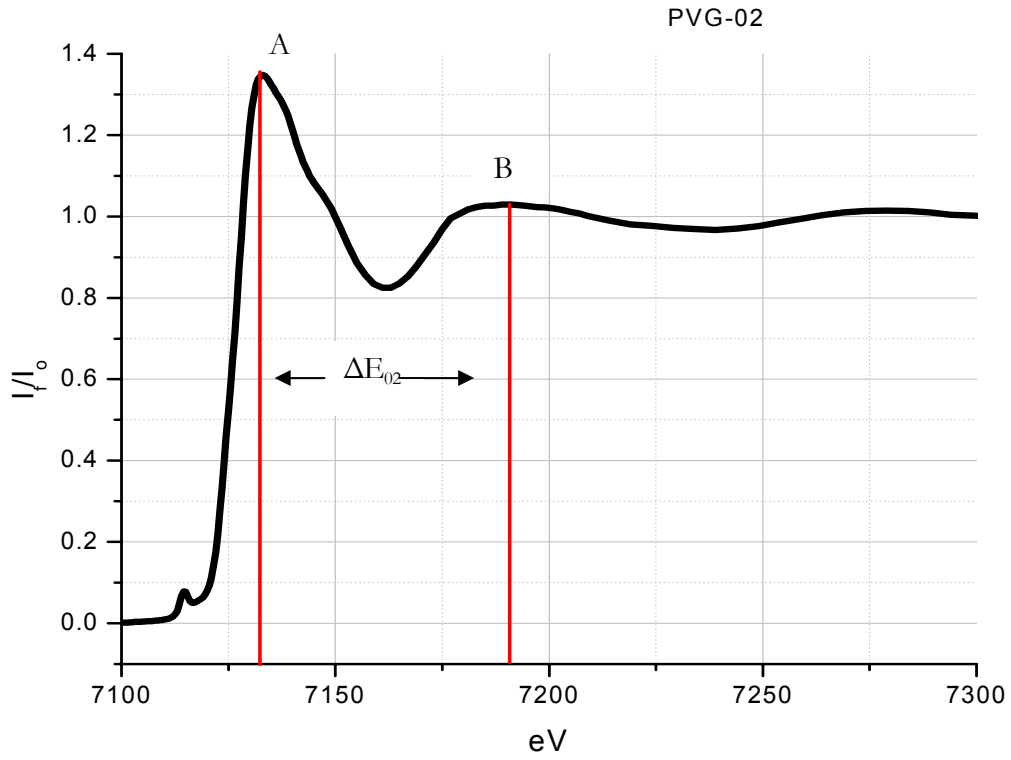

Figure 39. Flattened XANES spectrum of PVG-02. A-first strong resonance, B-shape resonance.

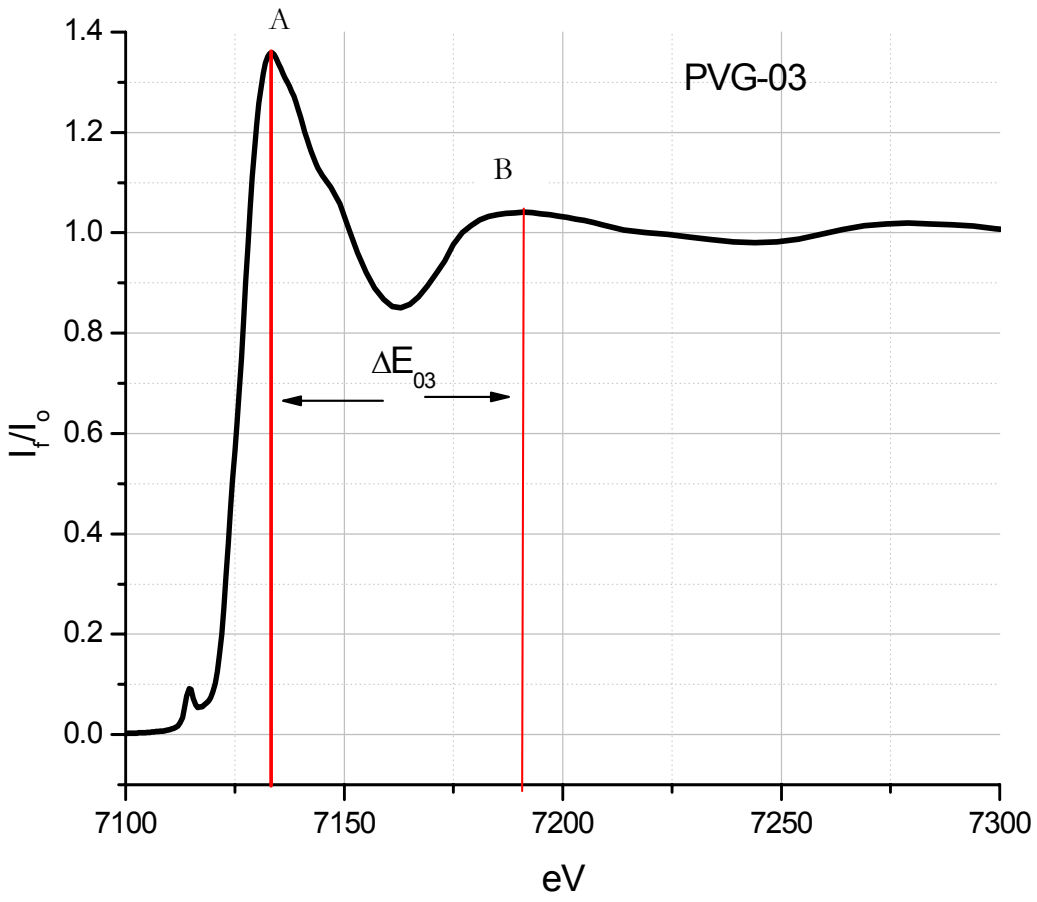

Figure 40. Flattened XANES spectrum of PVG-03. A-first strong resonance, B-shape resonance.

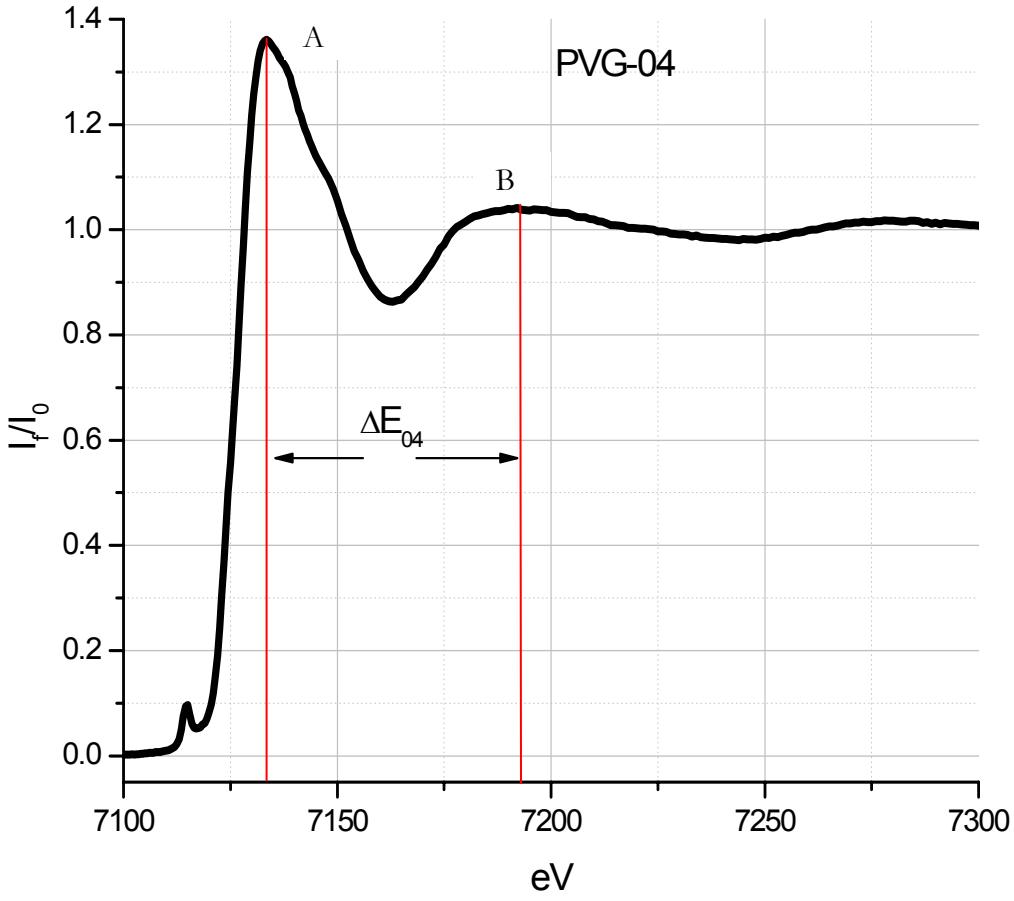

Figure 41. Flattened XANES spectrum of PVG-04. A-first strong resonance, B-shape resonance.

d) Edge and Pre-edge energies

The main K edge crest and threshold energies in the XANES region are sensitive to oxidation states of absorbing atoms [66]. Therefore this can be used to probe oxidation states of the absorbing atom. The white line energy of, Fe(III) bearing minerals are reported to be around 20.45±0.95 eV higher relative to Fe K edge, 7112eV [71,72]. Fe(II) bearing minerals show about 9.45±0.55eV shift from the Fe K-edge [71,72].

Final energy states in 3d orbitals are less sensitive to local coordination environments than higher energy final states [59].Therefore, main edge features and their energies are more sensitive to local coordination environments than pre edge energies [59]. Thus in this study edge energy was not used as a sole determinant of oxidation states.

The pre edge centroid position of Fe(II) is about 2eV lower in energy compared to that of Fe(III) [72]. The pre-edge centroid position of Fe(II) minerals are reported to be around 7112.8±0.6 and the pre edge centroid position of Fe(III) bearing minerals is reported to be around 7115.0±0.4 [71, 72].

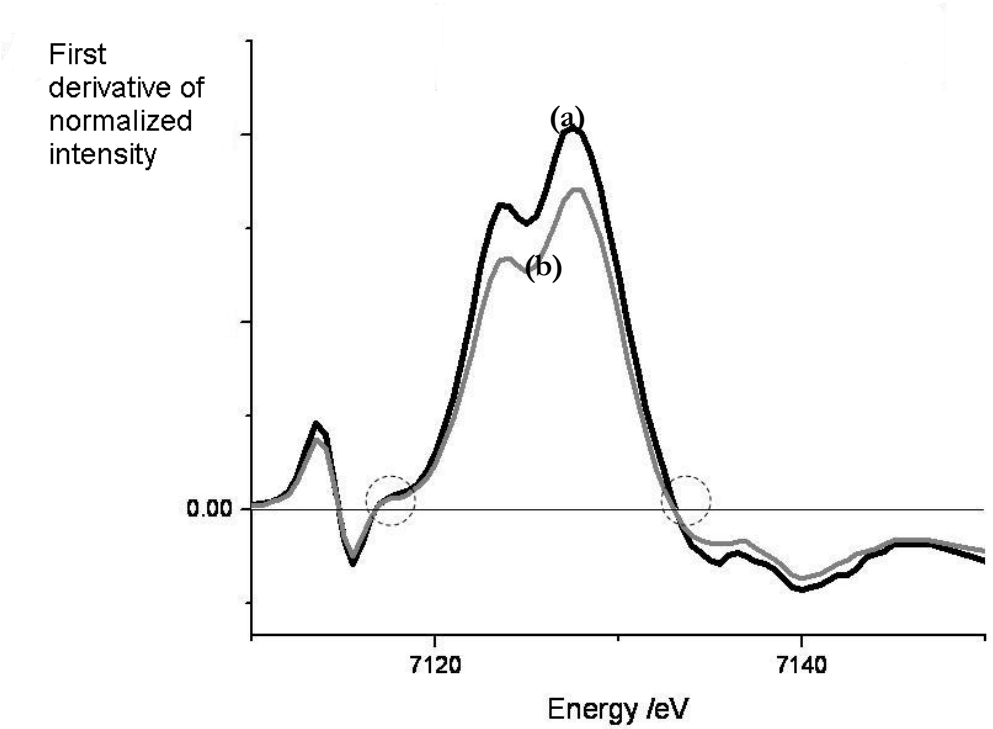

Figure 42 . First derivatives of normalized XAF intensities. (a) PVG-01 and (b) PVG-02. Doted circles shows the (left) pre-edge centroid position and the (right) first strong resonance peak.

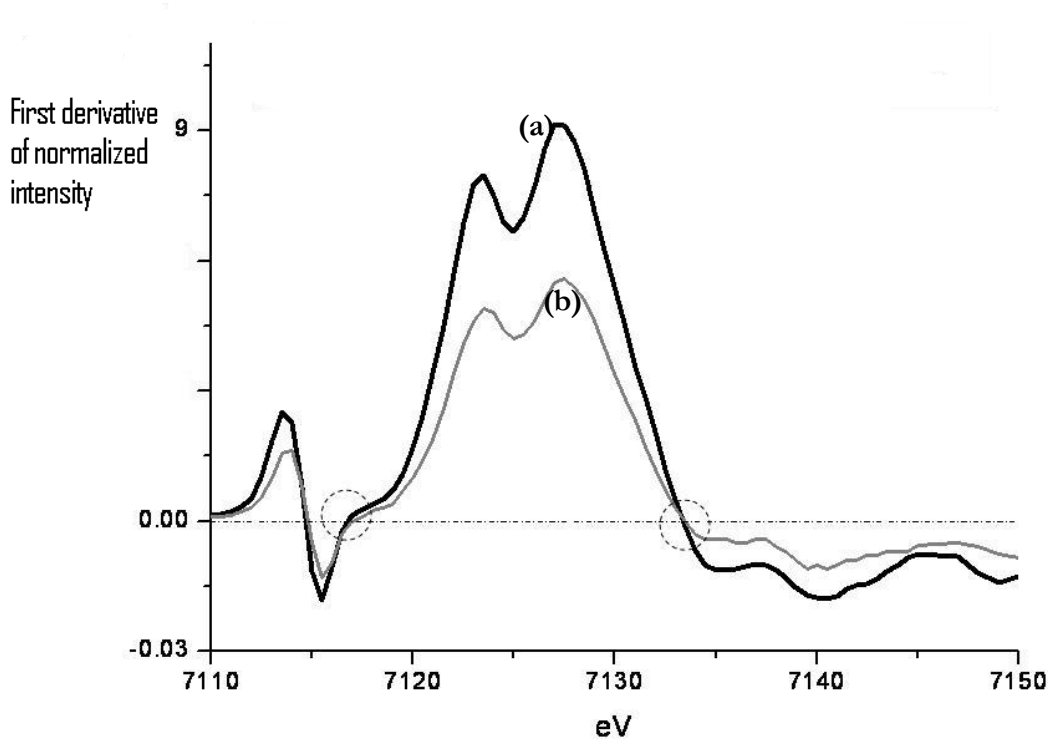

Figure 43 . First derivatives of normalized XAF intensities. (a) PVG-03 and (b) PVG-04. Doted circles shows the (left) pre-edge centroid position and the (right) first strong resonance peak.

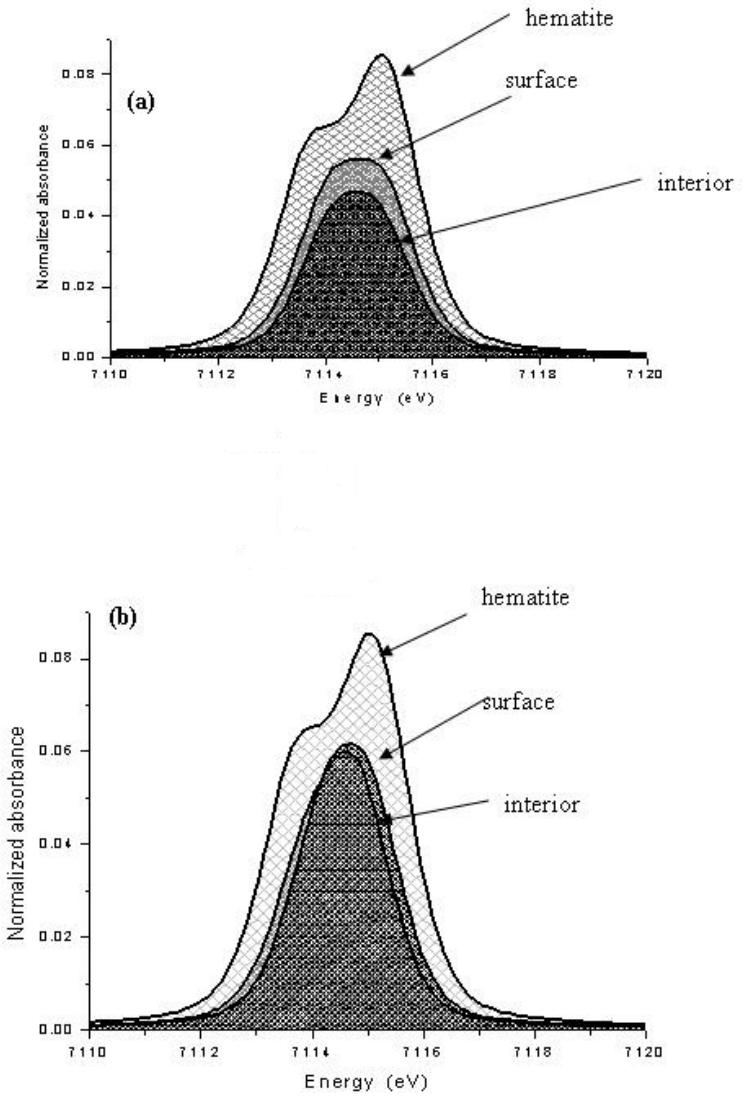

Figure 44 . Comparison of normalized 1s→3d transition intensities of surface and interior of PVG samples. A)Before heat treatment B) After heat treatment.

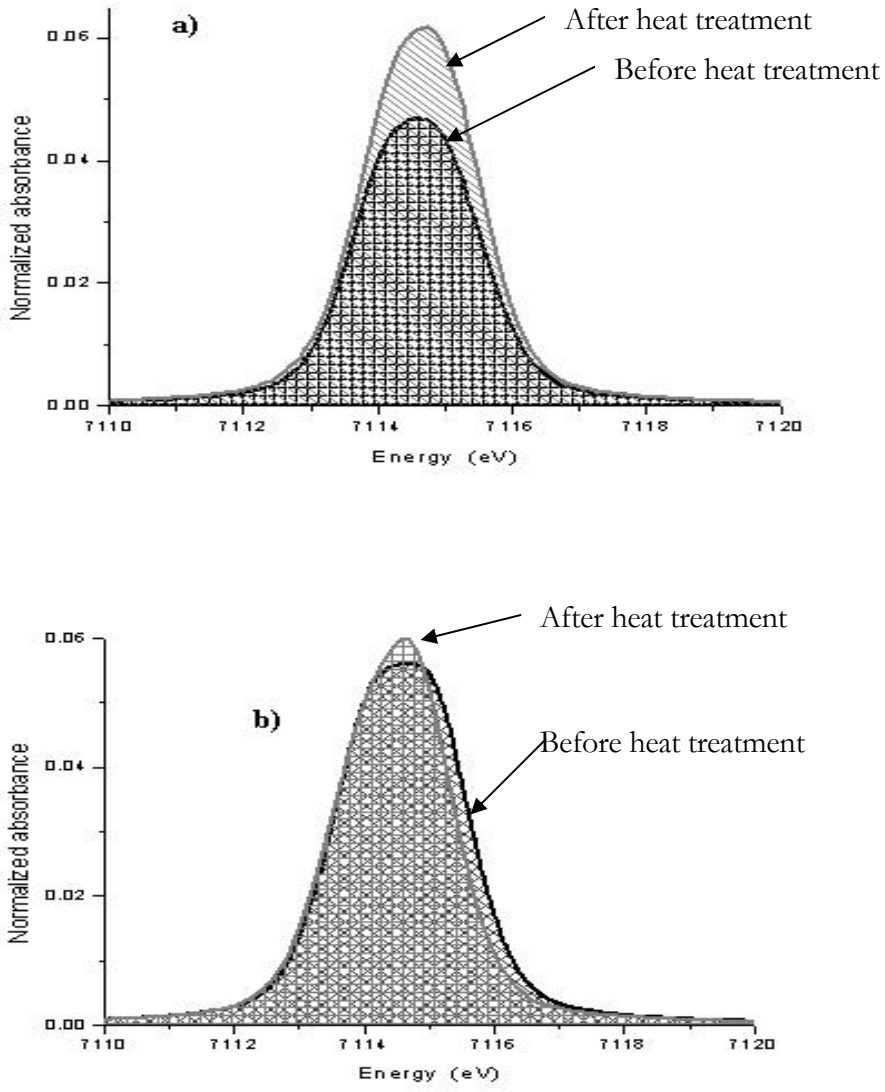

Figure 45. Comparison of normalized 1s→3d transition intensities of before and after heat treated PVG samples. A) Interior B) surface.

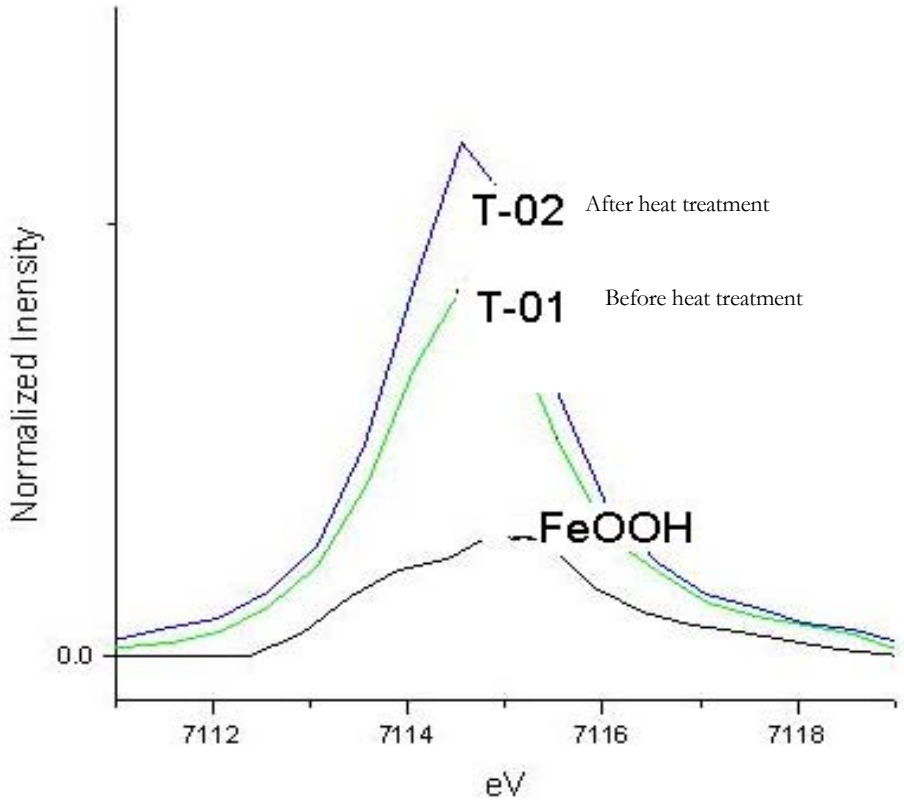

Figure 46. Normalized pre edge intensity of Fe-MCM-41 samples in comparison to FeOOH centrosymmetric standard. T-01 iron impregnated photolyzed MCM-41 before heat treatment. T-02 iron impregnated photolyzed MCM-41 after heat treatment.

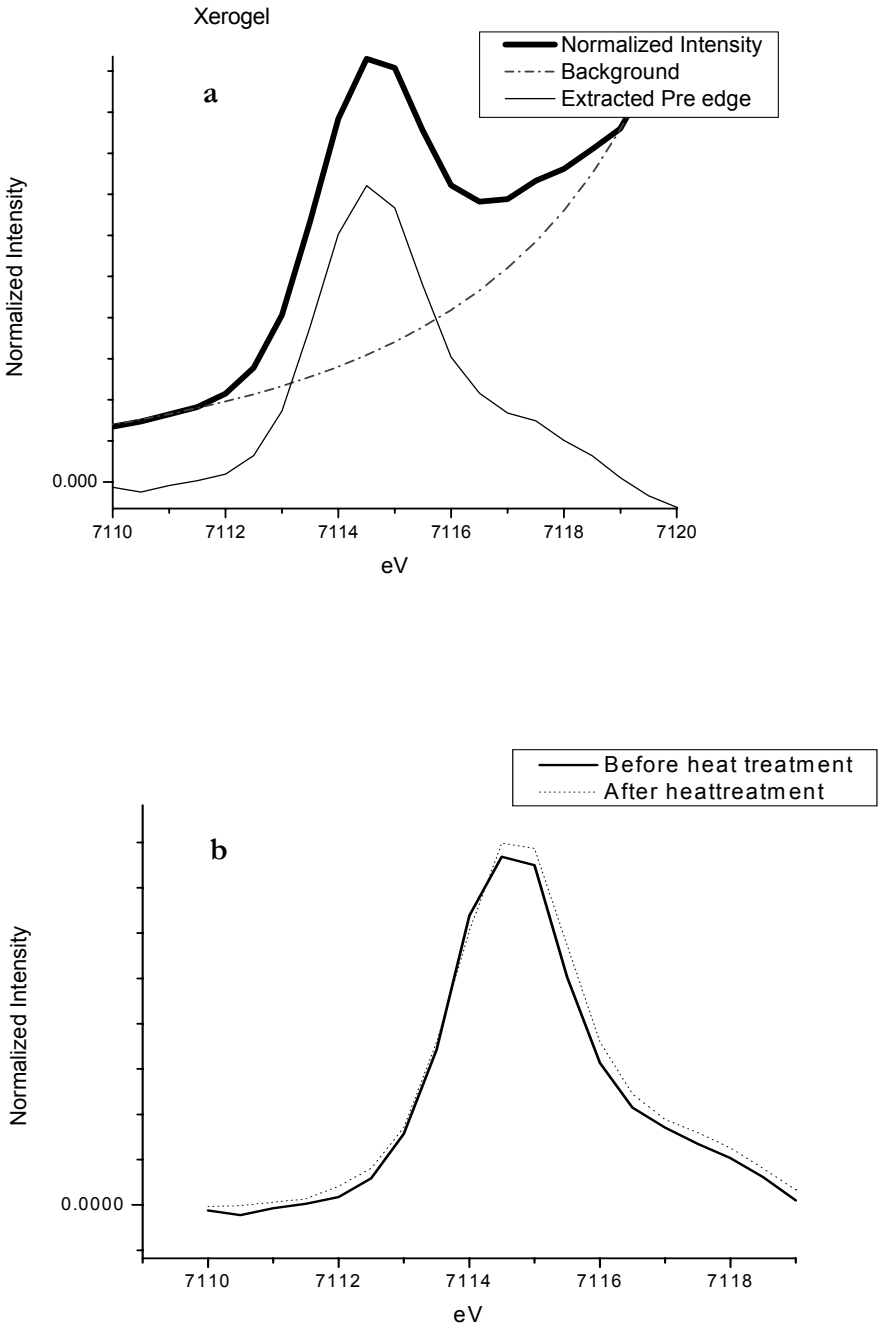

Figure 47. Xerogel Pre edge. a)Xerogel Pre edge extraction b) Extracted pre edges of before and after heat treated samples.

e) EXAFS

The Fourier transformation of $\chi(k)$ is related to scattering path lengths and can be expressed as follows:

$$\chi(k) = \sum_j \left(\frac{N_j}{kR_j^2} \right) S_0^2(k) f_j(k) e^{-2\ \sigma_j^2 k^2} e^{-2R_j/\lambda(k)} \sin(2kR_j + \delta_j(k)) \quad \textbf{(9)}$$

where k is the photoelectron wave vector, N_j is the number of scattering atoms at distance r_j from the absorber atom, S_o^2 is an amplitude reduction term called passive electron reduction factor and is due to the relaxation of all the other electrons in the absorbing atom to the hole in the core level. The factors $f_j(k)$, $\delta_j(k)$, $\lambda(k)$ are the backscattering amplitude function, energy dependent phase shift of the photoelectron wave, and the mean free path of photo electron of the jth atom, respectively. The term $exp\ (-2\sigma^2_j k^2)$ is the Debye-Waller factor, which includes thermal and static disorder terms with the root mean square displacement, σ_j., and $exp\ (-2r/\lambda)$ accounts for the loss of photo-electrons to inelastic process. The wave vector,

$$k = \sqrt{2m/\hbar^2 (E - E_0)} \quad \textbf{(10)}$$

where E is the energy of incident photon, E_0 is the absorption threshold energy and m is the mass of an electron.

The sum is over shells of atoms or scattering paths for the photo electron. The aim of EXAFS analysis is to obtain unknown parameters of the above equation by fitting it to experimental $\chi(k)$ values define by $\chi(k) = \frac{\mu(k) - \mu_0}{\mu_0}$.

A weighting factor of k^3 is applied to the normalized $\chi(k)$. The Fourier transform of the so generated EXAFS signal gives a pseudo-radial distribution function (RDF) around Fe atoms [60]. The positions of neighboring atoms may

shift by a small amount due to phase shift of photoelectron wave function. Therefore, bond lengths were determined based on fitting of RDF. For PVG, $\chi(k)$ is assumed to be a linear combination of $\chi(k)_{Fe(0)}$ and $\chi(k)_{FeO}$ [73]. The EXAFS function fittings can not be used to determine the coordination number (N) and the passive electron reduction factor $(0.7< S_o^2 < 1.0)$ at the same time due their strong correlation [61]. This and other experimental and theoretical issues, make EXAFS amplitudes and therefore N, less precise than EXAFS phase, and therefore R. Therefore, S_o^2 was fixed at a reasonable value such as 0.9 even though this may introduce an additional error of about 10% on the values of N obtained from the analysis.

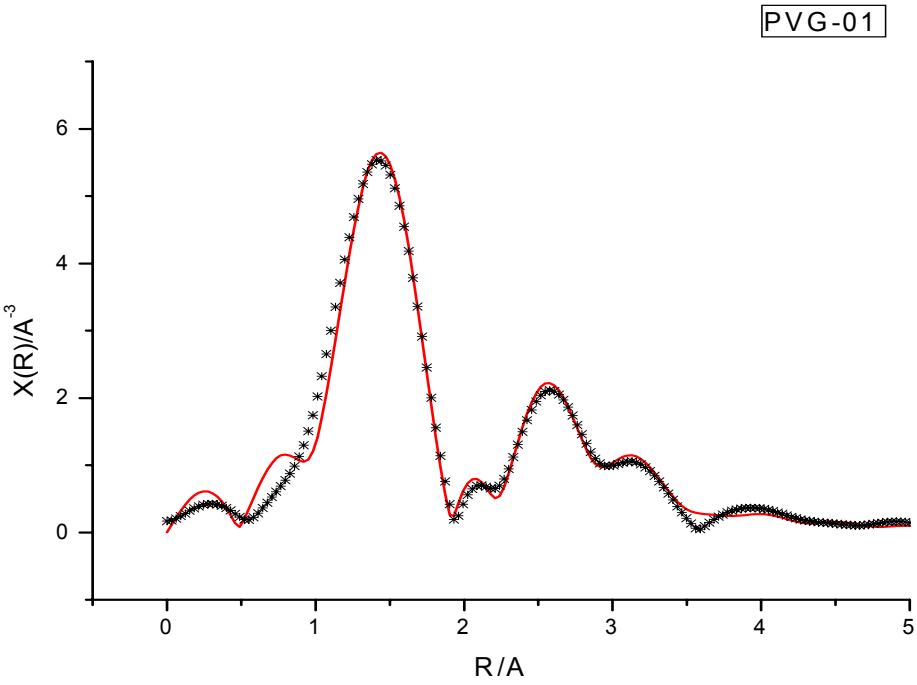

Fig.-13 a

Figure 48. k^3 weighted EXAFs data and theatrical fit of PVG-01. The line represents the theoretical fit of the data points (∗).

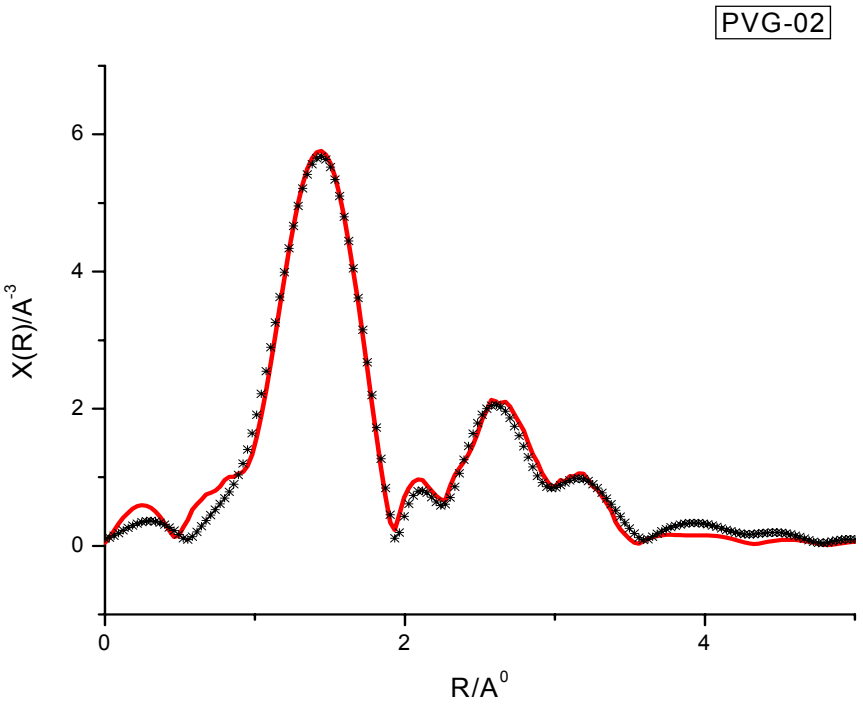

Fig.-13 b

Figure 49. k^3 weighted EXAFs data and theatrical fit of PVG-02. The line represents the theoretical fit of the data points (∗).

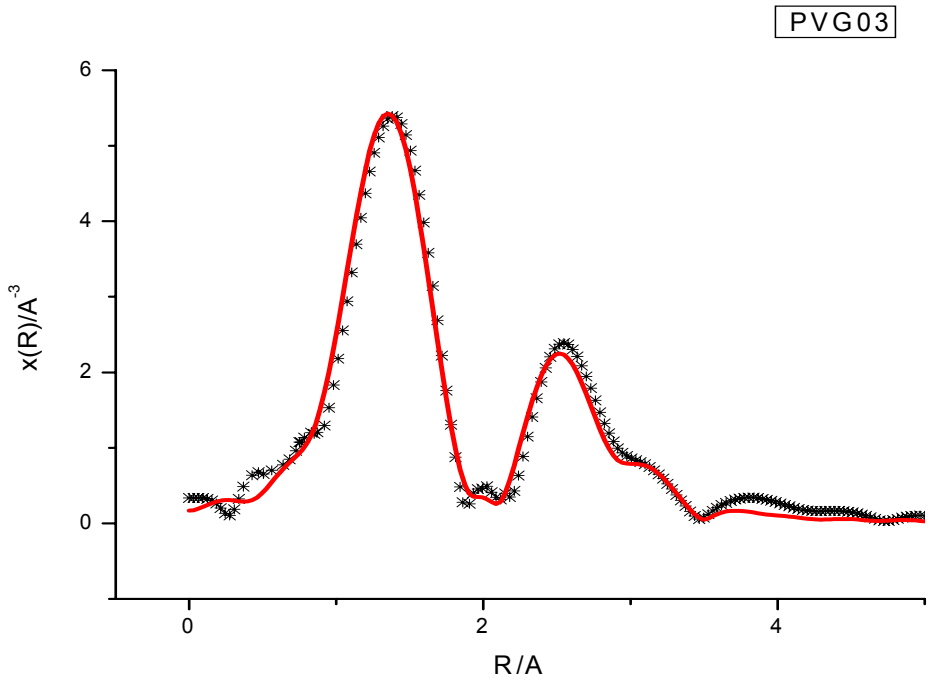

Fig.-14 a

Figure 50. k^3 weighted EXAFs data and theatrical fit of PVG-03. The line represents the theoretical fit of the data points (∗).

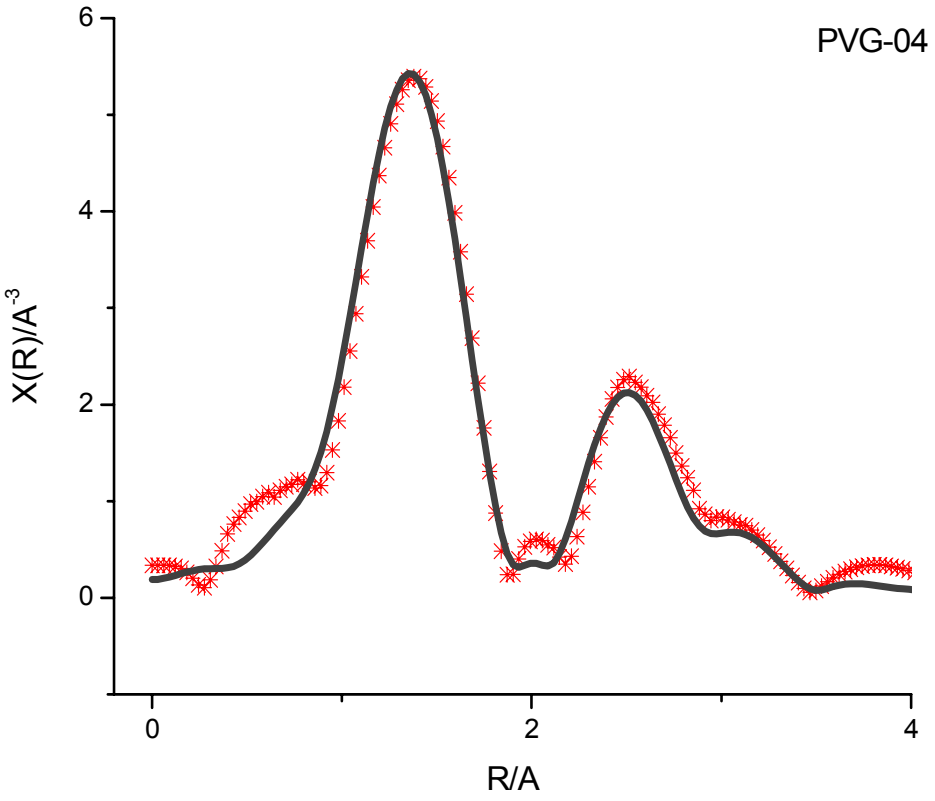

Figure 51. k^3 weighted EXAFs data and theatrical fit of PVG-04. The line represents the theoretical fit of the data points (∗).

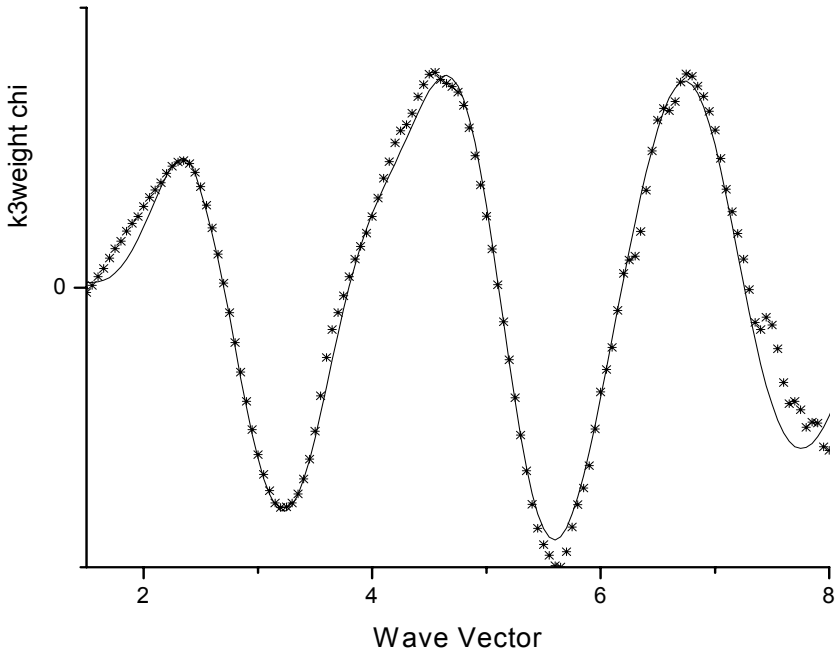

Figure 52. k^3 weighted $\chi(k)$ EXAFs data and theatrical fit of T-02. The line represents the theoretical fit of the data points (∗).

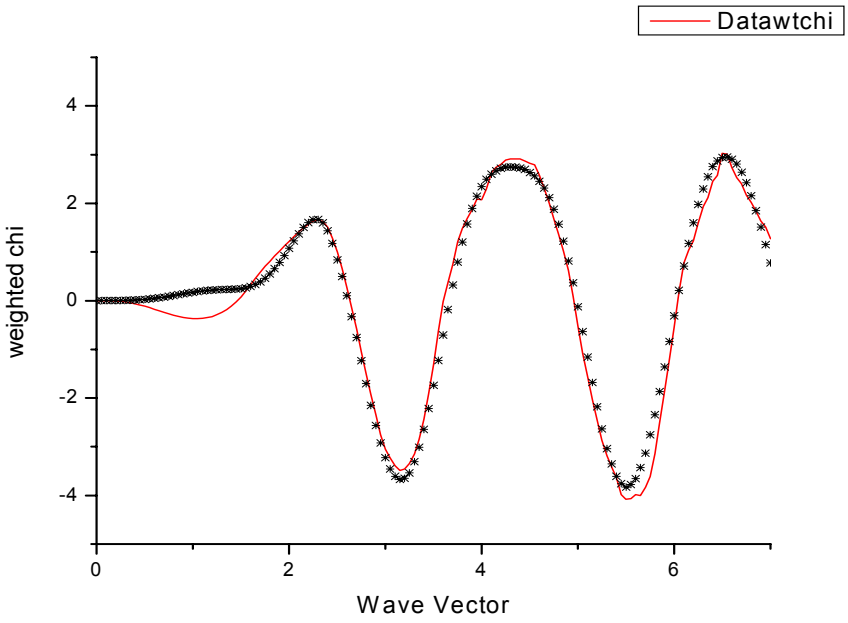

Figure 53. k^3 weighted $\chi(k)$ EXAFs data and theatrical fit of T-01. The line represents the theoretical fit of the data points (∗).

3.1.4 EPR Spectroscopy

The *g* values of EPR were calculated based on the equation,

$$g_e = \frac{h\nu}{\mu_B B_0} \quad (7)$$

The signal corresponding to *g=4.3* are assigned to Fe^{3+} in strong rhombic distorted tetrahedral coordination. The signal at *g=2.18* had been attributed to non frame work iron oxide/oxi-hydroxide nano-particles in silica channels. The signal at *g=2* is normally assigned to octahedral iron.

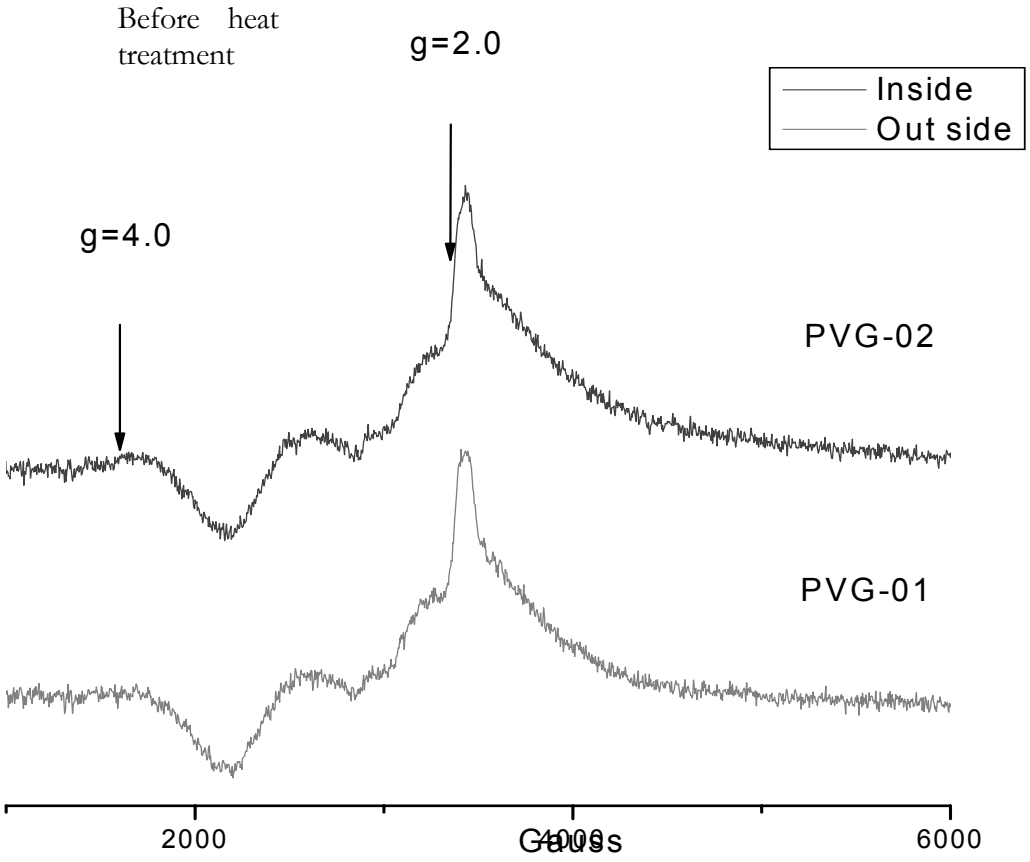

Figure 54. EPR spectrum of PVG-01 and PVG-02 at room temperature.

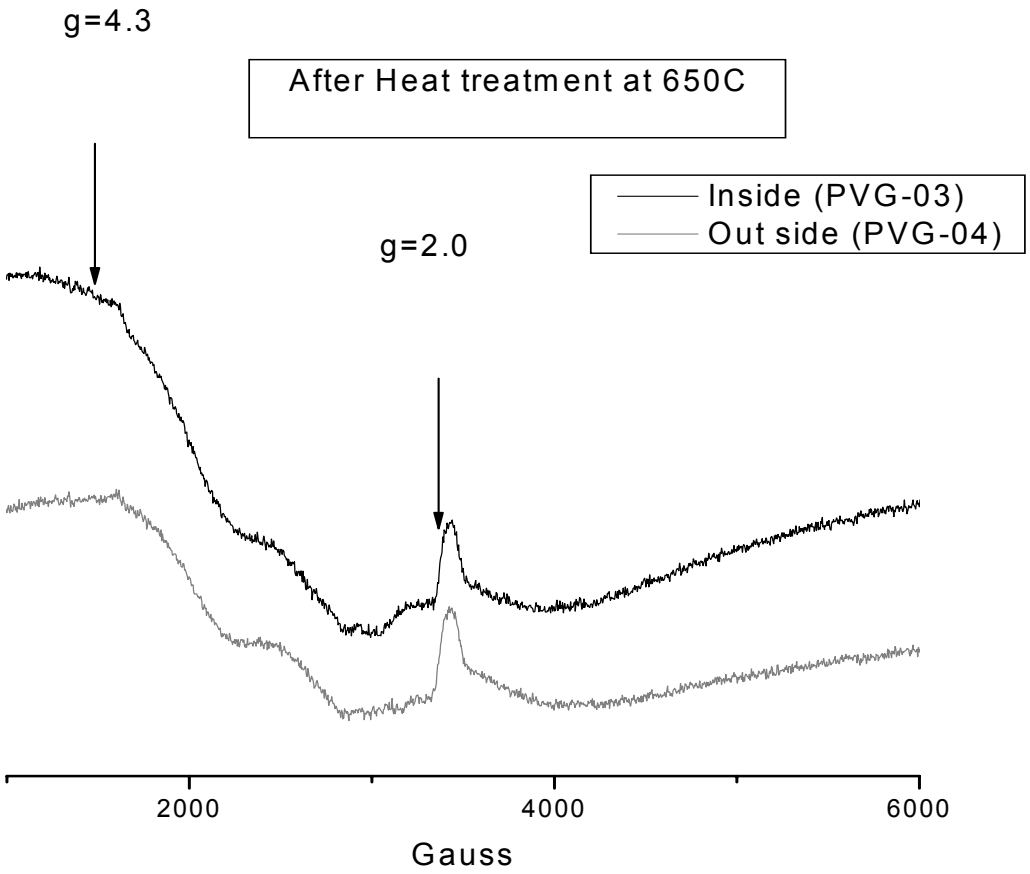

Figure 55. EPR spectrum of PVG-03 and PVG-04 at room temperature.

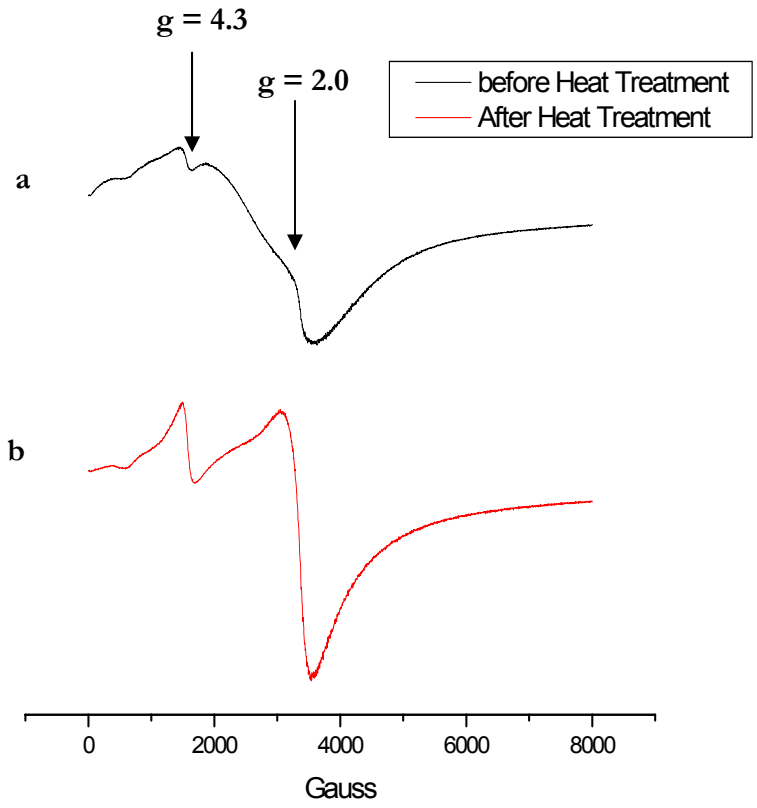

Figure 56. EPR spectrum of T-01 and T-02 a) prior to heat treatment b) after heat treatment.

3.1.5 Mossbauer Spectroscopy

a) Primary characteristics of Mössbauer spectrum

Though total absorption intensity of the spectrum is a function of the concentration of Mossbauer nuclei, generally this is not an appropriate technique for measuring the absolute concentration of a nuclide. The absorption intensity depends on number of other factors which are difficult to quantify. The technique is very effective in determining relative concentrations of different oxidation states [83].

The energy separation of ground and excited levels, between source and absorber is given by the isomer shift δ [84]. This is sometimes known as the chemical shift or center shift (**Figure 12**). The isomer shift is not an absolute quantity [83]. Therefore isomer shift data are expressed relative to standard absorber, which in all of our experiments α-Fe (0) was the standard.

When the nuclear angular momentum quantum number I >1/2 the nuclei have non-spherical charge distributions which are characterized by nuclear quadrupole moment, Δ. In the case of ^{57}Fe the excited state has I =3/2 (or $|3/2\rangle_e$). In the presence of electric field gradient, this line splits into two subsets, with m_I = |1/2| and m_I = |3/2| [83]. The quadrupole splitting is obtained from the separation of two lines. The quadrupole splitting reflects the symmetry of the bonding environment and the local structure in the vicinity of Mossbauer atom [83].

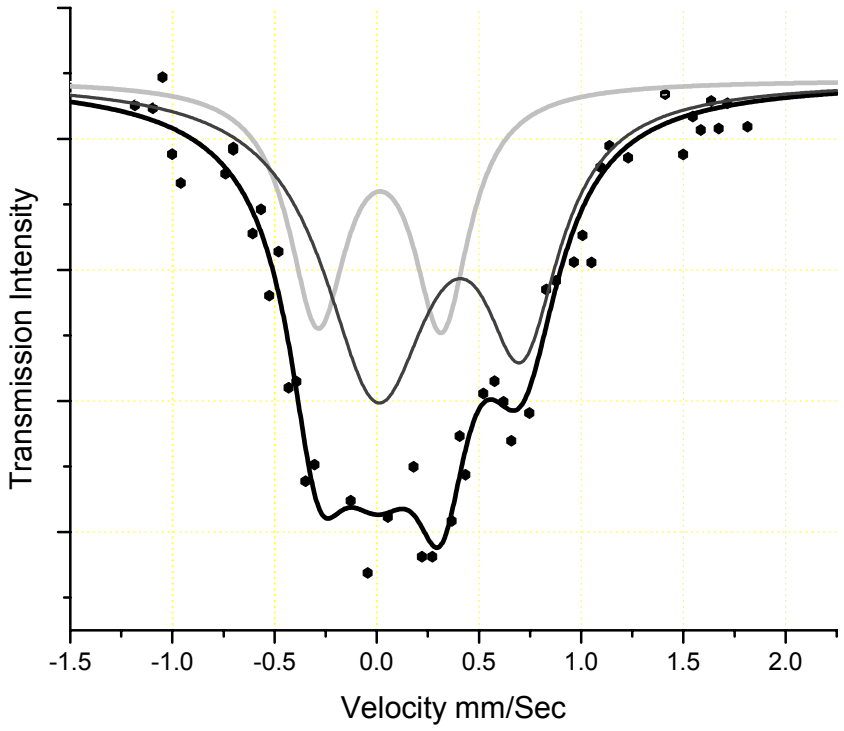

Figure 57. Mossbauer spectra of iron impregnated PVG after heat treatment. Data from Reference [111] was reanalyzed.

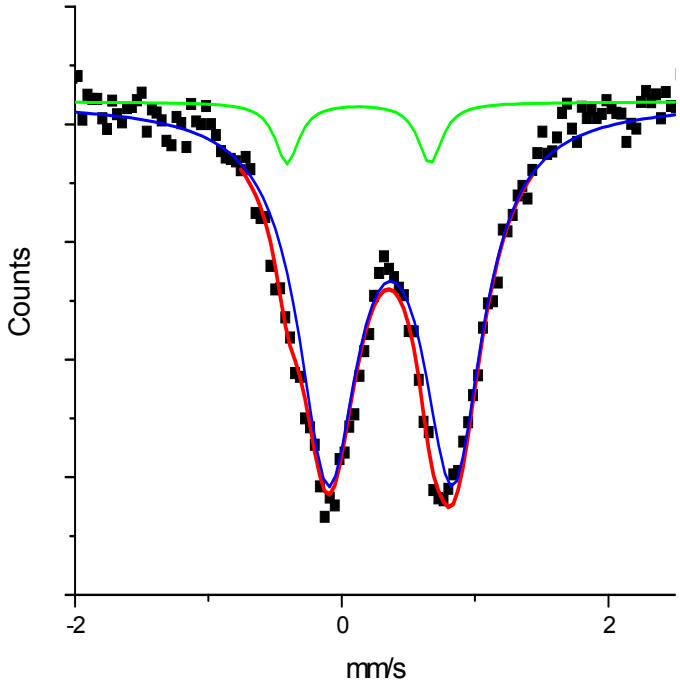

Figure 58. Mossbauer spectra of T-01. a)doublet with Isomer shift, 0.136 mm/sec, and quadrupole splitting 1.0909mm/sec. b)doublet with Isomer shift, 0.364 mm/sec, and quadrupole splitting 0.909mm/sec.

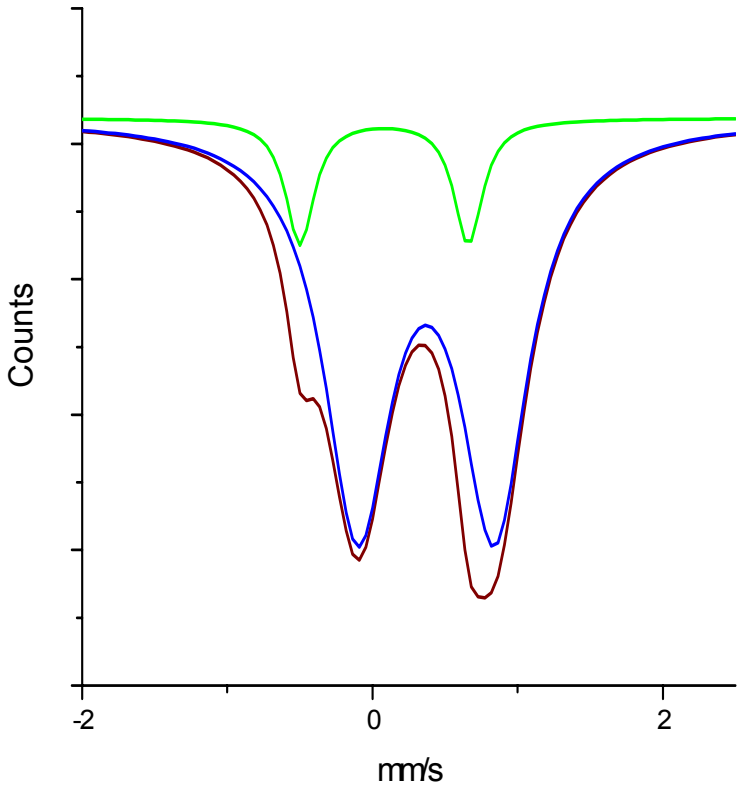

Figure 59. Mossbauer spectra of T-02. . a)doublet with Isomer shift, 0.136 mm/sec, and quadrupole splitting 1.0909mm/sec. b)doublet with Isomer shift, 0.364 mm/sec, and quadrupole splitting 0.909mm/sec.

3.1.6 Low angle XRD

The low angle XRD of the MCM showed 2-D hexagonally packed mesostructure. Low angle diffractogram exhibits four Bragg peaks, which can be indexed as (100),(110),(200) and (210). The distance between pore centers can be estimated using $2d_{100}/\sqrt{3}$ where d_{100}= 4.35nm (**Figure 60**).As shown in **Figure 60** the distance between pore centers were evaluated using **Equation 11**. Where d_{100} is the inter planer distance between 100 planes.

$$2a\cos\left(\frac{\Pi}{6}\right) = d_{100} \qquad \textbf{(11)}$$

$$2a = \frac{2d_{100}}{\cos\left(\Pi/6\right)} \qquad \textbf{(12)}$$

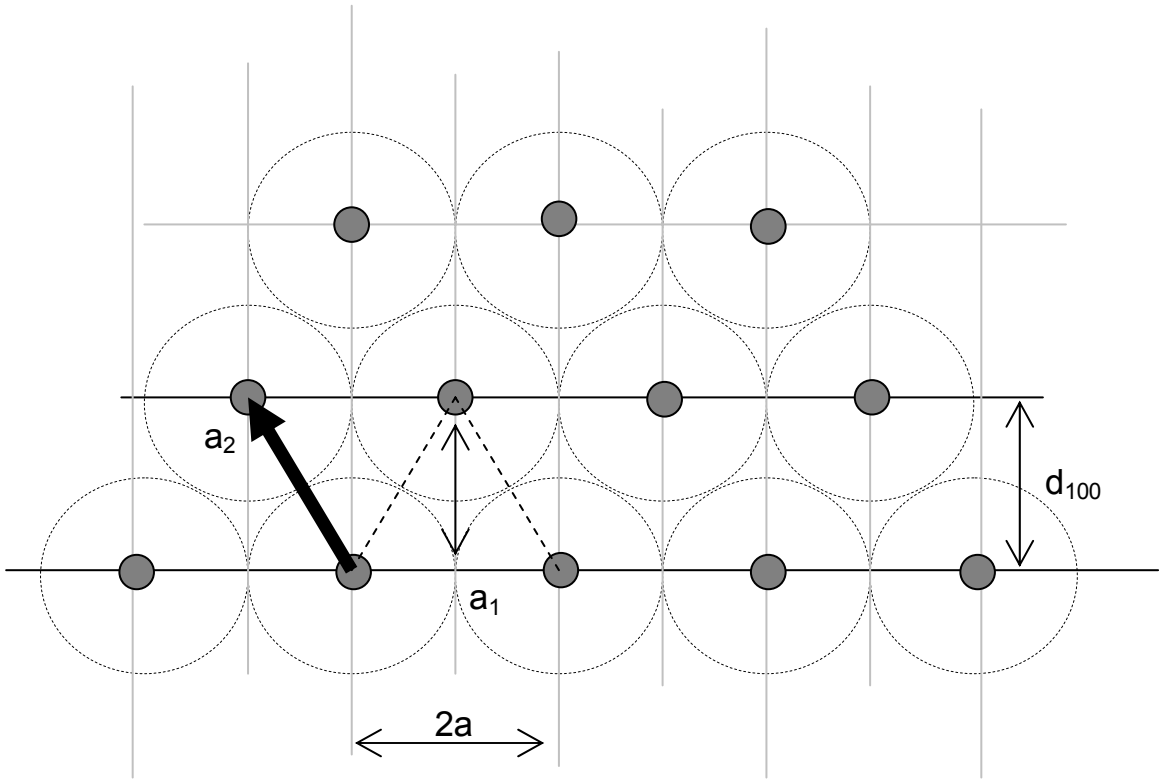

Figure 60. 2-D hexagonal Bravais lattice

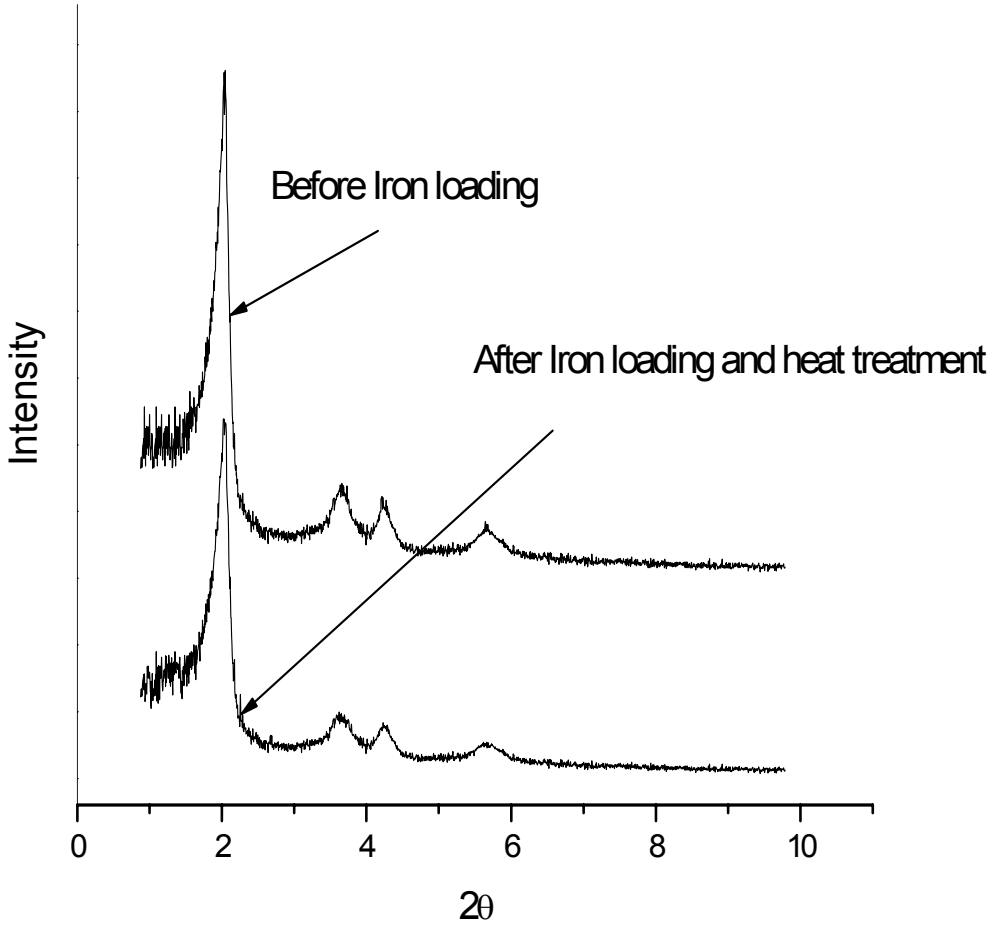

Figure 61. 2-D hexagonal structure of MCM-41and Fe-MCM-41 heated to 650 ^{0}C.

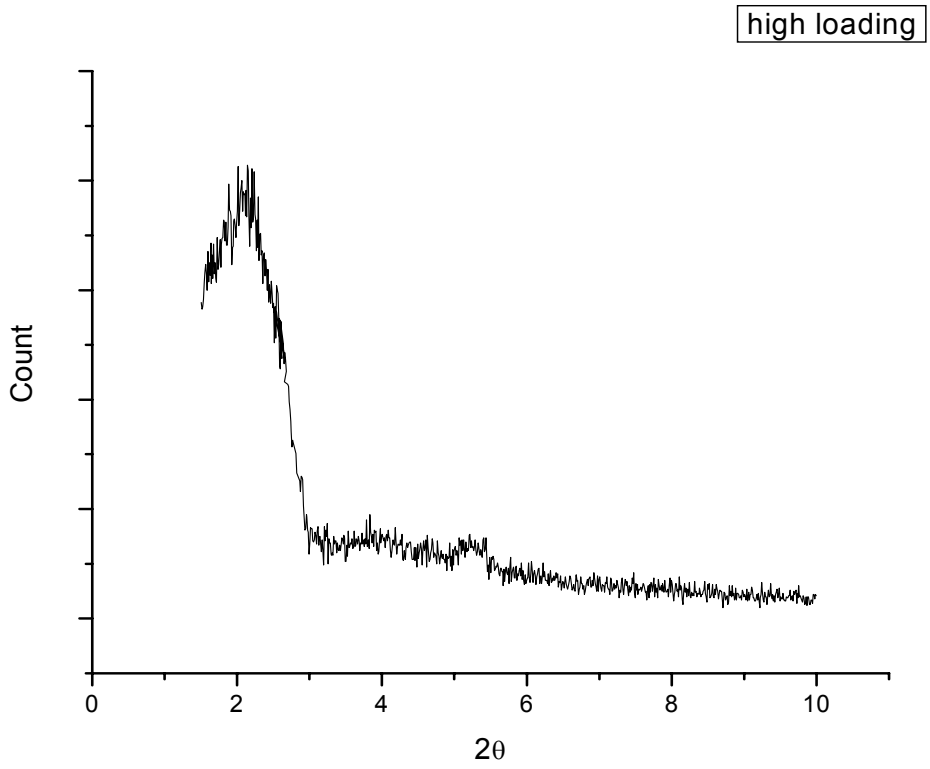

Figure 62. Low angle XRD of Highly (approximately 8 times higher than low iron loaded samples) Fe loaded MCM-41

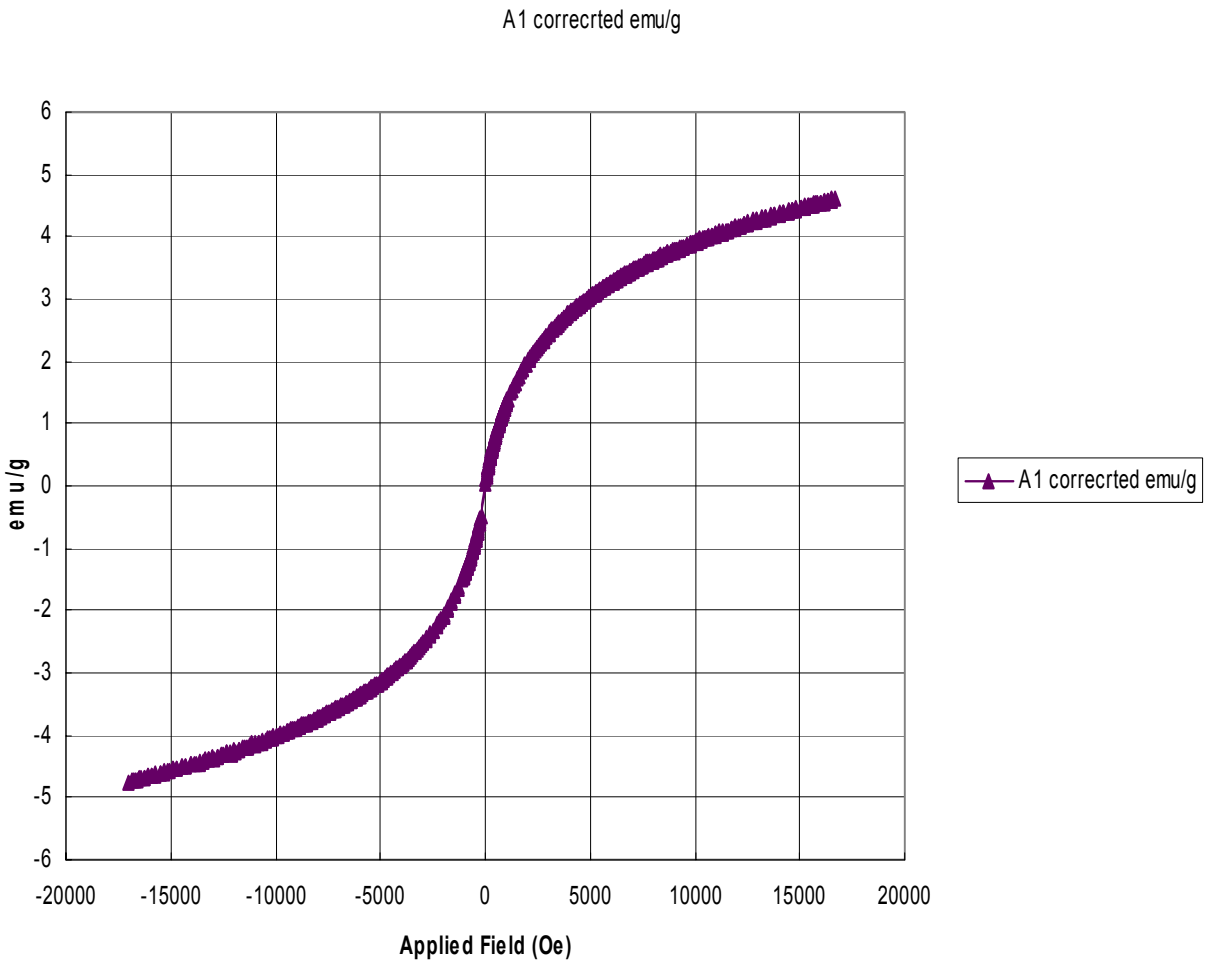

Figure 63. Fe-MCM-41 Magnetization curve at room temperature.

Chapter 4

4. 0. DISCUSSION

4. 1. Iron Impregnated PVG

4.1.1 UV-Visible Absorption

The porous Vycor glass (PVG) has little absorption below 310 nm. The absorption edge of iron oxide particles embedded in PVG significantly shifts towards higher energy relative to bulk α-Fe_2O_3. The bulk α-Fe_2O_3 has a band gap around 2.2eV [71]. The band gap change due to quantum confinement of iron oxide particles were reported by several authors. Miyoshi reported band gap increase of 0.28eV relative to bulk hematite [62].About 2eV band gap increase in iron oxide due to quantum size effects has been reported by Iwamoto [80]. Cohen has reported a 2.9eV band gap of γ- Fe_2O_3 particles embedded in transparent block copolymer films [63]. A relatively larger absorption edge shift of our iron doped in PVG samples was observed before heat treatment. Each of the above authors has shown that the band gap of iron oxide reduces with particle growth. At least quantitatively, the edge shift may be due to particle growth in silica matrix.

4.1.2 Iron distribution and image formation

Analogous to integrated electronic circuits, devices that integrate multiple photonic functions are called photonic integrated circuits, PICs. The major difference between the two is that a PIC provides functionality for information signals imposed on optical wave lengths. Unlike electronics in which the primary device is the transistor, there is no single dominant device in PIC. The range of devices required for an optical chip includes low loss interconnects waveguides, power splitters, optical amplifiers, optical modulators, filters, lasers and detectors. Photonic integrated circuits can allow optical systems to be made more compactly, having higher performance

than with discrete optical components. They also offer the possibility of integration with electronic circuits to provide increased functionality.

It has been discussed in our previous publications the potential of using iron doped PVG in integrated optics. The ability to photopattern iron in PVG and consolidate the glass without significant loss of pattern resolution, makes these ideal candidates. There is still discussion as to the exact mechanisms regarding image formation in the glass and the factors that affect image quality such as contrast, resolution, and noise. Micro X-ray fluorescence (μ-XRF) was used to study the images formed on $Fe(CO)_5$ doped PVG.

The X-ray fluorescence intensity of Fe K_α (**Figure 64**) was used to study contrast and sharpness of images formed on $Fe(CO)_5$ doped PVG.

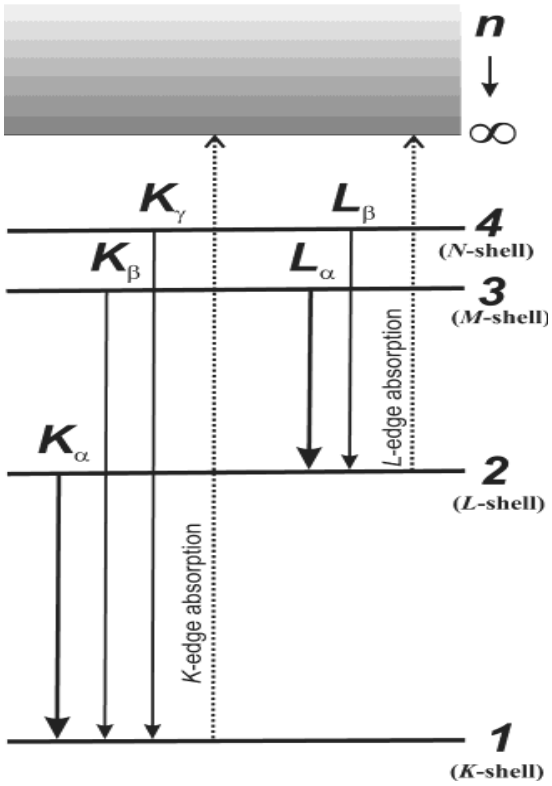

Figure 64. Core transitions and XRF lines.

An area of about 1mm X 1mm was selected as shown in **Figure 65**. The scan was run as described in the experimental section. The X-ray fluorescence intensity of Fe K_α (**Figure 64**) was plotted against the X and Y positions (**Figure 22** and **Figure 25**). These three dimensional plots compared the Fe K_α XRF intensity as the probe moved from photolyzed to unphotolyzed regions. The area not exposed to the xenon lamp has a lower concentration of iron compared to the exposed area (**Figure 24**). In order to analyze iron distribution at the border, intensities at different X positions were averaged. The average X intensity at a given Y value is designated as the normalized average intensity.

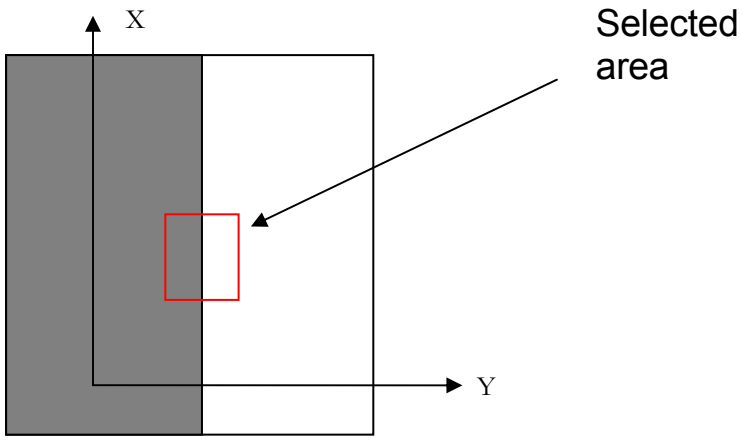

Figure 65 *Area selected for XRF*

The slope of the normalized average intensity of Fe K_α in the highlighted area relates to the contrast of the image (**Figure 22** and **Figure 26**). The data show that the approximately six times more iron in the photolyzed regions then in unphotolyzed.

The steeper the slope the bigger discrepancies in iron distribution, and hence a sharper contrast. Lower slopes correspond to softer contrast. In order to analyze the contrast variation at the border region the first derivative of the normalized Fe K_α X-ray fluorescence intensity averaged over 1mm in the X direction was taken. The variation of the normalized average intensity with the distance in the Y direction was fit to the Cauchy-Lorentz function-

$$y = y_0 + \frac{2A}{\Pi}\frac{w}{4(x - x_c)^2 + w^2} \quad . \qquad \textbf{(13)}$$

The FWHM of the fit can be use as a parameter to analyze iron distribution at the border. If the iron distribution at the border is gradual this should reflected by higher FWHM values and if it has a sudden jump, then FWHM should be smaller.

The FWHM of the sample before heat treatment is 0.059±0.0053 (**Figure 23**) and even after 4hrs of heat treatment at 650^0C, FWHM value (0.062±0.0072) changes only marginally, about 3% , (**Figure 27**). This confirms that there is no lateral diffusion of iron >10 μm on the XY plane. Our previous studies showed that there was particle growth at 650^0C. These observations suggest that if the particle growth is due to diffusive mass transport, then the upper limit of effective diffusion length is less than 10μm at 650^0C.

4.1.3 XANES

When the energy of an incident photon is sufficient to over come the binding energy of a core electron, absorption of the photon excites it to unoccupied higher energy levels [64]. In K-edge spectroscopy, a 1s electron is excited. The strongest peak of the first row transition elements is attributed to a 1s-4p transition. X-ray Absorption Near Edge Structure (XANES) generally can be considered to extend up to 50eV above the edge of the absorbing element [66].

XANES spectroscopy is a technique that is sensitive to the valance and the site geometry of an absorbing element [66]. The shape of the edge and the pre-edge resonances are characteristic of the local symmetry of the absorbing atom sites and can be used as fingerprints in the identification of its local structure [66]. A pre–edge feature, well separated from the main edge on the low energy side of the absorption edge of first-row transition elements is due to 1s →3d core transitions [65]. These transition intensities have been widely used to investigate variations of the chemical and structural information of metals in glasses, and this has become a widely accepted, relatively simple technique for determining coordination of transition metal ions in oxide glasses [66].

Before extracting pre edge from the experimental data 3-runs per sample were aligning by aliening selected peaks of first derivative of energy

scans. To extract the X-ray absorption pre edge from the background, the spectral region before the pre edge was fit to a polynomial and subtracted from the data as a background. The pre-edge was then extracted by subtracting two Lorentzian functions fitting the tail of the edge jump (**Figure 31** through **Figure 35**). In low resolution scans the pre-edge may appear as a one broad peak, but with the high resolution scans partially overlapping peaks can be extracted from pre edge (**Figure 31** through **Figure 35**).

Spectra were normalized to the average atomic absorption of 7350eV to 7500eV. By 7350eV, the near-edge oscillations are attenuated and absorption intensity now becomes independent of the oxidation state and coordination of the iron. After subtracting the pre-edge contributions, the absolute fluorescence intensity of this region is proportional to total iron concentration [67].Therefore, normalization allows us to compare spectra of samples with different iron concentrations.

a) Pre-edge

In centrosymmetric crystal fields, the 1s →3d transitions are electric dipole forbidden, but still can be observed as a weaker feature due to, quadrupole coupling effects [68], and the hybridization of Fe 3d and ligand 4p orbitals [73]. In noncentrosymmetric environments, the transition is dipole allowed and as a result intensities are at a least few times higher than the transitions in centrosymmetric environments [68]. The area under the pre-edge is sensitive to the crystal field around the absorbing atom [68], and increase with the non-centrosymmetric geometry of the crystal field [68].

The number of transitions in a given ligand field can be predicted by d^{n+1} crystal field model, where n is the number of *d*-electrons in the absorber [69]. The electron involved in the transition is added to the number of *d* electrons, e.g., d^{6+1} configuration for Fe^{2+}. In general terms, four transitions are accepted for tetrahedral Fe^{2+}, three for octahedral Fe^{2+} two for octahedral Fe^{3+} and two for tetrahedral Fe^{3+} [69] but usually only two transitions are

needed to model tetrahedral Fe^{2+} and Fe^{3+} [72, 69]. Provided the instrumental resolution is high enough, the two electronic transitions expected from Fe^{3+} in octahedral environment (**Figure 66**) can be resolved. In tetrahedral symmetry, if the resolution is not high enough due to the low crystal filed splitting ($\Delta_t = 4/9\ \Delta_o$) only one line may appear (**Figure 66**).

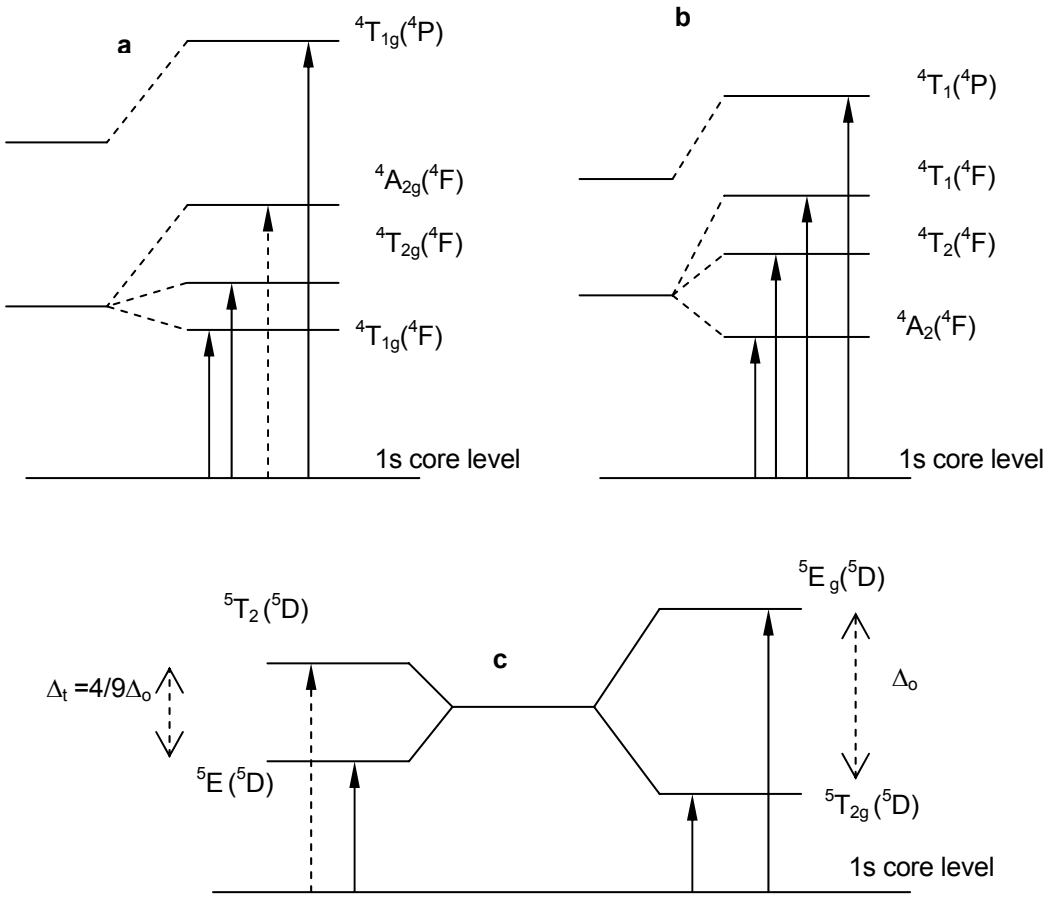

Figure 66. Electronic transitions of pre edge spectrum of iron (a) Fe^{2+} in an octahedral (b) Fe^{2+} in an tetrahedral (c) Fe^{3+} in an octahedral (right) and tetrahedral (left)

The normalized pre edge spectra of hematite can be deconvoluted as shown in the **Figure 36** and **Figure 37**. According to Wilke et al.[72], the feature that consist of peaks above 7116eV cannot be related to 1s→3d/4d transitions since the origin of these are still not known [72,70], contributions from these transitions were excluded from the calculation of the pre edge parameters [72]. It is important to not that as reported by Giuli [70] Wilke et al. calibrated edge energies of Fe metal at 7112.92eV.Therefore, their values have been rescaled accordingly in order to compared with our values. The remaining components converge to 50:50 Voigt shapes instead of quasi-Gaussian shapes (**Figure 36** and **Figure 37**). The two components can be fit with centroides near 7113.8eV and 7115.3eV, and this is in agreement with the Wilke's analysis of Fe(III) bearing minerals [72].

The pre edge centroid position of Fe(II) is lower in energy than that of Fe(III).According to Prietzel, the centroid position of Fe(II) minerals such as Pyrite, Pyrrhotite, and Marcasite are 7112.8±0.6 eV [71], and the pre-edge centroid position of Fe(III) bearing minerals such as Ferrihydrite, Goethite, Lepidocrocite ,Hematite and Jarosite fall within the range of 7115.0±0.4 eV [71]. Wilke has studied a large number of Fe(III) and Fe(II) model compounds and their pre edge characteristics [72]. According to these studies, the pre-edge centroid of Fe(II) model compounds fall within the range of 0.89-1.45 eV [72] and Fe(III) model compounds are within 2.43-2.61 eV [72] above the Fe-K edge energy (7112eV).

The centroid of the extracted pre-edges of the PVG-01 and PVG 02 are 2.69 eV higher in energy than the Fe K-edge while the centroid of the PVG-03 and PVG-04 are 2.72 eV higher in energy relative to the Fe K-edge. A comparison of pre-edge centroid of the samples and the above mentioned model compounds and minerals is shown in **Figure 67**. The pre edge centroides of PVG (**Figure 67**) provides no evidence of Fe(II).

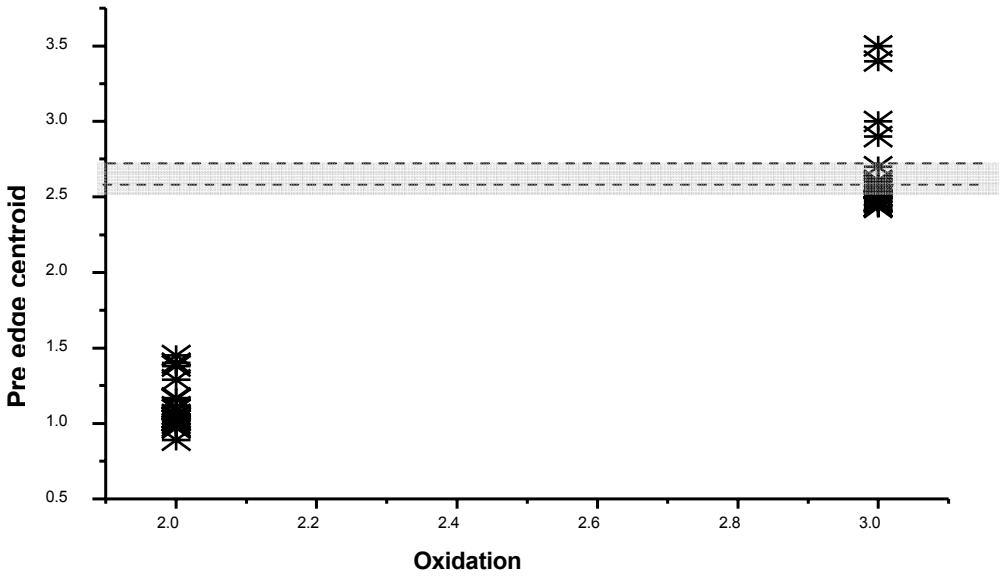

-

Figure 67. Pre edge centroid variation with oxidation state. The symbol * represent pre-edge centroid position of model compounds. The pre edge centroid position of these model compounds is taken from reference [72] and [71]. The pre edge positions of PVG samples are in between the dotted lines

.

Relative to centrosymmetric model compounds the areas of the extracted components of the normalized pre edges of the samples are, for PVG-01, 74.97% , for PVG-02, 56.8% , for PVG-03, 76.25% and PVG-04, 73.74% (**Figure 44**).

Since the intensities are normalized to total Fe concentration, the difference in normalized pre-edge areas between samples and centrosymmetric model compound (α-Fe_2O_3) indicates higher total Fe concentrations than that of total Fe(III) concentration in the samples (total Fe >total Fe3+, **Figure 44**). As iron can exist in three stable oxidation states , Fe(0) ,Fe(II) and Fe(III) ; this imply that samples contains Fe(0) or Fe(II) in addition to Fe(III). Since the edge and pre edge analysis ruled out Fe(II) , we conclude that samples contain Fe(0) and Fe(III). This is consistent with the Mossbauer data, which also confirmed non existence of tetrahedral iron sites and the EXAFS analysis present here in chapter 4.1.4, as well as our previous studies on photo-deposited iron in PVG [73]. Even though zero valent iron is a product of thermal and photo decomposition of $Fe(CO)_5$ it is not common to find unoxidized iron in silica matrices [74].

The fact that there is a significant area difference between PVG-01(76.25%) and PVG-02(56.8%) implies more unoxidized iron trapped inside the glass matrix compared to the surface (**Figure 44 a**). After heat treatments at 650^0C these areas became comparable (PVG-03 76.25% and PVG-04-73.74%) indicating that both inside and the surface now have roughly the same Fe(III)/Fe(0) ratios. Even after heat treatment, the normalized pre-edge areas are notably smaller compared to the centrosymmetric model compound. This is an indication that the heat treatment does not oxidize all the iron present on the surface of the glass and in side the matrix. The relative area increase after heat treatment, of surface (PVG 01 to PVG 03, **Figure 45 -b**) is insignificant, a 1.28% increase compared to interior (PVG-02 to PVG-04,

Figure 45-a). This suggest that heat treatment dose not alter the Fe(III)/Fe(0) ratio of surface iron by significant amount.

The relative area increase of samples with removed surface (PVG 02 to PVG 04,) is comparatively large (20%), implying that heat treatment considerably increased the Fe (III)/ Fe(0) ratio in the interior of the glass.

The EXAFS study done on the iron impregnated PVG shows that the bond lengths and coordination geometry of the iron compounds formed immediately after photolysis does not change with the annealing; suggesting that heat treatment does not produce new chemical species of iron. These observations lead us to conclusions that iron on the surface forms a thick protective layer of oxides immediately after the photolysis and the interior of the glass still carries iron particles with no protective oxide envelope or thin oxide covering, which is not sufficient to prevent further oxidation of particles. The particles formed in the interior of the glass oxidized until the oxide envelope is thick enough to prevent further oxidation (**Figure 44-b**). The data suggest that there is a critical ratio of Fe(III)/Fe(0) that stabilize these particles and prevent further oxidation. This state is reached when the Fe(III) mole fraction reaches approximately 75% of the total iron content (**Figure 45-b**).

b) Edge position

Though XANES does not provide a direct measure of the ionization energy [66] threshold (**Figure 38**), recent studies show that the energy shift of the first bound excited state at the absorption threshold or white line energy follows the binding energy shift of the core levels [66]. Therefore, this can be used to probe oxidation states of the absorbing atom [75]. Prietzel reported the white line energy (WL) of, Fe(III) bearing minerals such as Ferrihydrite, Goethite, Lepidocrocite ,Hematite and Jarosite are 20.45±0.95 eV higher in energy compared to Fe-K edge and Fe(II) minerals such as Pyrite, Pyrrhotite, and Marcasite are only 9.45±0.55eV [71] from the Fe K-edge. The PVG -01

and PVG 02 samples show a 21.06 eV energy shift where as PVG-03 and PVG-04 samples show a 21.39eV shift relative to Fe K- edge.

c) XANES Shape resonance analysis

Multiple scattering of excited photoelectron from neighboring atoms creates strong absorption features, 30-60 eVs above the photo ionization energy in the continuum part of the spectra of condensed materials [76].

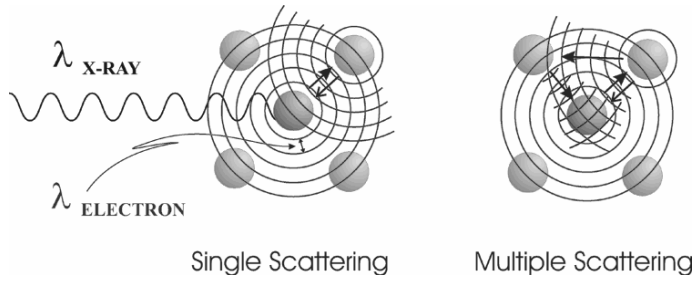

Figure 68. Multiple scattering of photoelectron

These multiple scatterings make it harder to fully interpret XANES spectrum but still empirical interpretations of XANES are easier compared to EXAFS and provide some valuable information about micro environment and the charge state of the absorbing atom.

Above the first strong resonance there are so called shape resonances [79] (**Figure 38**). This in some cases provides useful information about bond lengths [77].According to **Equation 14** energy separation between the WL (white line) and the first XANES peak after the main edge can be used to evaluate average bond Fe-O lengths [78,79].This is a straight forward approach but only allow us to evaluate bond length ratios.

$$\sqrt{\frac{(E_{r1} - E_{WL})}{(E_{r2} - E_{WL})}} = \frac{R_2}{R_1} \qquad \textbf{(14)}$$

This method yields reasonably accurate average bond lengths, provided the medium-range environment does not interfere significantly. Wilke and co workers have recently used the same method to evaluate average Fe-O bond lengths in silicate glasses [75]. We estimate the average ratio of bond lengths of Fe-O in the four PVG samples and the results are summarized in **Table 4** .

Table 4. Average Fe-O bond length variation from surface to interior.

Sample	**surface**	**E_r-E_{WL}**	**Ave Fe-O bond length ratio**
PVG-01	Top 30μm surface	7191.5-7133	(PVG-01)/(PVG-02) = **1.00042**
PVG-02	Top 30μm surface Removed	7191-7133	
PVG-03	Top 30μm surface	7192-7133.3	(PVG-03)/(PVG-04) = **1.0086**
PVG-04	Top 30μm surface Removed	7191-7133	

The yield average bond length differences are; about 0.2% for PVG-01 and PVG -02 and about 0.3% for PVG-03 and PVG-04. The comparison of PVG-01 with PVG-03 and PVG-01with PVG-04 shows that average bond length variation is less than 1%. These data suggest that chemical nature of the iron compounds on the surface and interior of the glass are identical and annealing does not affect the chemical nature of these iron compounds.

4.1.4 EXAFS

The absorption edge corresponds to an X-ray photon having just enough energy to free a bound electron in the atom [66]. When excited electrons are from the n=1 shell, the edge is called K-edge and when the electrons are from the n=2 shell edge is called L edge. The X-ray absorption of up to 40KeV is dominated by photoelectron absorption [66]. The absorbed photons excite a photoelectron creating a core hole in the atom and the atom may have more than one excitation. The kinetic energy of excited photo electron is given by the difference between the energy of the photon and the binding energy. This difference is normally large compared to the interaction energy with surrounding atoms [66]. The final state photo electron is modified by scattering of each surrounding atom (**Figure 69**). The result is the superposition of outgoing and scattered waves.

The phase variation with the wavelength of photoelectron depends on the distance between the central atom and the backscattering atoms [66] and the backscattering strength depends on the type of backscattering atom [66].

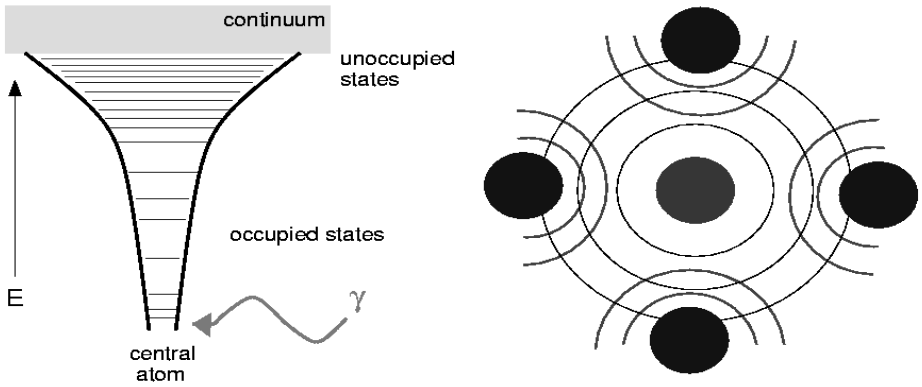

Figure 69. Photoelectron propagation

An FEFF calculation shows that the main contributors to the EXAFS spectrum of the first shell are single-scattering paths (ssp) with Fe in the center and oxygen or iron in the nearest neighbors(NN) (Fe→Oand Fe→Fe). The second shell contributions are from Fe-Fe single-scattering paths and multiple scattering paths such as Fe→O→O→Fe and Fe→Fe→Fe→Fe.

Figure 48 and **Figure 49** show the pseudo radial distribution functions(RDF) of iron in PVG-01 and PVG-02 respectively and **Figure 50** and **Figure 51** show the pseudo RDF of PVG-03 and PVG-04.

The bond length values of Fe-O and Fe-Fe of PVG-01 and PVG-02 (1^{st} and the 2^{nd} shells) are effectively equal (**Table 5**) and the bond lengths of PVG-03 and PVG-04 are also similar. This confirms our assumption that chemical nature of iron compounds does not change with the depth. This conclusion is consistent with the XANES shape resonance results present in section **4.1.3**. In our previous studies [73], we confirmed that heat treatment has no impact on the chemical nature of the iron based products formed in PVG matrices. The Fe-O distance in the first coordination shell is 1.96±0.06Å. similar distances observed in the iron oxides are α-Fe2O3-1.99 Å, γ -Fe2O3-1.86 Å , α-FeOOH- 1.97 Å, β- FeOOH- 1.89 Å, γ- FeOOH-1.89 Å, and δ-FeOOH-2.00 Å [80]. The NN distance between Fe and O indicates α-Fe2O3 type structure. This is consistent with the Mossbauer analysis.

The above data (**Table 5**) confirms that the bond length of the iron compounds on the surface and interior of the glass are similar before and after heat treatment. The first coordination shell consist of two major scattering paths ,Fe-O 1.96A and Fe-Fe-2.651A. The distance 2.65A is closer to the distance of α-Fe metal (Fe-Fe=2.4823A)[80]. The deviation could be due to the amorphous nature of iron particles formed.

Table 5. EXAFS results of PVG samples.

Sample	1st Shell R/A^0	2nd Shell R/A^0
PVG-01	1.95	2.99
PVG-02	1.96	2.98
PVG-03	1.90	2.99
PVG04	1.98	3.01
Ave	1.96	2.99

4.1.5 Electron Paramagnetic Resonance

The EPR data of the samples taken at room temperature are presented in **Figure 53** and **Figure 54**. Though EPR is highly sensitive tool to probe local environment of paramagnetic iron [81] the interpretation of the EPR data in silica matrices is still controversial [107]. The presence of silanol groups and water molecules interferes with the EPR signal making it more complicated [107]. But we still can gain some important information from these spectra. Surface and interior, have similar spectral variations before and after heat treatment (**Figure 54**, **Figure 55**) indicating that there is no difference in chemical nature of paramagnetic iron, inside and on the surface of the glass before and after heat treatment.

The EPR signal at g=2.0 is generally associated with oxide clusters and g=2.0 is normally attributed to octahedral iron sites [82] whereas g=4.3 is attributed to tetrahedral sites with rhombic distortion [82]. Before and after heat treated samples show no tetrahedral iron (g=4.3) and confirmed presence of octahedral Fe (III) (g=2.0).

The EXAFS, the XANES and the EPR data converge at the conclusion that surface and interior of PVG has the same chemical species but at different compositions. Both the interior and the surface have metallic iron and Fe(III) oxide, but the Fe(0)/Fe(III) increases from the surface to the interior.

4.1.6 Mossbauer Spectroscopy

a) Hyperfine parameters

The isomer shift δ is directly proportional to the difference in total electron density at the nucleus of the absorber and source, $\delta = \alpha\left[|\psi_A(0)|^2 - |\psi_S(0)|^2\right]$ where the constant of proportionality *α* depends principally on the relative change in the nuclear radius between the excited state and the ground state, $\delta R/R$ [83]. ^{57}Fe has a relatively large value of *α*, so that oxidation state changes are easily observed. The best fits of Mossbauer spectra recorded of the heat treated samples with out removing surface, deconvoluted to two doublets, indicating two forms of iron present in the glass (**Figure 57**). Vanishingly small isomer shift value, δ=0.095 mm/sec of one doublet suggests that one form could be elemental iron. The other form exhibits an isomer shift and quadrupole splitting (Δ) similar to α-Fe_2O_3, (δ=0.52±0.05 and Δ =0.69 mm/S) indicating octahedrally coordinated Fe(III).

Since Fe(0) in the porous Vycor glass are dense enough to be seen in the Mossbauer spectrum we could rule out of Fe(0) in low density forms like $Fe(CO)_5$ or other volatile iron carbonyls. Hence the Fe(0) is not from the unreacted $Fe(CO)_5$ or other volatile iron carbonyls but must be formed in the photochemical decomposition of $Fe(CO)_5$. This assignment is further justified by the EXAFS results where we found, Fe-O and Fe-Fe in NN positions.

Absorption intensities of two doublets (**Figure 12**) correspond to $|\pm 3/2\rangle_e \rightarrow |\pm 1/2\rangle_g$, $|\pm 1/2\rangle_e \rightarrow |\pm 1/2\rangle_g$ transitions [83] where *e* and *g* refer to the excited and ground nuclear states respectively. The relative transition probabilities and angular intensity dependence of the two quadrupole lines of a doublet (**Figure 12**) are given by $3(1+\cos^2\theta)$**:** $(5-3\cos^2\theta)$, where θ is angle between direction of γ-rays and axis of quantization [84]. Hence the observed area ratio of quadrupole lines of a doublet can be used to obtain information

on the sub lattice. When averaged over all angles the ratio, $3(1+\cos^2\theta)$**:** $(5-3\cos^2\theta)$ approaches 1:1[84]. The area ratio of the two quadrupole lines, of the doublet with $\Delta=0.62\pm0.06$ mm/s. and the $\delta=0.095$mm/sec, is 1.012:1 (**Figure 57**). This indicates that Fe(0) particles are randomly oriented. The two quadrupole lines of the other doublet ($\delta=0.52\pm0.05$ and $\Delta=0.69$ mm/S) are unequal, indicating some preferential orientation of Fe(III) in the glass matrix.

b) Magnetic splitting

When the nucleus experiences a magnetic field, the degeneracy of a nuclear states with an angular momentum quantum number $I>0$, splits in to $2I+1$ sub-states (**Figure70**). The splitting of the spectral lines is directly proportional to the magnetic field strength. The sextet (**Figure70**) is observable when observation time of the experiment, $t_{obs} < \tau$ [85]. The τ is given by Neel-Brown expression $\tau = \tau_0 \exp(KV/kT)$ where k,T, K and V are Boltzmann constant, temperature, anisotropy constant and particle volume respectively[86,87].The pre-exponential factor τ_0 is in the order of 10^{-9}-10^{-12} and depends weakly on temperature [87]. When $t_{obs} > \tau$ the sextet collapses into a quadrupole doublets or to a singlet. This blocking transition depends on the time window of experimental technique used, t_{obs} for Mossbauer spectroscopy $t_{obs} \approx 10^{-8}$ S.

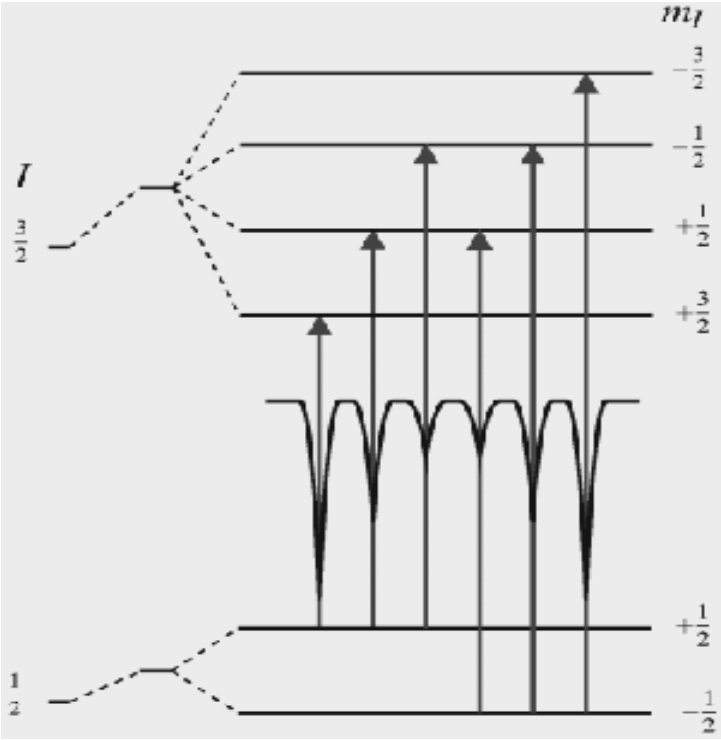

Figure70. The magnetic splitting of the nuclear energy levels of ^{57}Fe

The room temperature Mossbauer spectra of iron impregnated heat treated PVG samples show only quadrupole doublets. This implies that $t_{obs} > \tau$, these arguments were used to estimate lower limit of anisotropy constant of these particles. The value so obtained is 3.8 X 10^5 erg/cm^3, which agrees with our previous measurements [111].

The anisotropy of bulk α-Fe is 1X10^5 erg/cm^3 and the bulk anisotropy of Fe_2O_3 is 1X 10^4 erg/cm^3. Higher anisotropy is typical for small particles, Lou and coworkers [88] have reported two order of magnitude higher than the bulk value for 4.5nm diameter, Fe(0) particles deposited in SiO_2 matrix. If iron particles are rigidly bound we would expect orders of magnitude higher anisotropy.

4.1.8 TEM Micrograph analysis.

The TEM image was taken of wedge shaped edge of iron impregnated PVG piece.

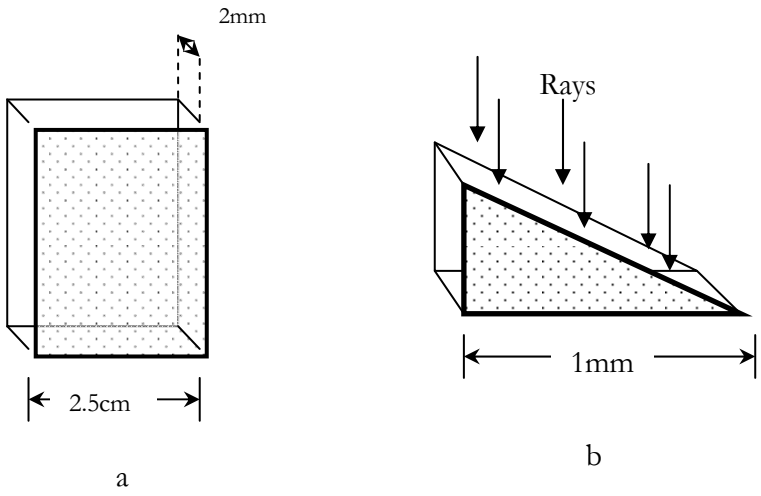

Figure 71. wedge shaped edge of iron impregnated PVG

TEM micrograph was analyzed using Image-J software and found that average circularity of particles in 650C –PVG samples were 0.976 with standard deviation of 0.0419. As circularity of particles is high, in our analysis, the particles were considered as spherical. **Figure 73** shows the histogram of particle sizes obtained from TEM micrographs.

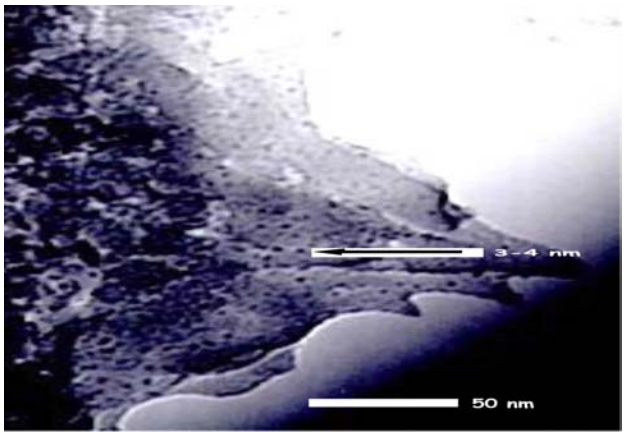

Figure 72. *TEM* micrograph of Fe-PVG heat treated at 650^{0}C [111].

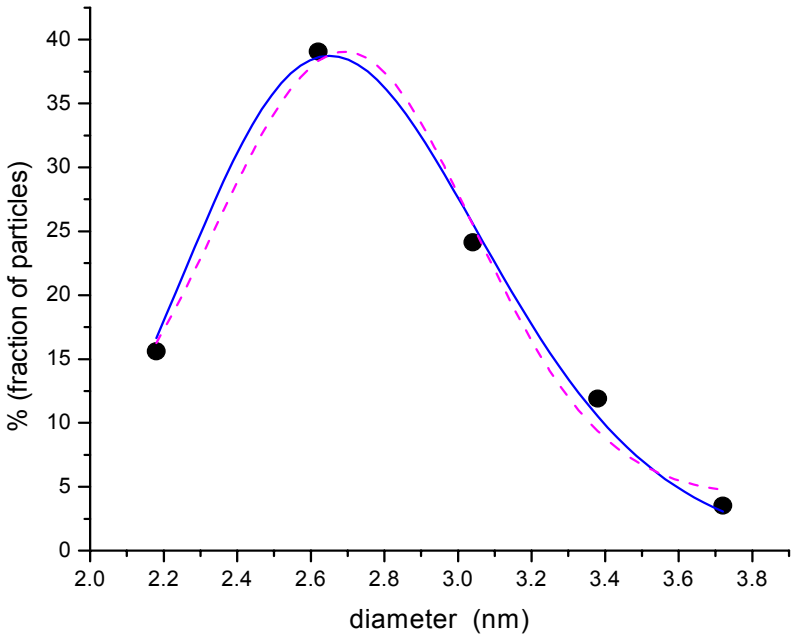

Figure 73 *Particle size distribution*

Log normal and Gaussian curves are fit to particle size data obtained from the TEM micrograph. Log normal distributions have been used for years for particle size studies, and there is ample empirical evidence for its validity for analyzing large populations of small particles. In addition it is more convenient to use than some of the theoretical models available, and it has been shown that log normal distributions closely resembles some of the theoretical models [89].As expected, lognormal distribution gives a better fit compared to Gaussian functions and therefore our experimental data were fit to log normal distribution [90] shown in **equation 15** [91].

$$f(d)d(d) = \frac{\exp\left(\ln(d/d_M)^2 \Big/ 2\sigma_d^2\right)}{\sqrt{2\pi}\, d\, \sigma_d} d(d) \qquad \textbf{(15)}$$

Fitting **Equation 19** to the TEM particle size data shown in **Figure 73** yields, the medium diameter of particles d_m=2.71±0.04 nm and the standard deviation σ_d= 0.15±0.01 of ln(d/d_m). The particle volume is also lognormally distributed with the median volume $V_m=\pi/6(d_m)^3$ and the standard deviation $\sigma=3\sigma_d$ =0.45 of ln(V/V_m) [92].

4.1.8 Magnetization Study

Above the blocking temperature of superparamagnetic particles, the magnetization M, is free to be aligned the applied field, H [93]. Therefore superparamagnetic particles show no hysteresis in magnetization versus applied field curves. Magnetization, M of superparamagnetic state can be modeled by Langevin function [93,94.,[95]], **Equation 16**.

$$M = M_0\left[\coth\left(\frac{\mu H}{k_B T}\right) - \frac{k_B T}{\mu H}\right] \qquad \textbf{(16)}$$

where M_0 is saturation magnetization of the sample at a given temperature(T), k_B is Boltzmann constant and μ is the effective magnetic moment of particles [93]. The effective magnetic moment of particles is

related to saturation magnetization of bulk phase, M_s [93] and average volume, of particles($\langle V \rangle$) by,

$$\mu = M_s \langle V \rangle \quad \textbf{(17)}$$

Figure **Figure 74** shows the Langevin function (equation 20) fit to the experimental data yield M_0=110 emu/g and μ ≈ 2.76 x 10^{-17} emu . Using saturating magnetization of bulk iron (1700emu/cm^3) the particle sizes was estimated. If particles consist of α-Fe only then estimated size is about 0.1nm. High saturation magnetization value suggest that particles can not contain only α-Fe_2O_3. As discussed above analysis of TEM picture showed that the average circularity of particles in 650^{0}C –PVG samples were 0.976 with standard deviation of 0.0419. The average particle size estimated using TEM analysis is 3.5 nm. These facts imply that these particles consist of α-Fe, and hematite.

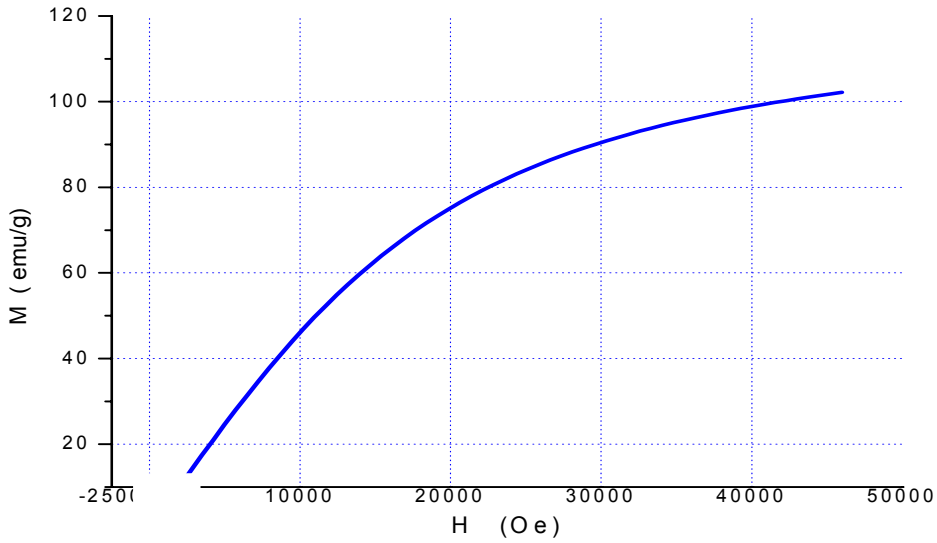

Figure 74. Magnetization curve Fe-PVG

4. 2. Iron Impregnated MCM-41

4.2.1 Low angle XRD

The low angle XRD of the MCM-41 samples showed a hexagonally packed mesostructure. Low angle diffractogram exhibits four Bragg peaks, which can be indexed as (100),(110),(200) and (210) [96]. Inter pore distance 2a can be estimate using distance between (100) planes, d_{100} (**Figure 60**).

$$2a\cos\left(\frac{\Pi}{6}\right) = d_{100}$$

(18)

The diffracted beams from atoms in successive planes cancel unless they are in phase, and the condition for this is given by the BRAGG relationship (**Figure 7a**).

$$2d\sin(\theta) = n\lambda$$

(19)

Where λ is the wavelength of the X-rays, d is the distance between planes and θ is the angle of diffraction. **Equation 23** was applied to low angle XRD to evaluate d_{100} distance. From Equation **22** the distance between pore centers was estimated, $2a = 2d_{100}/\sqrt{3}$, d_{100}= 4.35nm. The low angle XRD confirmed that hexagonal structure preserved after doping (**Figure 61**). But high loading(approximately 8 times higher) distort the 2-D hexagonal structure (**Figure 62**). The high angle XRD shows no crystalline peaks before or after heat treatment. This could be due to ultra fine grain size of iron particles formed in MCM. The superparamagnetic behavior observed in magnetization studies (**Figure 63**)of these particles are also indicative of ultra fine grain size.

The pre edge centroid position of Fe(II) is lower in energy compared to Fe(III). The separation between the average pre-edge centroid positions for

Fe(II) and Fe(III) is in the order of 1.5 eV [97]. The centroid position of absorption pre edge of Fe(II) based minerals are 7112.9 ± 0.5[98] . The centroid of the extracted pre-edges of the Fe doped MCM-41 samples is around 7114.0 eV. The extracted pre-edge contained no peak or partially resolved peak at 7112 eV. The centroid position of pre edge confirms that the charge states of iron in the samples are Fe(III) not Fe(II) (**Figure 46**).

4.2.2 XANES

Pre edge intensities of iron silicates were reported to be higher compared to α-FeO(OH) [99]. This intensity increase was attributed to tetrahedral coordination of iron [99]. The pre edge data of samples show higher intensity compared to *α*-FeO(OH) (**Figure 46**) indicating tetrahedral iron sites and the pre edge intensity increases after heat treatment suggesting more tetrahedral iron sites in heat treated MCM-41 samples. Though tetrahedral iron sites in silica matrices have been reported by number of authors, for example, Rossano, reported iron silicates formed in glasses with mix of 4-and 5-fold coordinated iron [100,101]. Samanta reported ferrisilicate formation in MCM-41, synthesized in the presence of $FeCl_3$ [102]. We found no tetrahedral iron site in PVG matrix even after heat treatment. This is an indication that iron in MCM-41 is different compared to iron in PVG matrix.

4.2.3 EXAFS

EXAFS data were analyzed as described in section **3.1.3e** and **4.1.4** . k^3-weighted EXAFS Fourier transformed spectra are shown in (**Figure 53** and **Figure 54**). The peak near 1.9Å is attributed to Fe-O backscattering in the first coordination shell. The radial distribution function, RDF of samples show some peaks 2-5Å . These may have contributions from Fe-Si, Fe-Fe and Fe-O back scatterings but extremely low concentrations of iron make it hard to distinguish between the backscattering signal and noise in this region. Therefore only first shell fitting of these are used for analysis.

Table 6 : EXAFS Analysis summary of T-01 and T-02 MCM-41 samples

Samples	Shell	Coordination number , N	Distance in Å
α-Fe_2O_3 [104]	Fe-O	3.0	1.95
	Fe-O	3.0	2.10
T-01	Fe-O	4.15	1.88
T-02	Fe-O	4.56	1.95
$FeSiO_4$ [104]	Fe-O	4.0	1.85

XANES pre edge information confirmed the existence of tetrahedrally coordinated iron sites. The Fe-O distances of the first coordination shell are similar to distances observed in the iron oxides such as α-Fe_2O_3-1.99 Å, γ -Fe_2O_3-1.86 Å , α-FeOOH- 1.97 Å, β- FeOOH- 1.89 Å, γ- FeOOH-1.89 Å, and δ- FeOOH-2.00 Å [103, 80] and ferrisilicates Fe-O 1.85A [104].

4.2.4 Mossbauer spectroscopy

Mossbauer data were fit with two set of doublets in order to achieve the best possible fit. These doublets show reasonably small absorption band width [**Figure 58** and **Figure 59**]. The IS<0.3mm/s is an indication of tetrahedrally coordinated Fe(III) and IS>0.3mm/s is generally assigned to octahedrally coordinated Fe(III) [105, 102]. With the increase of temperature the doublet with IS<0.3mm/s, absorption increases (**Figure 58** and **Figure 59**), indicating an increase of tetrahedral iron sites (**Table 7**). The observation is in agreement with the XANES pre edge analysis.

Table 7 . Mossbauer parameters of T-01 and T-02 MCM-41 samples

Sample	Isomer Shift (IS) mm/sec	Quadrupole Splitting (QS) mm/sec
T-01 Prior to heat treatment	0.1364	1.0909
	0.364	0.909
T-02 after to heat treatment	0.0909	1.182
	0.364	0.909

4.2.5 EPR spectroscopy

The EPR data of T-01 and T-02 taken at 77K are presented in **Figure 46**. EPR is considered to be highly sensitive to the local environment of paramagnetic iron [106] but the interpretation of EPR data in zeolites and MCM-41 is still an issue of controversy[107]. The presence of silanol groups and water molecules tends interfere with the EPR signal making it harder to interpret [106]. The better interpretation of the EPR data was achieved by combining results of Mossbauer and XAF data. For iron bearing Zeolites and MCM-41, the signal corresponding to g=4.3 is assigned to Fe^{3+} in strong rhombic distorted tetrahedral coordination [108,102,109]. The weak signal at g=2.18 has been attributed to non frame work iron oxide/oxi-hydroxide nano-particles in silica channels [102]. The strong signal at g=2 in T-01, and T-02 can be assigned to octahedral iron (**Figure 56**). The strong and broader signal around g=2, covers g=2 and g=2.18 suggesting free iron oxide particles in the channels (**Figure 56**). The EPR spectra of T-01 shows a feature at g=4.3 suggesting the presence of tetrahedral iron (**Figure 56**), which is consistent with the XANE pre-edge data. The Mossbauer data confirms the

above assignment of octahedral and tetrahedral iron in T-01. The EXAFS analysis also support the tetrahedral iron in the T-01 sample as first shell fitting shows N=4.25±0.4 (4<N<6). The EPR spectrum of T-02 also shows features at g=4.3 and g=2. The signal at g=2 is strong and broader as in the T-01 sample but some distortion of the signal is observed. It is not possible to explain this as there is not much evidence found in the literature about this kind of distortions. The less distorted EPR spectra at higher (**Figure 56**) temperature indicate that the heating increases the crystallinity of tetrahedral and octahedral iron sites in MCM-41. The pre edge data confirm that heat treatment increase tetrahedrally coordinated iron. Suggesting at high temperature iron in the oxide particles diffuse in to silica network. This is further supported by the Mossbauer data. The observation that doublet with IS< 0.3 mm/s increases (**Figure 56**)with the temperature indicating that iron migrates in to the silica matrix.

4. 3 Iron Impregnated Xerogel

4.3.1 Mossbauer analysis

In our previous studies [110] it was found that the iron impregnated Xerogel (prepared as described in section 2.3) shows only one doublet in the Mossbauer spectrum at room temperature. The quadrupole moment of the doublet is 0.95mm/sec and the isomer shift is 0.4 mm/sec. This suggests that only one specie of iron in the matrix.

4.3.2 XANES

a) Pre-edge and edge energies

The pre edge centroid position can be used to probe oxidation state. As discussed above, the centroid position of Fe(II) minerals is reported to be at 7112.8±0.6 and the pre edge centroid position of Fe(III) bearing minerals are around 7115.0±0.4. The extracted pre edge of xerogel dose not show peak around 7112eV (**Figure 47**). The edge energy of iron impregnated xerogel is also with in the range of Fe(III). This evidence rules out the possibility of Fe(II) in the xerogel.

b) Pre edge intensity

Normalized pre edge intensity of the unheated xerogel samples were comparable with samples of centrosymetric α-Fe_2O_3, thereby ruling out tetrahedral iron sites. Heat treatment (650^0C) marginally increases the pre edge intensity. This suggests that some of the iron migrates into the silica matrix forming tetrahedral sites. However the amount of iron migrates into tetrahedral sites was so small it was not detectable by Mossbauer. The studies done by D.Sunil showed that at 1200^0C amount of tetrahedral iron increases to a detectable level by Mossbauer [111]. These observations suggest that iron migration into tetrahedral sites initiates around 650^0C, but is greatly enhanced at higher temperatures.

4.3.3 EXAFS

The EXAFS data were analyzed as described in section **3.1.3e** and **4.1.4**. Due to the low concentrations of iron, it was hard to distinguish between the backscattering signal and noise. Therefore, only first shell fitting of these are used for analysis. The first Fourier transformed peak intensity was fit with single shell with about 6 oxygen atoms at a distance of 1.92 Å [110]. This is in agreement with Mossbauer data. D. sunil has shown, that in the consolidated gels first shell consist of two N values 5.8 and 3.6 with the Fe-O distance 1.9 Å and 1.7 Å respectively [40]. This provides further evidence that a fraction of the iron is migrates in to tetrahedral sites within the xerogel matrix.

Chapter 5

5. 0. CONCLUSIONS

5.1 Iron impregnated PVG

The study confirms that the image formation of Fe-PVG is due to total iron gradient. The exposed regions contain more iron compared to unexposed regions. Ratio of iron in exposed to unexposed regions may depend on several factors such as incident light intensity, exposure time, initial loading but under the experimental conditions of this study the ratio was found to be around 6:1. As the amount of total iron is proportionate to refractive index, exposed regions have higher refractive index compared to unexposed regions. This refractive index gradient makes the image on the glass.

This study further confirms that high intensity photolysis alters the cross sectional distribution of iron in PVG (**Figure 28**,**Figure 29**). The results show that intense light generates relatively high amount of iron near the surface and relative amount of iron in the PVG decrease exponentially with the depth (**Figure 29**).

Lateral diffusion of iron in the PVG matrix was studied at 650^0C and was found to be insignificant above 10μm. D. Particle growth of iron occurs around 650^0C in the matrix. Therefore sub micron level diffusion may have contributed to particle growth [111].

The present study has shown that when PVG is used as a support matrix, photolized $Fe(CO)_5$ forms an octahedrally coordinated Fe(III). The Fe(III) formed on the surface and the inside of the PVG have a octahedral, crystal field symmetry. The analysis of XANES pre edge showed no peak at < 7112eV. Edge shift analysis along with the above observation rule out the presence of Fe(II) indicating the presence of Fe(0) (section 4.13). The study found no clear evidence of Fe(II) formed in or on the surface before and after

heat treatment. The normalized XANES pre edge showed that there is a secondary source of iron in addition to octahedrally coordinated Fe(III) in the matrix. We assign that secondary source of iron to Fe(0). This is confirmed by the Mossbauer analysis that shows two doublets indicating two forms of iron. And very low isomer shift (0.09 mm/s)of one doublet further justified our assignments. The EXAFS study on the system published elsewhere [73] also confirms Fe-Fe bonds. The Fe(0) formed is not uniformly distributed in the glass matrix. More Fe (0) is found to be in the interior compared to the surface. Mossbauer and magnetic data suggest that Fe(0)formed are not completely oxidized during heat treatment. This may be due to the fact Fe(0) particles formed are covered with Fe_2O_3 protective layer as we proposed in our previous publication [35]. And even after heat treatment, Fe(0) particles appear to be randomly oriented in the matrix where as heat treatment introduced some preferential orientation to Fe(III). This could be due to the fact that they are attached to silica substrate through this oxide envelope.

5.2 Iron impregnated MCM-41

Unlike $Fe(CO)_5$ doped PVG when $Fe(CO)_5$ doped MCM-41 is photolized, that lead to formation of octahedrally and tetrahedrally coordinated iron sites with in the silica matrix. The XANES pre edge shows no peaks around 7112eV region indicating no Fe(II) in the samples. The normalized XANES pre edge intensity increases with the temperature. The EXAFS analysis yields Fe-O bond lengths, 1.88 ± 0.07 Å the values are comparable with iron oxides (such as Fe_2O_3, FeO(OH),..) and ferrisilicares [106]. The EXAFS 1st shell fitting is also in agreement with tetrahedral iron sites. The best fit was achieved by fitting two doublets to the Mossbauer data. This indicates existence of two forms of iron in these samples. The isomer shift values of the two doublets 0.14, 0.36 and 0.09, 0.36 mm/s before and after heat treatment. The two isomer shift values confirm that the samples contain both tetrahedral and octahedral iron. With the increasing temperature the doublet with IS< 0.3mm/s

has shown a significant growth. This indicates an iron migration from octahedral iron, in the oxide particles to tetrahedral iron in silica matrix and this is further supported by the EPR data.

5.3 Iron impregnated Xerogel

The XANES pre edge analysis confirms nonexistence of Fe(II) in the xerogel samples. This observation is common to all the other investigated silica matrices. The EXAFS analysis shows that the Fe-O distances are comparable with iron oxides and ferrisilicares [106]. The EXAFS 1st shell fitting shows no tetrahedral iron sites in unheated samples and samples heated to 650^{0}C. The XANES pre edge intensity marginally increases at 650^{0}C indicating initiation of iron migration into tetrahedral sites. Our previous studies showed that the number of these sites greatly increase at 1200^{0}C [111]. Neither xerogel nor MCM-41 shows any evidence of elemental iron before or after heat treatments. The Fe(0) formation in PVG seems a unique phenomena.

The study shows that when $Fe(CO)_5$ doped xerogel is photolized octahedral coordinated iron and no tetrahedrally coordinated iron is detected at room temperature in xerogel matrix. At higher temperatures tetrahedral iron sites appears in xerogel matrix and these iron sites grow with the temperature. Even though xerogel and MCM-41 are almost pure silica matrices in MCM-41, tetrahedral iron sites appear immediately after photolysis. PVG shows no detectable amount of tetrahedral iron before or after heat treatment.

BIBLIOGRAPHY

1 Elliott, S.R. **Physics of Amorphous Materials,** 2nd Edition (Longmans . London, 1990)

2 Johnson, J. A.; Johnson, C. E. **Moessbauer spectroscopy as a probe of silicate glasses.** Journal of Physics: Condensed Matter (2005), 17(8), R381-R412.

3 A Margaryan and M A Piliavin. **Germanate Glasses: Structure, spectroscopy and properties**. Artech house, Boston. London (1993)

4 Levitz, P.; Ehret, G.; Sinha, S. K.; Drake, J. M. **Porous Vycor glass: the microstructure as probed by electron microscopy, direct energy transfer, small-angle scattering, and molecular adsorption.** Journal of Chemical Physics (1991), 95(8), 6151-61.

5 Kikkinides, E. S.; Kainourgiakis, M. E.; Stefanopoulos, K. L.; Mitropoulos, A. Ch.; Stubos, A. K.; Kanellopoulos, N. K. **Combination of small angle scattering and three-dimensional stochastic reconstruction for the study of adsorption-desorption processes in Vycor porous glass.** Journal of Chemical Physics (2000), 112(22), 9881-9887.

6 Dvoyashkin, Muslim; Valiullin, Rustem; Kaerger, Joerg. **Temperature effects on phase equilibrium and diffusion in mesopores.** Physical Review E: Statistical, Nonlinear, and Soft Matter Physics (2007), 75(4-1), 041202/1-041202/8.

7 Corma, Avelino. **From Microporous to Mesoporous Molecular Sieve Materials and Their Use in Catalysis.** Chemical Reviews (Washington, D. C.) (1997), 97(6), 2373-2419.

8 Vinu, Ajayan; Mori, Toshiyuki; Ariga, Katsuhiko. **New families of mesoporous materials.** Science and Technology of Advanced Materials (2007), Volume Date 2006, 7(8), 753-771.

9 Rouquerol, J.; Avnir, D.; Fairbridge, C. W.; Everett, D. H.; Haynes, J. H.; Pernicone, N.; Ramsay, J. D. F.; Sing, K. S. W.; Unger, K. K. **Recommendations for the characterization of porous solids.** Pure and Applied Chemistry (1994), 66(8), 1739-58.

10 Yanagisawa, Tsuneo; Shimizu, Toshio; Kuroda, Kazuyuki; Kato, Chuzo. **The preparation of alkyltrimethylammonium-kanemite complexes and their conversion to microporous materials.** Bulletin of the Chemical Society of Japan (1990), 63(4), 988-92.

11 Inagaki, S.; Fukushima, Y.; Kuroda, K. **Synthesis of highly ordered mesoporous materials from a layered polysilicate.** Journal of the Chemical Society, Chemical Communications (1993), (8), 680-2.

12 Anandan, Sambandam; Okazaki, Masaharu. **Dynamics, flow motion and nanopore effect of molecules present in the MCM-41 nanopores-An overview.** Microporous and Mesoporous Materials (2005), 87(2), 77-92.

13 Costa, Andreia A.; Ghesti, Grace F.; de Macedo, Julio L.; Braga, Valdeilson S.; Santos, Marcello M.; Dias, Jose A.; Dias, Silvia C. L. **Immobilization of Fe, Mn and Co tetraphenylporphyrin complexes in MCM-41 and their catalytic activity in cyclohexene oxidation reaction by hydrogen peroxide.** Journal of Molecular Catalysis A: Chemical (2008), 282(1-2), 149-157.

14 Zeng, Wei; Qian, Xue-Feng; Zhang, Yan-Bo; Yin, Jie; Zhu, Zi-Kang. **Organic modified mesoporous MCM-41 through solvothermal process as drug delivery system.** Materials Research Bulletin (2005), 40(5), 766-772.

15 Vallet-Regi, M.; Ramila, A.; del Real, R. P.; Perez-Pariente, J. **A New Property of MCM-41: Drug Delivery System.** Chemistry of Materials (2001), 13(2), 308-311.

16 Diaz, J. Felipe; Balkus, Kenneth J., Jr. **Enzyme immobilization in MCM-41 molecular sieve.** Journal of Molecular Catalysis B: Enzymatic (1996), 2(2-3), 115-126.

17 Rani, V. Radha; Kishan, M. Radha; Kulkarni, S. J.; Raghavan, K. V. **Immobilization of metalloporphyrin complexes in molecular sieves and their catalytic activity.** Catalysis Communications (2005), 6(8), 531-538.

18 Tsoncheva, Tanya; Areva, Sami; Dimitrov, Momtchil; Paneva, Daniela; Mitov, Ivan; Linden, Mika; Minchev, Christo. **MCM-41 silica modified with copper and iron oxides as catalysts for methanol decomposition.** Journal of Molecular Catalysis A: Chemical (2006), 246(1-2), 118-127.

19 Corma, Avelino. **From Microporous to Mesoporous Molecular Sieve Materials and Their Use in Catalysis.** Chemical Reviews (Washington, D. C.) (1997), 97(6), 2373-2419.

20 U.Schwertmann, R.M. Cornell, **Iron oxides in the laboratory** VCH New York (1996).

21 Kohn, Ralf; Paneva, Daniela; Dimitrov, Momtchil; Tsoncheva, Tanya; Mitov, Ivan; Minchev, Christo; Froba, Michael. **Studies on the state of iron oxide nanoparticles in MCM-41 and MCM-48 silica materials.** Microporous and Mesoporous Materials (2003), 63(1-3), 125-137.

22 Bomati-Miguel, Oscar; Tartaj, Pedro; Morales, Maria P.; Bonville, Pierre; Golla-Schindler, Ute; Zhao, Xinqing Q.; Veintemillas-Verdaguer, Sabino. **Core-shell iron-iron oxide nanoparticles synthesized by laser-induced pyrolysis.** Small (2006), 2(12), 1476-1483.

23 Cherepy, Nerine J.; Liston, Dorion B.; Lovejoy, Jennifer A.; Deng, Hongmei; Zhang, Jin Z. **Ultrafast Studies of Photoexcited Electron Dynamics in □ - and □ -Fe2O3 Semiconductor Nanoparticles.** Journal of Physical Chemistry B (1998), 102(5), 770-776.

24 Cornell,R,M: Schwertmann,U.The Iron Oxides; VCH: New York, 1996.

25 J.W. Bulte and D.L. Kraitchman, *Curr. Pharm.* **Monitoring cell therapy using iron oxide MR contrast agents.** *Biotechnol.* **5** (2004), p. 567.

26 E.J. Delikatny and H. Poptani, **MR techniques for in vivo molecular and cellular imaging.** *Radiol. Clin. North Am.* **43** (2005), p. 205.

27 G.M. Lanza, P.M. Winter, S.D. Caruthers, A.M. Morawski, A.H. Schmieder and K.C. Crowder, **Magnetic resonance molecular imaging with nanoparticles.** *J. Nucl. Cardiol.* **11** (2004), p. 733.

28 J. Vymazal, J.W. Bulte, J.A. Frank, G. Di Chiro and R.A. Brooks**, Frequency dependence of MR relaxation times. I. Paramagnetic ions**. *J. Magn. Reson. Imaging* **3** (1993), p. 637.

29 V.G. Roullin, J.R. Deverre, L. Lemarie, F. Hindré, M.C.V. Julienne, R. Vienet and J.P. Benoit, **Anti-cancer drug diffusion within living rat brain tissue: An experimental study using [^{3}H](6)-5-fluorouracil-loaded PLGA microspheres.** *Eur. J. Pharm. Biopharm.* **53** (2002), p. 293.

30 Koksharov, Yu. A.; Pankratov, D. A.; Gubin, S. P.; Kosobudsky, I. D.; Beltran, M.; Khodorkovsky, Y.; Tishin, A. M. **Electron paramagnetic resonance of ferrite nanoparticles.** Journal of Applied Physics (2001), 89(4), 2293-2298.

31 Suber, Lorenza; Santiago, Antoni Garcia; Fiorani, Dino; Imperatori, Patrizia; Testa, Alberto Maria; Angiolini, Massimo; Montone, Amelia; Dormann, Jean L. **Structural and magnetic properties of -Fe2O3 nanoparticles.** Applied Organometallic Chemistry (1998), 12(5), 347-351.

32 Turcu, R.; Peter, I.; Pana, O.; Giurgiu, L.; Aldea, N.; Barz, B.; Grecu, M. N.; Coldea, A. **Structural and magnetic properties of polypyrrole nanocomposites.** Molecular Crystals and Liquid Crystals (2004), 417 235-243.

33 E.A Mendoza; H.D. Gafney. **Photolithographic processing of integrated optic devices in PVG.** Conference on optoelectronic Materials, Harvard University, Cambridge, MA, 1987.

34 Paras N. Prasad **Nanophotonics** pg 280-281

35 Sunil, Dehipawalage; Devi, P. Sujatha; Dong, Jinquan; McQuade, Arthur W.; Mendoza, Edgar A.; Gafney, Harry D.. **Integrated optics: a new focus for inorganic chemistry.** Comments on Inorganic Chemistry (2003), 24(3-4), 69-136.

36 Gafney, Harry D. **A photochemical approach to integrated optics.** Journal of Macromolecular Science, Chemistry (1990), A27(9-11), 1187-202.

37 Luong, John C.; Borrelli, Nicholas F. **Fabrication of III-V semiconductor quantum dots in porous glass.** Materials Research Society Symposium Proceedings (1989), 144(Adv. Mater., Process. Devices III-V Compd. Semicond.), 695-700.

38 Dong, Jinquan; Gafney, Harry D.. **Fabrication and patterning surface conductive porous glass.** Journal of Non-Crystalline Solids (1996), 203(Optical and Electrical Properites of Glasses), 329-333.

39 Farges, Francois; Lefrere, Yannick; Rossano, Stephanie; Berthereau, Anne; Calas, Georges; Brown, Gordon E. **The effect of redox state on the local structural environment of iron in silicate glasses: a combined XAFS spectroscopy, molecular dynamics, and bond valence study.** J. Non-Cryst. Solids (2004), 344(3), 176-188.

40 Mendoza, Edgar A.; Wolkow, Eugene; Sunil, D.; Wong, Peter; Sokolov, Jonathon; Rafailovich, Miriam H.; Den Boer, Marten; Gafney, Harry D.. **A comparison of iron oxides photodeposited in porous Vycor glass and tetramethoxysilane/methanol/water xerogels.** Langmuir (1991), 7(12), 3046-51.

41 Sunil, D.; McQuade, Arthur W.; Ye, Gouzhang; Gafney, Harry D.. **Photodeposition of diffraction gratings in glass: a comparison of lithographic, laser writing and holographic deposition.** Applied Spectroscopy (2000), 54(6), 869-877

42 Rossetti, R.; Hull, R.; Gibson, J. M.; Brus, L. E. **Hybrid electronic properties between the molecular and solid state limits: lead sulfide and silver halide crystallites.** Journal of Chemical Physics (1985), 83(3), 1406-10.

43 Ekimov, A. I.; Efros, Al. L.; Onushchenko, A. A. **Quantum size effect in semiconductor microcrystals.** Solid State Communications (1985), 56(11), 921-4.

44 Dapurkar, S. E.; Badamali, S. K.; Selvam, P. **Nanosized metal oxides in the mesopores of MCM-41 and MCM-48 silicates.** Catalysis Today (2001), 68(1-3), 63-68.

45 Kresge, C. T.; Leonowicz, M. E.; Roth, W. J.; Vartuli, J. C.; Beck, J. S. **Ordered mesoporous molecular sieves synthesized by a liquid-crystal template mechanism.** Nature (London, United Kingdom) (1992), 359(6397), 710-12.

46 Zeng, Wei; Qian, Xue-Feng; Zhang, Yan-Bo; Yin, Jie; Zhu, Zi-Kang. **Organic modified mesoporous MCM-41 through solvothermal process as drug delivery system.** Materials Research Bulletin (2005), 40(5), 766-772.

47 Suvanto, S.; Hukkamaeki, J.; Pakkanen, T. T.; Pakkanen, T. A. **High-Cobalt-Loaded MCM - 41 via the Gas-Phase Method.** Langmuir (2000), 16(9), 4109-4115.

48 Corma, Avelino. **From Microporous to Mesoporous Molecular Sieve Materials and Their Use in Catalysis.** Chemical Reviews (Washington, D. C.) (1997), 97(6), 2373-2419.

49 G. Centi, B. Wichterlova, A.T Bell , **Catalysis by Uniqie Metal Ion Structures in Solid Matrices, in**: NATO Science Series, Kluwer Acadamic, Dordrecht, 2001.

50 Zhang, Xiaoming; Guo, Haiquan; Chi, Ning; Wang, Shunchin C.; Yang, Nan-Loh; Akins, Daniel L. **Self-aligned magnetic dipole moments of Fe2O3 formed within sol-gel matrix.** Materials Chemistry and Physics (2006), 98(2-3), 207-211.

51 Rochelle M. Cornell and Udo Schwertmann . **The Iron Oxides: Structure, Properties, Reactions, Occurrences and Uses**. Wiley-VCH; 2 edition (October 17, 2003).

52 Kawabata, Tomonori; Ohishi, Yoshihiko; Itsuki, Satoko; Fujisaki, Naoko; Shishido, Tetsuya; Takaki, Ken; Zhang, Qinghong; Wang, Ye; Takehira, Katsuomi. **Iron-containing MCM-41 catalysts for Baeyer-Villiger oxidation of ketones using molecular oxygen and benzaldehyde.** Journal of Molecular Catalysis A: Chemical (2005), 236(1-2), 99-106.

53 Trost, Barry M. **The atom economy: a search for synthetic efficiency.** Science (Washington, DC, United States) (1991), 254(5037), 1471-7.

54 P.T. Anastas, J.C. Warner, **Green Chemistry: Theory and Practice**, Oxford University Press, 1998

55 N.I. Sax, **Dangerous Properties of Industrial Materials**, 6th ed, Van Nostrand reinhold Company Inc., New York, 1984.

56 Amama, Placidus B.; Lim, Sangyun; Ciuparu, Dragos; Yang, Yanhui; Pfefferle, Lisa; Haller, Gary L. **Synthesis, Characterization, and Stability of Fe-MCM-41 for Production of Carbon Nanotubes by Acetylene Pyrolysis.** Journal of Physical Chemistry B (2005), 109(7), 2645-2656.

57 John D. Wright and Nico A.J.M. Sommerdijk **Sol-Gel Material Chemistry and Applications** ,Gordon and Breach Science Publishers

58 Ice, G. E.; Hubbard, C. R.; Larson, B. C.; Pang, J. W. L.; Budai, J. D.; Spooner, S.; Vogel, S. C.; Rogge, R. B.; Fox, J. H.; Donaberger, R. L. **High - performance Kirkpatrick - Baez supermirrors for neutron milli- and micro-beams.** Materials Science & Engineering, A: Structural Materials: Properties, Microstructure and Processing (2006).

59 S. Bajt, R. Sutton, S. Delaney. **Microanalysis of iron oxidation states in erath and planetary materials.** Physica B 208 & 209 (1995) 243-244.

60 Piamonteze, Cinthia; Tolentino, Helio C. N.; Ramos, Aline Y. **The phase-derivative method in EXAFS applied to the study of rare earth nickel perovskites.** Nuclear Instruments & Methods in Physics Research, Section B: Beam Interactions with Materials and Atoms (2006), 246(1), 151-157.

61 Wolska, A.; Lawniczak-Jablonska, K.; Klepka, M.; Walczak, M. S.; Misiuk, A. **Local structure around Mn atoms in Si crystals implanted with Mn+ studied using x-ray absorption spectroscopy techniques.** Physical Review B: Condensed Matter and Materials Physics (2007), 75(11), 113201/1-113201/4.

62 Miyoshi, Hirokazu; Yoneyama, Hiroshi. **Photochemical properties of iron oxide incorporated in clay interlayers.** Journal of the Chemical Society, Faraday Transactions 1: Physical Chemistry in Condensed Phases (1989), 85(7), 1873-80.

63 Sohn, B. H.; Cohen, R. E. **Processible Optically Transparent Block Copolymer Films Containing Superparamagnetic Iron Oxide Nanoclusters.** Chemistry of Materials (1997), 9(1), 264-269.

64 Dodd, Charles G.; Glen, Gerald L.. **Chemical bonding studies of silicates and oxide by x-ray K-emissionspectroscopy.** Journal of Applied Physics (1968), 39(12), 5377-84.

65 Downes, H.; Reichow, M. K.; Mason, P. R. D.; Beard, A. D.; Thirlwall, M. F. **Mantle domains in the lithosphere beneath the French Massif Central: trace element and isotopic evidence from mantle clinopyroxenes.** Chemical Geology (2003), 200(1-2), 71-87.

66 Yasuhiro Iwasawa, **X-Ray Absorption Fine Structure.** World Scientific Publishing Company (August 1996).

67 Leri, Alessandra C.; Hay, Michael B.; Lanzirotti, Antonio; Rao, William; Myneni, Satish C. B. **Quantitative Determination of Absolute Organohalogen Concentrations in Environmental Samples by X-ray Absorption Spectroscopy.** Analytical Chemistry (2006), 78(16), 5711-5718.

68 Galoisy, L.; Calas, G.; Arrio, M. A. **High-resolution XANES spectra of iron in minerals and glasses: structural information from the pre-edge region.** Chemical Geology (2001), 174(1-3), 307-319.

69 Berry, Andrew J.; O'Neill, Hugh St. C.; Jayasuriya, Kasthuri D.; Campbell, Stewart J.; Foran, Garry J. **XANES calibrations for the oxidation state of iron in a silicate glass.** American Mineralogist (2003), 88(7), 967-977.

70 Gabriele Giuli, G, Pratesi; C, Cipriani and E, Paris. **Iron local structure in tektites and impact glasses by extended X-ray absorption fine structure and high-resolution X-ray absorption near-edge structure spectroscopy.** Geochimica et Cosmochimica Acta, Vol 66, No. 24, pp 4347-4353. (2002).

71 Prietzel, J.; Thieme, J.; Eusterhues, K.; Eichert, D. **Iron speciation in soils and soil aggregates by synchrotron-based X-ray microspectroscopy (XANES, -XANES).** European Journal of Soil Science (2007), 58(5), 1027-1041.

72 Wilke, Max; Farges, Francois; Petit, Pierre-Emmanuel; Brown, Gordon E., Jr.; Martin, Francois. **Oxidation state and coordination of Fe in minerals: An Fe K-XANES spectroscopic study.** American Mineralogist (2001), 86(5-6), 714-730.

73 Sunil, D.; Sokolov, J.; Rafailovich, M. H.; Kotyuzhanskii, B.; Gafney, H. D.; Wilkens, B. J.; Hanson, A. L. **Microstructure of photodeposited iron in porous Vycor glass.** Journal of Applied Physics (1993), 74(6), 3768-77.

74 Darsillo, Michael S.; Gafney, Harry D.; Paquette, Michael S. **Photochemistry of Fe(CO)5 adsorbed onto porous Vycor glass.** Journal of the American Chemical Society (1987), 109(11), 3275-86.

75 Wilke, Max; Farges, Francois; Partzsch, Georg M.; Schmidt, Christian; Behrens, Harald. **Speciation of Fe in silicate glasses and melts by in-situ XANES spectroscopy.** American Mineralogist (2007), 92(1), 44-56.

76 Cai, Qiang; Luo, Zhong-Sheng; Pang, Wen-Qin; Fan, Yu-Wei; Chen, Xi-Hua; Cui, Fu-Zhai. **Dilute Solution Routes to Various Controllable Morphologies of MCM-41 Silica with a Basic Medium.** Chemistry of Materials (2001), 13(2), 258-263.

77 Stohr, J.; Sette, F.; Johnson, Allen L. **Near-edge x-ray-absorption fine-structure studies of chemisorbed hydrocarbons: bond lengths with a ruler.** Physical Review Letters (1984), 53(17), 1684-7.

78 B. K. Agarwal . **X-Ray Spectroscopy: An Introduction (Springer Series in Optical Sciences)** (Jun 1991).

79 Engemann, C.; Hormes, J.; Longen, A.; Dotz, K. H. **An x-ray absorption near edge spectroscopy (XANES) study on organochromium complexes at the Cr K-edge.** Chemical Physics (1998), 237(3), 471-481.

80 Schneider, Jorg J.; Czap, Norbert; Hagen, Jorg; Engstler, Jorg; Ensling, Jurgen; Gutlich, Philipp; Reinoehl, Uwe; Bertagnolli, Helmut; Luis, Fernando; De Jongh, L. Jos; Wark, Michael; Grubert, Gerd; Hornyak, Gabor L.; Zanoni, Roberto. **Metallorganic routes to nanoscale iron and titanium oxide particles encapsulated in mesoporous alumina: formation, physical properties, and chemical reactivity.** Chemistry--A European Journal (2000), 6(23), 4305-4321.

81 Goldfarb, D.; Bernardo, M.; Strohmaier, K. G.; Vaughan, D. E. W.; Thomann, H. **Characterization of Iron in Zeolites by X-band and Q-Band ESR, Pulsed ESR, and UV-Visible Spectroscopies.** Journal of the American Chemical Society (1994), 116(14), 6344-53.

82 Antoni, Emilie; Montagne, Lionel; Daviero, Sylvie; Palavit, Gerard; Bernard, Jean-Luc; Wattiaux, Alain; Vezin, Herve. **Structural characterization of iron-alumino-silicate glasses.** Journal of Non-Crystalline Solids (2004), 345 & 346 66-69.

83 Dominic P. E. Dickson and Frank J. Berry, **Mossbauer spectroscopy** . Camberidge University Press.

84 J. Danon , **Application of the Mossbauer Effect in Chemistry and Solid-State Physics,** Technical Report series No 50, International atomic Energy agency, Vienna, 1966, Pg 32.

85 Thakur, M.; De, K.; Giri, S.; Si, S.; Kotal, A.; Mandal, T. K. **Interparticle interaction and size effect in polymer coated magnetite nanoparticles.** Journal of Physics: Condensed Matter (2006), 18(39), 9093-9104.

86 L.Neel, Ann. **An interpretation of the magnetic properties of some iron oxide powders.** Geophys. 5,99 (1949).

87 W.F. Brown, Jr.,**Thermal Fluctuations of a Single-Domain Particle** Phys.Rev. 130,1677 (1963).

88 Liou, S. H.; Chien, C. L. **Particle size dependence of the magnetic properties of ultrafine granular films.** Journal of Applied Physics (1988), 63(8, Pt. 2B), 4240-2.

89 Brown, Wilbur K.; Wohletz, Kenneth H. **Derivation of the Weibull distribution based on physical principles and its connection to the Rosin-Rammler and lognormal distributions.** Journal of Applied Physics (1995), 78(4), 2758-63.

90 Roy, S.; Roy, B.; Chakravorty, D. **Magnetic properties of iron nanoparticles grown in a glass matrix.** Journal of Applied Physics (1996), 79(3), 1642-5.

91 Popplewell, J.; Sakhnini, L. **The dependence of the physical and magnetic properties of magnetic fluids on particle size.** Journal of Magnetism and Magnetic Materials (1995), 149(1-2), 72-8.

92 O'Grady, K.; Bradbury, A. **Particle size analysis in ferrofluids.** Journal of Magnetism and Magnetic Materials (1983), 39(1-2), 91-4.

93 Yoon, M.; Kim, Y. M.; Kim, Y.; Volkov, V.; Song, H. J.; Park, Y. J.; Vasilyak, S. L.; Park, I.-W. **Magnetic properties of iron nanoparticles in a polymer film.** Journal of Magnetism and Magnetic Materials (2003), 265(3), 357-362.

94 Klokkenburg, M.; Erne, B. H.; Mendelev, V.; Ivanov, A. O. **Magnetization behavior of ferrofluids with cryogenically imaged dipolar chains.** Journal of Physics: Condensed Matter (2008), 20(20), 204113/1-204113/5.

95 Chakraverty, S.; Bandyopadhyay, M.; Chatterjee, S.; Dattagupta, S.; Frydman, A.; Sengupta, S.; Sreeram, P. A. **Memory in a magnetic nanoparticle system: Polydispersity and interaction effects.** Physical Review B: Condensed Matter and Materials Physics (2005), 71(5), 054401/1-054401/8.

96 Cai, Qiang; Luo, Zhong-Sheng; Pang, Wen-Qin; Fan, Yu-Wei; Chen, Xi-Hua; Cui, Fu-Zhai. **Dilute Solution Routes to Various Controllable Morphologies of MCM-41 Silica with a Basic Medium.** Chemistry of Materials (2001), 13(2), 258-263.

97 Hensen, Emiel; Zhu, Qingjun; Liu, Pang-Hung; Chao, Kuei-Jung; Van Santen, Rutger. **On the role of aluminum in the selective oxidation of benzene to phenol by nitrous oxide over iron-containing MFI zeolites: an in situ Fe XANES study.** Journal of Catalysis (2004), 226(2), 466-470.

98 Prietzel, J.; Thieme, J.; Eusterhues, K.; Eichert, D. **Iron speciation in soils and soil aggregates by synchrotron-based X-ray microspectroscopy (XANES, μ -XANES).** European Journal of Soil Science (2007), 58(5), 1027-1041.

99 Matsubayashi, N.; Shimada, H.; Imamura, M.; Sato, T.; Okabe, K.; Yoshimura, Y.; Nishijima, A. **Determination of Fe-substituted sites in the MFI structure by Fe K-edge EXAFS.** Catalysis Today (1996), 29(1-4), 273-277.

100 Rossano, S.; Ramos, A.; Delaye, J.-M.; Filipponi, A.; Creux, S.; Brouder, Ch.; Calas, G. **Iron surrounding in CaO-FeO-2SiO2 glass: EXAFS and molecular dynamics simulation.** Journal of Synchrotron Radiation (1999), 6(3), 247-248.

101 Rossano, S.; Ramos, A.; Delaye, J.-M.; Creux, S.; Filipponi, A.; Brouder, Ch.; Calas, G. **EXAFS and molecular dynamics combined study of CaO-FeO-2SiO2 glass. New insight into site significance in silicate glasses.** Europhysics Letters (2000), 49(5), 597-602.

102 Samanta, S.; Giri, S.; Sastry, P. U.; Mal, N. K.; Manna, A.; Bhaumik, A. **Synthesis and Characterization of Iron-Rich Highly Ordered Mesoporous Fe-MCM-41.** Industrial & Engineering Chemistry Research (2003), 42(13), 3012-3018.

103 Schneider, Jorg J.; Czap, Norbert; Hagen, Jorg; Engstler, Jorg; Ensling, Jurgen; Gutlich, Philipp; Reinoehl, Uwe; Bertagnolli, Helmut; Luis, Fernando; De Jongh, L. Jos; Wark, Michael; Grubert, Gerd; Hornyak, Gabor L.; Zanoni, Roberto. **Metallorganic routes to nanoscale iron and titanium oxide particles encapsulated in mesoporous alumina: formation, physical properties, and chemical reactivity.** Chemistry--A European Journal (2000), 6(23), 4305-4321.

104 Yan, Guiyang; Long, Jinlin; Wang, Xuxu; Li, Zhaohui; Wang, Xinchen; Xu, Yiming; Fu, Xianzhi. **Insight into Photoactive Sites for the Ethylene Oxidation on Commercial HZSM-5 Zeolites with Iron Impurities by UV**

Raman, X-ray Absorption Fine Structure, and Electron Paramagnetic Resonance Spectroscopies. Journal of Physical Chemistry C (2007), 111(13), 5195-5202.

105 Lazar, K.; Borbely, G.; Beyer, H. **In situ Moessbauer study of framework-substituted (Fe)ZSM 5 zeolites.** Zeolites (1991), 11(3), 214-22.

106 Goldfarb, D.; Bernardo, M.; Strohmaier, K. G.; Vaughan, D. E. W.; Thomann, H. **Characterization of Iron in Zeolites by X-band and Q-Band ESR, Pulsed ESR, and UV-Visible Spectroscopies.** Journal of the American Chemical Society (1994), 116(14), 6344-53.

107 Amama, Placidus B.; Lim, Sangyun; Ciuparu, Dragos; Yang, Yanhui; Pfefferle, Lisa; Haller, Gary L. **Synthesis, Characterization, and Stability of Fe-MCM-41 for Production of Carbon Nanotubes by Acetylene Pyrolysis.** Journal of Physical Chemistry B (2005), 109(7), 2645-2656.

108 Wang, Ye; Zhang, Qinghong; Shishido, Tetsuya; Takehira, Katsuomi. **Characterizations of Iron-Containing MCM-41 and Its Catalytic Properties in Epoxidation of Styrene with Hydrogen Peroxide.** Journal of Catalysis (2002), 209(1), 186-196.

109 Stockenhuber, Michael; Hudson, Michael J.; Joyner, Richard W. **Preparation, Characterization, and Unusual Reactivity of Fe-MCM-41.** Journal of Physical Chemistry B (2000), 104(14), 3370-3374.

110 Mendoza, Edgar A.; Wolkow, Eugene; Sunil, D.; Wong, Peter; Sokolov, Jonathon; Rafailovich, Miriam H.; Den Boer, Marten; Gafney, Harry D. **A comparison of iron oxides photodeposited in porous Vycor glass and**

tetramethoxysilane/methanol/water xerogels. Langmuir (1991), 7(12), 3046-51.

111 D.Sunil ,**Spectroscopic studies the of microstructure of metal oxides in Vycor glass**, PhD thesis submitted to Department of Physics CUNY graduate Center 1993.